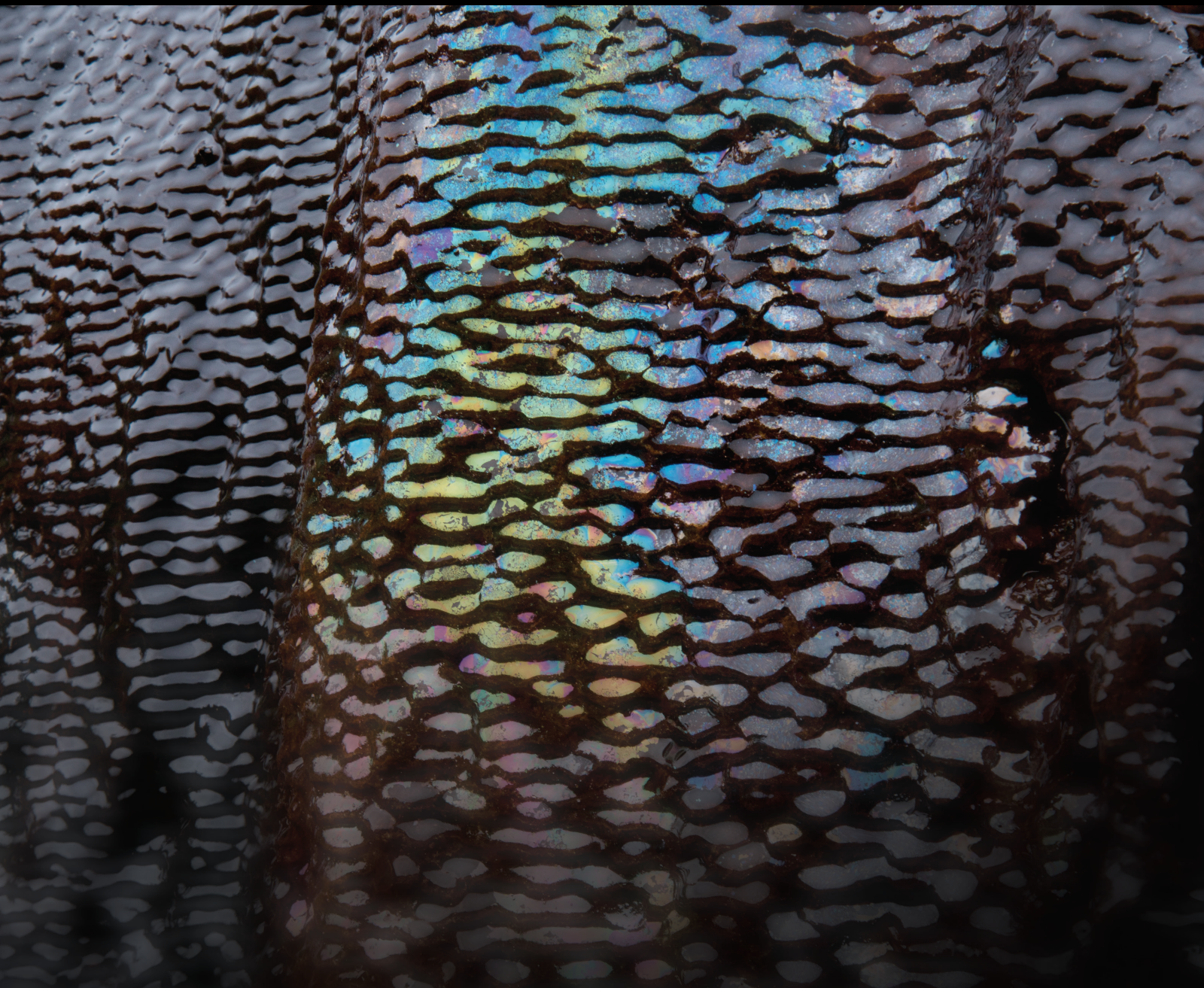# The Role and Impact of Geofluids in Geohazards 2020

Lead Guest Editor: Ching Hung
Guest Editors: Xueyu Pang, Guan-Wei Lin, Kuo-Hsin Yang, and Ryosuke Uzuoka

The Role and Impact of Geofluids in Geohazards 2020

The Role and Impact of Geofluids in Geohazards 2020

Lead Guest Editor: Ching Hung
Guest Editors: Xueyu Pang, Guan-Wei Lin, Kuo-Hsin Yang, and Ryosuke Uzuoka

Bisheng Wu iD, China
Da-yang Xuan iD, China
Yi Xue iD, China
HE YONGLIANG, China
Fan Yang iD, China
Zhenyuan Yin iD, China
Sohrab Zendehboudi, Canada
Zhixiong Zeng iD, Hong Kong
Yuanyuan Zha iD, China
Keni Zhang, China
Mingjie Zhang iD, China
Rongqing Zhang, China
Xianwei Zhang iD, China
Ye Zhang iD, USA
Zetian Zhang iD, China
Ling-Li Zhou iD, Ireland
Yingfang Zhou iD, United Kingdom
Daoyi Zhu iD, China
Quanle Zou, China
Martina Zucchi, Italy

Contents

WILEY | Hindawi

Research Article

Postfailure Characterization of Shallow Landslides Using the Material Point Method

Thanh Son Nguyen (ID),[1] **Kuo-Hsin Yang** (ID),[2] **Chia-Chun Ho**,[3] and **Feng-Chi Huang**[4]

[1]*Faculty of Bridges and Roads, National University of Civil Engineering (NUCE), 55 Giai Phong Rd., Hai Ba Trung Dist., Hanoi 11616, Vietnam*
[2]*Department of Civil Engineering, National Taiwan University (NTU), 1 Sec. 4, Roosevelt Rd., Taipei 106, Taiwan*
[3]*Department of Civil and Construction Engineering, National Taiwan University of Science and Technology (Taiwan Tech), 43 Sec. 4, Keelung Rd., Taipei 106, Taiwan*
[4]*Taiwan Construction Research Institute, 11F 190 Sec. 2, Chunghsin Rd., New Taipei City 231, Taiwan*

Correspondence should be addressed to Kuo-Hsin Yang; khyang@ntu.edu.tw

Although the mechanisms of slope failure caused by rising groundwater have been widely investigated, the kinematic behavior of landslides in the postfailure stage, which contains essential information for hazard mitigation and risk assessment, has not yet been fully studied. Thus, in this study, a series of numerical simulations using the material point method (MPM) were conducted to analyze the kinematic behavior and soil movement of shallow landslides (infinite slope problems). First, the proposed MPM formulation was validated in a full-scale landslide flume test. The simulated results of final slope profile, runout distance, deposit height, shear band development, slope displacement, and velocity accorded with the experimental results, suggesting that the MPM can quantitatively simulate large deformations. A parametric study of shallow slopes with various hydrological conditions and soil hydraulic and soil mechanical parameters was then performed to assess the influence of the aforementioned factors on landslide kinematics. The simulation results indicated that mechanical behavior at the slope toe is complex; the multiple plastic shear bands generated at the slope toe were due to a combination of shearing and compression. The deposition profile of the slopes was significantly influenced by all input parameters. Among the aforementioned parameters, soil cohesion, location of the groundwater table, and saturated soil permeability most greatly affected runout distance in the sensitivity assessment. Soil friction angle had a minor influence on the kinematic behavior of the slope.

1. Introduction

Landslides are major geotechnical disasters that occur worldwide. Forecasting landslide kinematics, such as the deposition profile, travel distance, and velocity of the unstable mass, is key in preventing and controlling the risks that landslides pose to infrastructure and human lives [1]. Many researchers have developed both physical and numerical models as well as conducted field observations to understand the kinematic characteristics of landslides [2]. However, most studies have focused on evaluating the failure mechanism of slopes rather than the postfailure behaviors of landslides [3]. Understanding the kinematic behavior of landslides remains a challenge that has yet to be completely surmounted.

Numerous experiments using small-scale [4–8] and large-scale [9] landslide experiments have been conducted to investigate debris flows behavior. Although existing methods for identifying the failure mechanisms of slopes yield undeniable advantages, most of these methods have mainly focused on the behavior of noncohesive soil [10]. Moreover, experimental approaches are time-intensive, and a scale model, unlike a field observation, cannot capture the same initial conditions.

With the development of increasingly powerful computers, numerical simulations have been increasingly used as powerful tools for slope stability analysis [11]. However, the numerical modeling of landslide kinematics (particularly deformation and runout) remains challenging for most

(a) MPs→nodes   (b) Solution on nodes

(d) Reset mesh   (c) Nodes→MPs

● ○ Material point   ↗ Displacement vector

⊞ Node and mesh   ↗ Reset mesh

↗ Update information
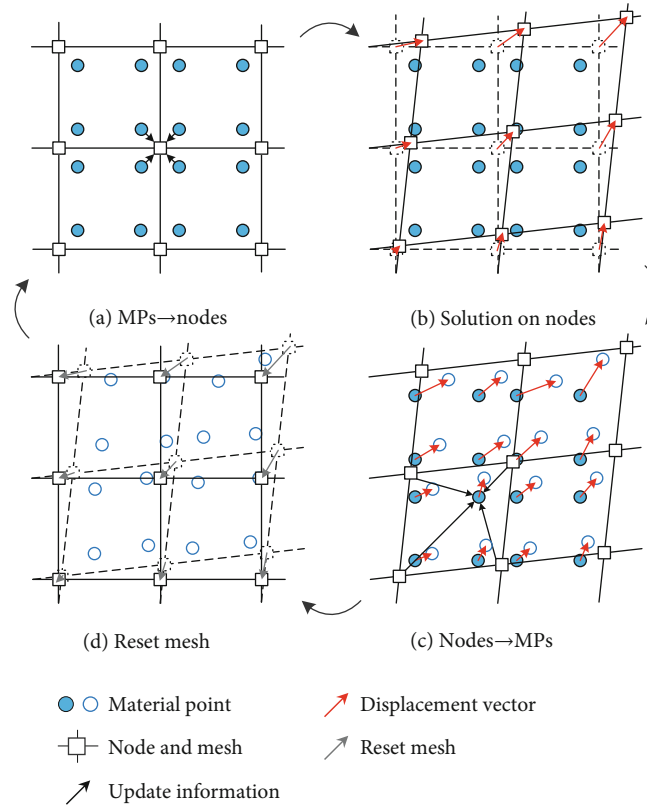
FIGURE 1: Computational cycles of MPM: (a) map MP info to nodes, (b) solve equilibrium equations on nodes and update nodes' info and positions, (c) map node info to MPs and update MPs' info and positions, and (d) reset mesh.

geotechnical engineers [12]. Traditional numerical methods in stability analysis, such as the limit equilibrium method (LEM) [13] and finite element method (FEM) using the standard Lagrangian approach [14], remain useful only for analyzing slope response in the early stages of failure (i.e., the prefailure and failure stages), especially for identifying the location of failure surfaces and obtaining accurate safety factors, when the small strain assumption is considered reasonable [15]. These methods generally have limitations in problems associated with the development of large deformations after failure (i.e., the postfailure stage) because of excessive mesh distortions in the shear zone that lead to either inaccurate results or a calculation failure from a failure to converge [16]. In addition, advanced techniques that use the updated Lagrangian FEM formulation—in which first, the computational mesh is assumed to deform with the considered body and second, all static and kinematic variables that refer to the last calculated configuration in the solution require continual remeshing—lead to unstable and inaccurate results for large strain problems [17]. Troncone [18] simulated the failure mechanism of the Senise landslide at Southern Italy, and their simulated location of the failure surface, as identified in their finite element (FE) result, was consistent with the observed location; however, the predicted crest deformation was limited to a maximum of 0.53 m at failure onset. This predicted crest deformation was smaller than that in field observations. This small crest deformation was obtained even when a Lagrangian finite

element formulation, updated for a large deformation, was used by Mohammadi and Taiebat [3] in a later study.

To overcome the drawbacks of mesh-based methods, a robust method for addressing large-deformation problems is warranted. Particle-based methods (i.e., meshless or mesh-free methods)—which include smoothed particle hydrodynamics (SPH) [19], the discrete element method [20] proposed by Cundall and Strack [21], and discontinuous deformation analysis—are robust approaches to solving large-deformation problems and to describing the postfailure mechanisms of landslides. These methods do not require data to be stored or the definition of a mesh to feature the connection of points. However, these methods incur a relatively high computational cost because neighboring particles must be intensively searched after each time step. This results in consistency loss [22]. In addition, SPH is limited by its inability to simulate multiphase interactions that involve failure evolution. Soga et al. [23] summarized the advantages and disadvantages of numerical methods for simulating landslide problems. By using both Eulerian (i.e., a fixed finite element grid) and Lagrangian (i.e., moving material points) formulations, Sulsky et al. [24] developed the material point method (MPM) to simulate the dynamic deformation of solid bodies. MPM has been successfully used to simulate geotechnical problems related to the large deformation of slopes and dams [1, 23, 25–31]. Although the MPM effectively models slope failure, few comprehensive overviews have been conducted on the influence of hydrological
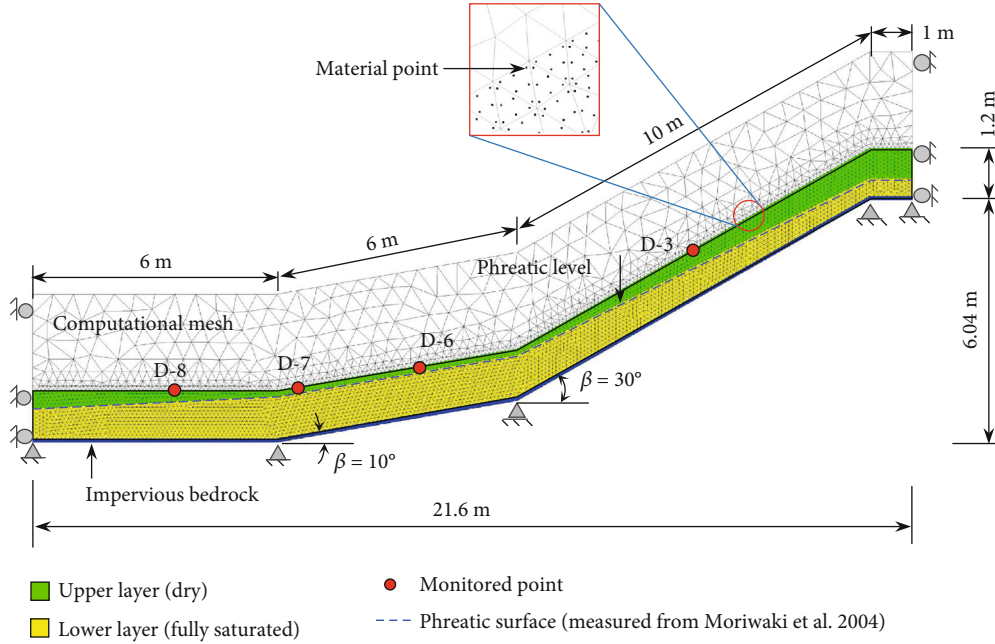
FIGURE 2: Initial geometry of the numerical model for the model validation.

TABLE 1: Material properties for numerical model validation.

| Parameters | Symbol | Sand | | Steel frame |
		Upper layer	Lower layer	
Material model		Dry	Saturated	Dry
Soil model		MC	MC	Linear
Porosity (-)	n	0.46	0.46	—
Solid density, (kg/m³)	ρ_s	2690	2690	7850
Liquid density, (kg/m³)	ρ_l	—	1000	—
Permeability, (m/s)	k_s	—	5×10^{-5a}	—
Bulk modulus liquid, (kPa)	K_L	—	2.15×10^4	—
Dynamic viscosity liquid (kPa.s)	μ_d	—	1×10^{-6}	—
Young's modulus, (kPa)	E	6000[b]	6000[b]	2.1×10^8
Poisson's ratio	υ	0.3	0.3	0.15
Effective cohesion (kPa)	c'	0	0	—
Effective friction angle (°)	ϕ'	34	34	—
Dilatancy angle (°)	ψ	0	0	—
Tensile strength (kPa)	σ_t	0	0	—

[a,b]Calibration parameters to match the observed.

condition, soil hydraulic, and soil mechanical parameters on the postfailure behavior and kinematics of landslides.

The aforementioned discussion motivated the authors to conduct a series of MPM analyses to investigate the postfailure process, failure mechanism, and kinematic behavior of shallow landslides related to infinite slope problems. The sensitivity of the hydrological condition, soil hydraulic, and soil mechanical parameters in the kinematics of shallow slopes is evaluated and quantified. This remaining paper is organized as follows: first, an introduction of kinematic MPM formulations for a two-phase single-point MPM formulation used in

the Anura3D MPM Research Community [32] is presented; subsequently, a validation of the MPM using the full-scale landslide flume test performed by Moriwaki et al. [33] is described; finally, a parametric study investigating the parameters influencing the postfailure kinematics of shallow slopes and a sensitivity assessment is detailed.

2. Methods and Validation

2.1. Basis of MPM Formulation. In this study, a two-phase single-point MPM formulation [34, 35] was used to represent
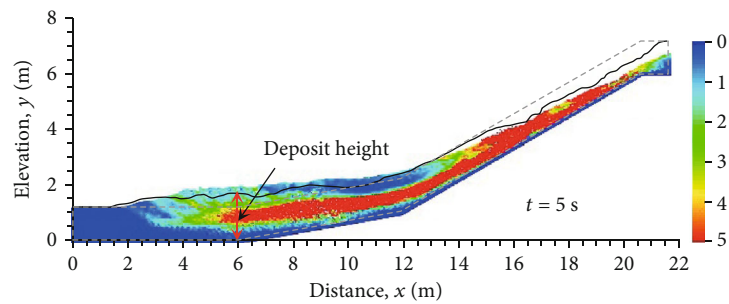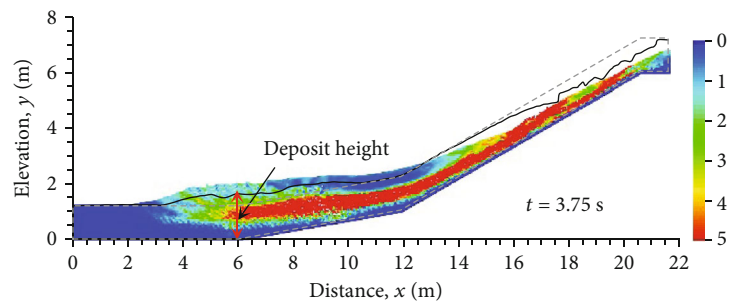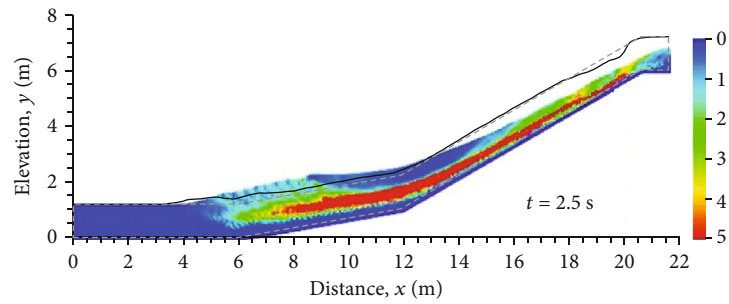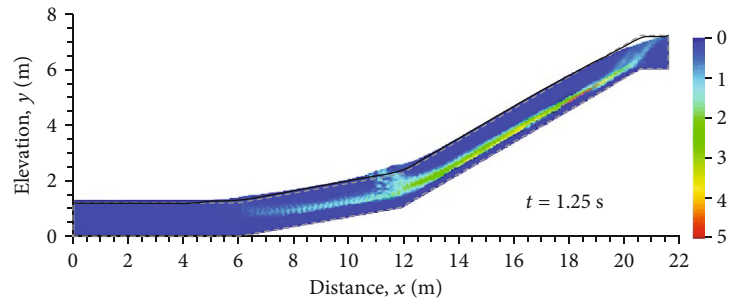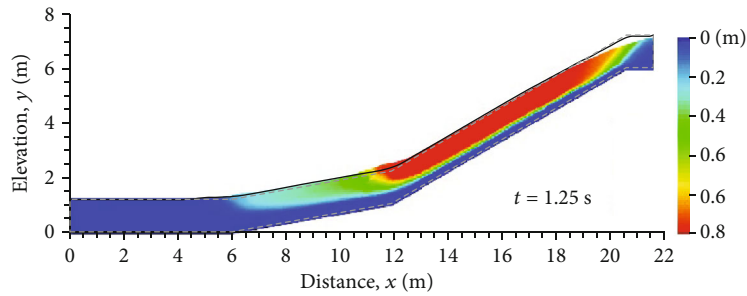
(a)

(b)

(c)

(d)

Figure 3: Continued.

(e)
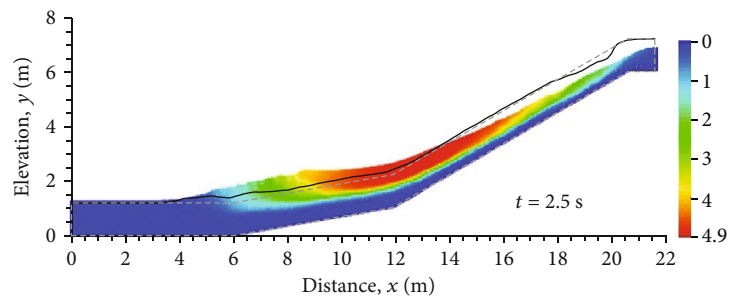
(f)

(g)
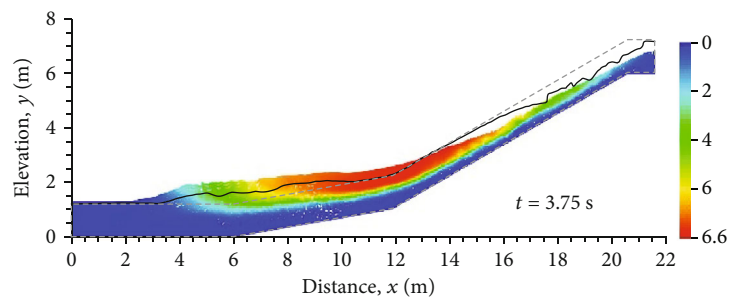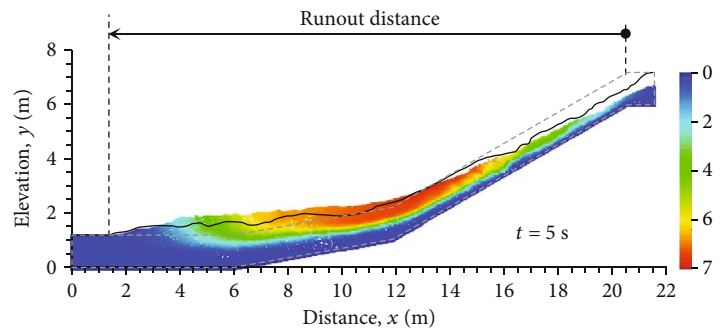
(h)

FIGURE 3: Comparison of the progress of the landslide between predicted and measured results in terms of: (a–d) deviatoric strain and (e–h) displacement contours.

(a)

Shear band

(b)

(c)
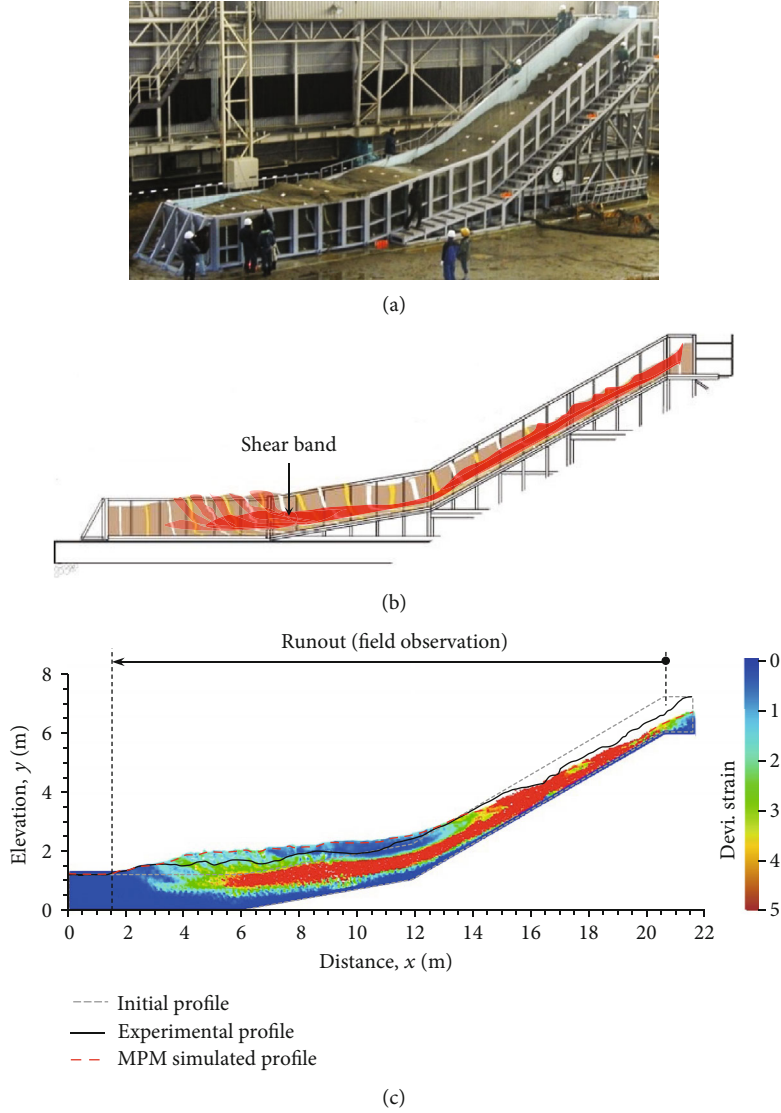
FIGURE 4: Comparison of predicted and measured final configuration and development of shear band: (a) photo of the experiment, (b) illustration from experiment results, and (c) prediction by MPM.

the saturated porous medium, where the governing equations of the mass and momentum conservations of both the solid and liquid phases were written by Fern et al. [36] as follows:

$$\frac{d\rho}{dt} + \rho\nabla v = 0, \tag{1}$$

where d/dt is the material time derivative, ρ is the material density, t is time, v is the velocity vector, and ∇ is the gradient operator.

The mass conservation for saturated soil is also known as the storage equation and can be expressed as

$$\frac{D^S \varepsilon_{\mathrm{vol},L}}{dt} = \frac{1}{n}[(1-n)\nabla.v_S + n\nabla.v_L], \tag{2}$$

where v_S and v_L are the velocities of the solid and liquid phases, respectively; n is the porosity of the solid skeleton; and $\varepsilon_{\mathrm{vol},L}$ is the volumetric strain of the liquid phase.

The momentum conservation for the mixture and liquid phase (per unit of liquid volume) is expressed in Eqs. (3) and (4), respectively.

$$(1-n)\rho_S \frac{dv_S}{dt} + n\rho_L \frac{dv_L}{dt} = \nabla.\sigma + [(1-n)\rho_S + n\rho_L]g, \tag{3}$$

$$\rho_L \frac{dv_L}{dt} = \nabla.p_L - f^d + \rho_L g, \tag{4}$$

$$f^d = \frac{n_L \mu_L}{\kappa_L}(v_L - v_S), \tag{5}$$

where ρ_S and ρ_L are the solid and liquid densities, respectively; σ is stress tensor; n_L is the volumetric concentration
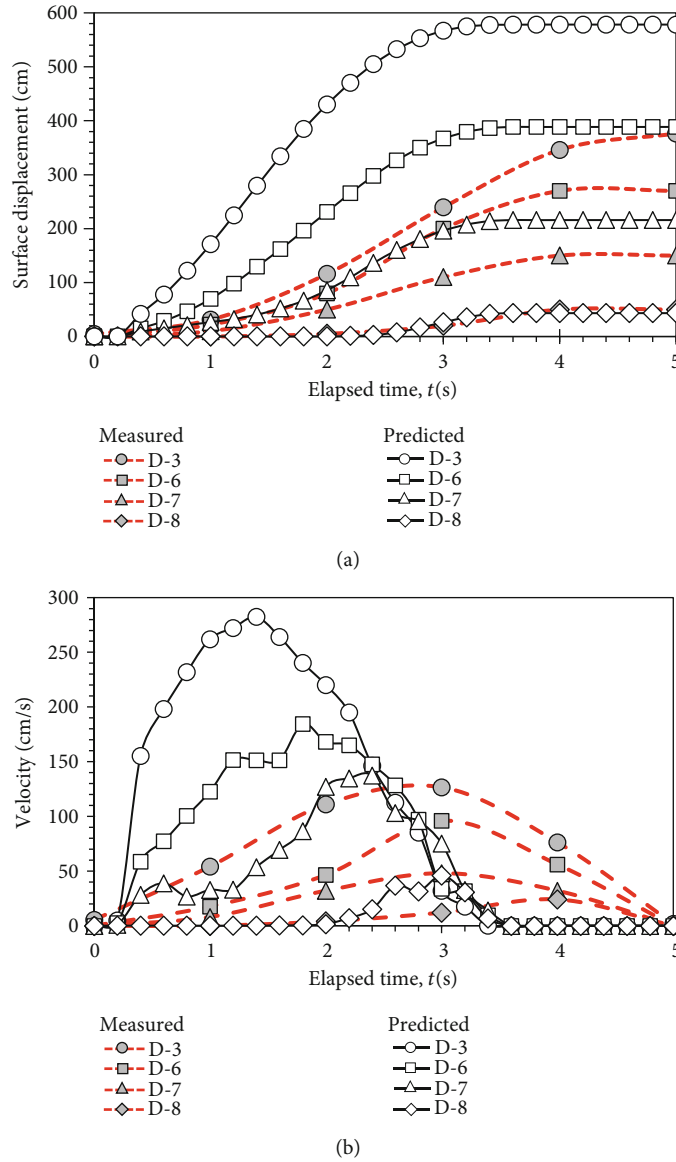
FIGURE 5: Comparison of predicted and measured (a) surface displacement and (b) velocity at different locations along the slope surface.

ratio of the liquid; p_L is liquid pressure; μ_L is the viscosity of the liquid; κ_L is the intrinsic permeability of the liquid; g is the gravitational acceleration vector; and f^d is the drag force, which represents the interaction force between the solid and liquid phases. Based on the assumption that flow is considered laminar and stationary in the slow velocity regime (i.e., linear), drag force can be defined using Eq. (5) with Darcy's law.

Figure 1 illustrates a computational cycle in the MPM. To solve the aforementioned momentum balance equation, the continuum body must first be spatially discretized by mapping information from the material points to the computational nodes of the mesh (referred to as the background computational mesh) (Figure 1(a)). At the beginning of each time increment, the momentum equations are solved on the predefined background mesh (i.e., the nodal accelerations) (Figure 1(b)). These nodal values are then used to update

the acceleration, velocity, and position of the material points within a newly generated background mesh (Figure 1(c)). Because no permanent information is stored in the mesh, it can be freely redefined at the end of the time step. Finally, the assignment of material points to elements is updated after the background mesh is reset for the next time step (Figure 1(d)). The governing equation, time discretization, and solution procedure of MPM were detailed by Fern et al. [36].

2.2. Model Validation.
To validate the proposed numerical model, the MPM result was compared against the results of a full-scale landslide flume test (Figure 2) conducted by Moriwaki et al. [33]. The real landslide case typically involves certain uncertainties associated with in situ conditions such as slope profile, hydrology, and subsurface ground conditions. Compared to real landslide cases, the reasons for selecting
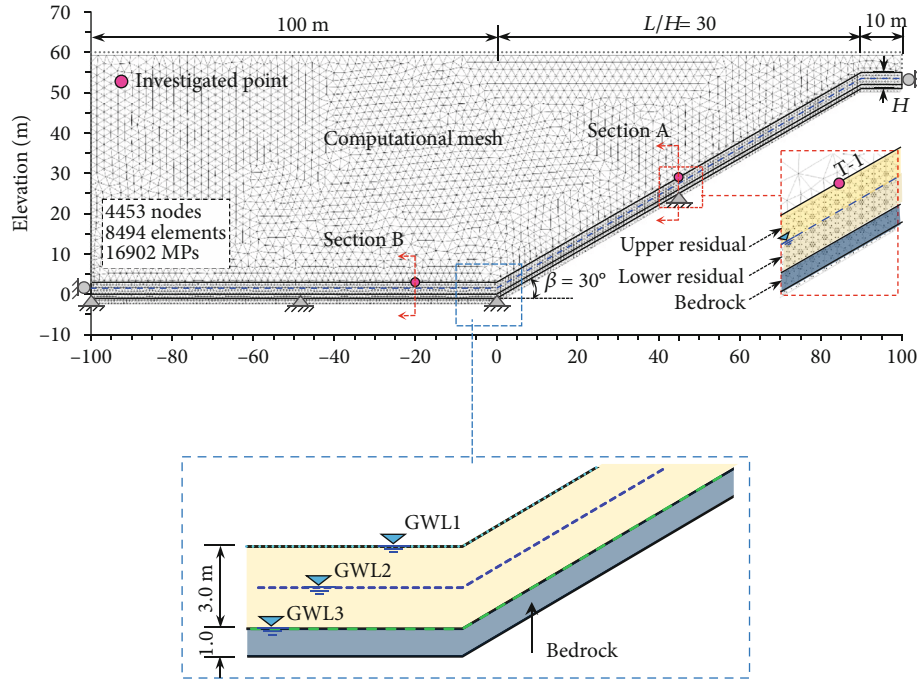
FIGURE 6: Initial geometry of the numerical model for the baseline case and parametric study (enlarged part shows three groundwater level using in the parametric study).

the experiment test reported by Moriwaki et al. [33] are because the selected experimental test was conducted in an indoor, well-controlled environment, resulting in better and more accurate test results for the use of the model validation. The model slope in the landslide flume test was 23 m long, 7.8 m high, 3 m wide, and 1.2 m deep, and the slope comprised three parts: an upper 30° slope segment, a lower 10° slope segment, and a horizontal segment at the toe of the model slope. The soil used in the test was loose Sakuragawa River sand, which is classified as a poorly graded sand (SP) according to the Unified Soil Classification System. A constant rainfall intensity of 100 mm/h was applied to the slope. A rapid landslide occurred on the 30° slope section 9267 s after the rainfall started. The collapsed soil mass slid downward and reached a final position within approximately 5 s from 9267 to 9272 s (postfailure stage). The test setup and experimental results were detailed by Moriwaki et al. [33].

Table 1 presents the mechanical properties of the input soil used in the MPM simulation. The soil properties of the Sakuragawa River sand were selected on the basis of those reported by Moriwaki et al. [33], Ghasemi et al. [37], and Yang et al. [38]. Sand behavior was analyzed using the elastic–perfectly plastic model. A 0.1 m thick steel flume was modeled as an impervious bedrock layer with a relatively high Young's modulus to ensure that it behaved as a rigid material.

Moriwaki et al. [33] observed the critical water table immediately before slope failure, and its modeling is presented in Figure 2. Therefore, in the initial geometry in the MPM, the slope configuration comprised two layers under the assumptions that, first, the dry material (one phase, single point) is part of the upper layer above the observed phreatic

surface at the time of failure and, second, the lower layer below the phreatic surface was a fully saturated material and was fully coupled (i.e., two-phase and single point). Slope deformation that occurred during the prefailure and failure stages was ignored. Figure 2 presents the initial geometry and discretization in the model validation. To obtain accurate results, the mesh was refined for sand material (i.e., element size of 0.1 m) because failure was expected to occur on the entire slope. The material point sizes were selected based on the relationship between the model height and the material point sizes for different cases of slope-related problems suggested by Llano-Serna et al. [1]. In total, 7567 elements and 3943 nodes with six material points per grid element were used in the model. Regarding boundary conditions, the bottom boundary was fully fixed, whereas roller boundaries were prescribed at the left and right sides of the model. The lateral and bottom models were impervious to the liquid phase. Because there is no information of interface friction coefficient reported by Moriwaki et al. [33], the frictional contact between the soil layer and bedrock was simply assumed to be full contact in the simulations.

The numerical simulation comprised two steps: (1) gravity loading to generate *in situ* stresses and (2) simulation of the 5 s propagation stage of the landslide. Because the Anura3D framework uses an explicit kinematic formulation to solve the governing equations [34], a time step of 0.1 s over 50 steps was used in the simulation to satisfy the requirements in the results. In the kinematic process, a local damping factor of 0.05 was used to simulate the slope failure, as suggested by Yerro et al. [30]. Furthermore, as reported by Abe et al. [39], during slope failure, an increase in pore pressure within the slope is synonymous with the change in soil

TABLE 2: Material properties for the analyses of the baseline case.

Parameters	Symbol	Shallow slope Upper residual	Lower residual	Bedrock[a]
Material model		Dry	Saturated	Dry
Soil model		MC	MC	MC
Porosity (-)	n	0.4	0.4	0.4
Solid density, (kg/m^3)	ρ_s	2650	2650	2350
Liquid density, (kg/m^3)	ρ_l	—	1000	—
Permeability, (m/s)	k_s	—	3×10^{-5}	—
Bulk modulus liquid, (kPa)	K_L	—	2.15×10^4	—
Dynamic viscosity liquid (kPa.s)	μ_d	—	1×10^{-6}	—
Young's modulus, (kPa)	E	10000	10000	20×10^6
Poisson's ratio	υ	0.3	0.3	0.3
Effective cohesion (kPa)	c'	1	1	500
Effective friction angle (°)	ϕ'	31.5	31.5	30
Dilatancy angle (°)	ψ	0	0	0
Tensile strength (kPa)	σ_t	0	0	5

[a]Assumed values based on Li et al. [46].

TABLE 3: Summary of the input property ranges of the parametric study.

Series of analyses	Description	Hydrological conditions Phreatic surface	Hydraulic property Saturated hydraulic conductivity k_s (m/s)	Mechanical properties Cohesion c' (kPa)	Friction angle ϕ' (°)	Soil modulus E (MPa)
Baseline		GWL2[b]	3.0×10^{-5}	1	31.5	10
	Influence of GWL	[GWL1[a] GWL3[c]]	3.0×10^{-5}	1	31.5	10
Parametric study	Influence of k_s	GWL2	[3.0×10^{-4} 1.0×10^{-5}]	1	31.5	10
	Influence of c'	GWL2	3.0×10^{-5}	[0, 7]	31.5	10
	Influence of ϕ'	GWL2	3.0×10^{-5}	1	[25, 37]	10
	Influence of E	GWL2	3.0×10^{-5}	1	31.5	[5, 20]

[a,b,c]Positions of the phreatic surface corresponding at the top, middle, and bottom of soil layer, respectively.

permeability and stiffness. Therefore, a calibration parameter for both soil stiffness and permeability was used in this study to match the observed runout distance and final configuration in the experiment.

Figure 3 shows the landslide process in terms of the development of the deviatoric shear strain and deformation contours at different time points. In general, the observed and predicted final slope configurations were consistent. Both the landslide flume test and numerical simulation indicated that failure occurs in two stages. At the first stage of failure initiation (Figure 3(a)), the shear band is mainly formed along the soil–bedrock interface in the upper slope, and the sliding failure is a translational slide. In the second stage, failures occur within the moving mass when the shear zone is fully extended from the end of the upper slope to the end of the lower 10° of the slope (Figures 3(b)–3(c)). The shear band appearing in the lower part of the 10° slope was more complicated than that of the upper part because of

the combination of compaction and shearing. As presented in Figure 3(h), the simulation results were consistent with the runout distance measured in the experimental test. At $t = 5$ s, the computed maximum depositional height was located near the toe of the 10° slope and was consistent with the experimental observations (Figure 4(a)). Figure 4 compares the simulated and observed shear band distributions in the final configuration. The kinematics of shear band development were similar to those observed in the MPM simulation.

Figure 5 shows the comparison between measured and predicted surface displacement and velocity for four monitored points on the slope surface. As illustrated in Figure 5, the predicted and measured surface displacement and velocity are close for the monitored points at the lower slope (i.e., D-7 and D-8), but the numerical results generally overly predicted both surface displacement and velocity at the upper slope (i.e., D-3 and D-6). The discrepancy is primarily

$t = 1$ s

(a)

$t = 5$ s

(b)

$t = 7.5$ s

(c)

$t = 25$ s

(d)
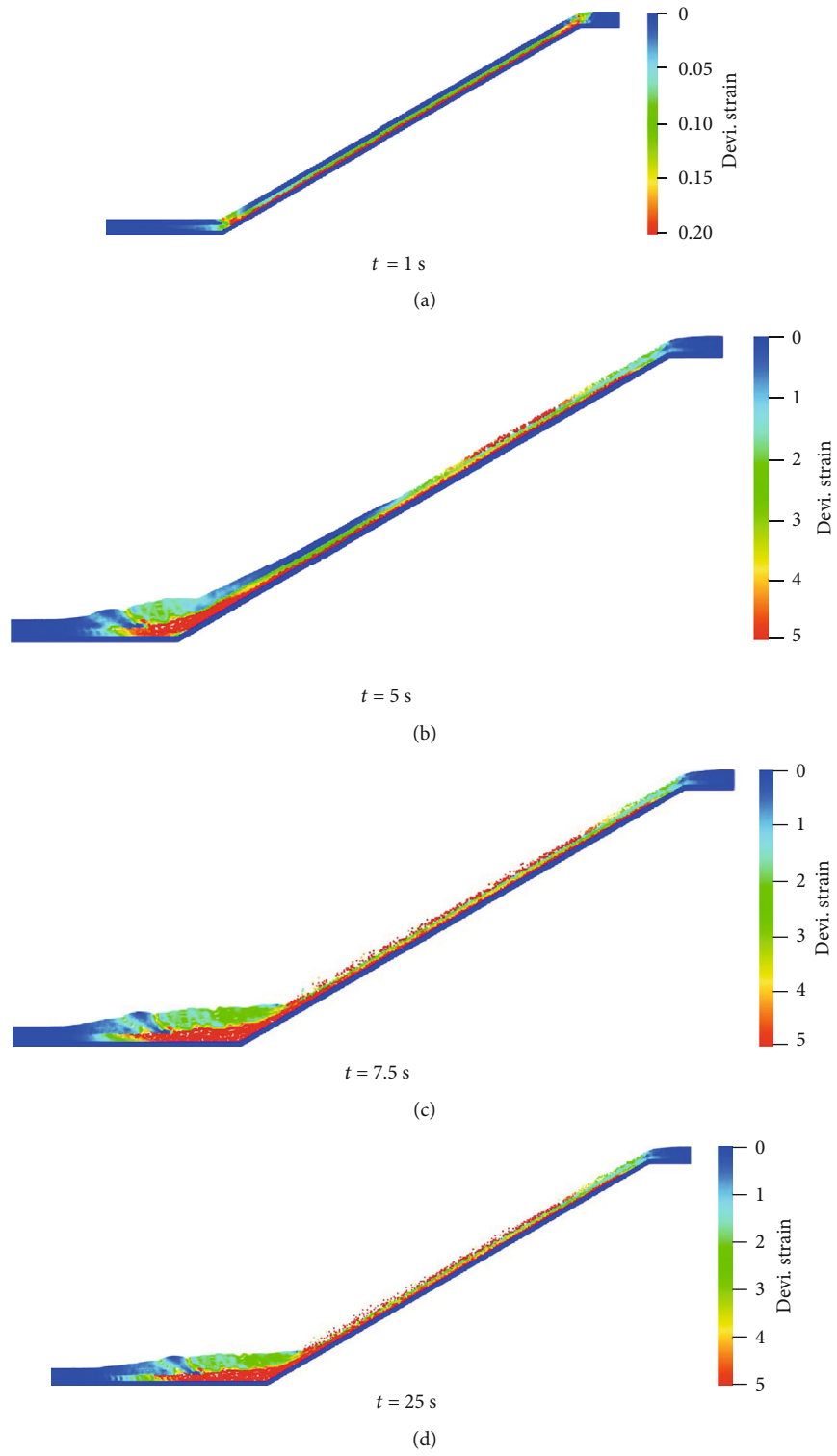
FIGURE 7: Continued.

$t = 1$ s

(e)

$t = 5$ s

(f)

$t = 7.5$ s

(g)

$t = 25$ s

(h)
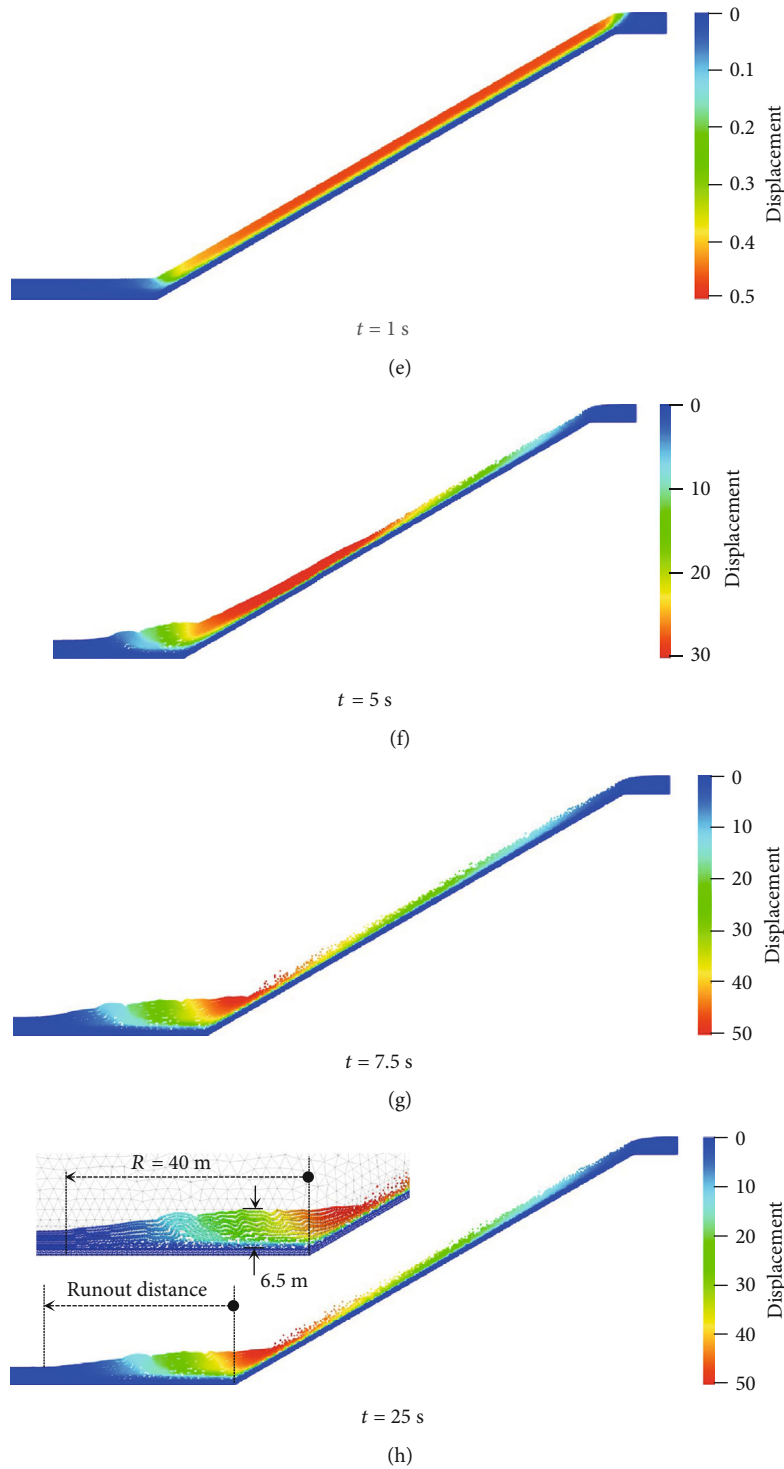
FIGURE 7: Progress of the landslide for baseline case in terms of: (a–d) deviatoric strain and (e–h) displacement contours at different times.

attributable to the change of soil parameters (i.e., soil modulus and permeability) under different loading conditions during the landslide process. As the landslide progresses, the soil at the upper slope is mainly under extension, while the soil at the lower slope is subject to compression. In reality, soils under different loading conditions may have different void ratios, resulting in different soil mechanical and hydraulic parameters. However, this effect of change of soil parameters

with soil void ratio (or loading conditions) is not modeled in this study due to the limitation of the current Anura3D MPM version. The above statement has been confirmed by conducting a trial simulation using different soil moduli and permeabilities for the soils at the upper and lower parts of the slope. The numerical results show the predicted and measured surface displacement and velocity match well for both the upper and lower parts of the slope. However, manually
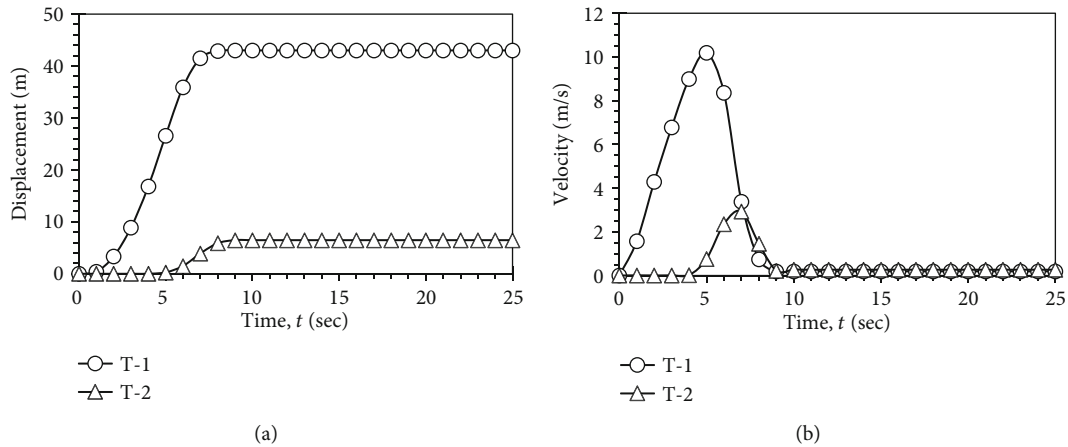
FIGURE 8: Variation of slope displacement and velocity with time: (a) displacement and (b) velocity.

inputting two different sets of soil properties for soils at the upper and lower part of the slope is not a rigorous numerical procedure, and, thus, the results are not presented in this paper. For a more rigorous numerical procedure, advanced MPM functions should be implemented to resolve this limitation; for example, considering two phases, two points function to allow the soil properties to vary with the soil void ratio.

3. Postfailure Behavior of Shallow Landslides

3.1. Numerical Model and Inputs. A shallow slope with a 3 m thick residual soil layer on top of the impermeable rock layer, a length of 90 m, and an incline of 30° (Figure 6) was adopted in this study to evaluate the influence of soil parameters and groundwater level on the postfailure characterization and kinematic behavior of shallow landslides. The slope model and input soil properties were designed according to the statistical data reported in a companion paper by Yang et al. [38]. In this study, the soil properties, the thickness of the residual soil, and slope angle used in this study were statistically determined from a large soil database (i.e., 57 soil types) compiled from 35 landslide case histories of the literature (see Table 6 in Yang et al. [38]). The datasets cover a wide range of soil types, including residual weathered soils and transported colluvium deposits worldwide. For example, more than 80% of the landslide cases in the collected landslide database have soil thickness ranging from 1 to 5 m. Based on the above statistical results, a 3 m thick soil layer, the average value of 1-5 m, was selected in this study.

For the slope geometry and boundary conditions, the ratio of slope length to soil thickness in the slope model (L/H) was 30, which is larger than the suggested ratio of 25 to ensure no interference from boundaries in the calculation [40]. In addition, the length of the horizontal section at the toe of the model was extended by 100 m to ensure that the soil travel distance was unaffected. To save computation time, only a 1 m thick layer of bedrock was imposed in the model. Moreover, the water table was assumed to be located in the middle of the soil slope (Figure 6). The model comprised two parts. The upper layer of soil (i.e., that above the water table) was assumed to behave as a dry material,

whereas the lower layer of soil was assumed to be fully saturated. The boundary conditions and numerical procedure were identical to those used in the validation model, which used a roller for the two side boundaries and a hinge for the bottom boundary.

The soil layer and bedrock were modeled under the assumption of the Mohr–Coulomb constitutive model with a nonassociated flow rule. During the analysis, the effective stress parameters under drained conditions were measured for the soil layer submerged in water by using the two-phase single-point MPM formulation. Figure 6 presents the geometric configuration and boundary conditions of the slope. The initial domain of the model was discretized using 8494 mixed triangular finite elements, 4453 mesh nodes, and 16902 material points in plane strain. The simulation lasted 25 s in total after landslide initiation.

The numerical analyses were performed in two series: a baseline case and a parametric study. For the baseline case, the input soil properties listed in Table 2 were obtained based on the mean soil property values from a previously compiled dataset of 35 landslide case histories in the literature [38]. A low soil cohesion value (i.e., $c' = 1$ kPa) was selected for the baseline case for a better observation of the postfailure behavior of landslide. For the parametric study, the effect of three groups of input parameters—namely, hydrological conditions (i.e., groundwater level), soil hydraulic parameters (i.e., saturated soil permeability), and soil mechanical parameters (i.e., soil friction angle, cohesion, and Young's modulus)—on postfailure behavior such as travel distance and velocity was evaluated. In each case, only one parameter was manipulated, and all other parameters were constant in the baseline case. In total, 11 cases of numerical simulations were performed in this study (Table 3). The soil property values within one standard deviation (SD) of the mean ($\mu \pm$ SD) from the landslide database [38] were selected in the parametric study. If $\mu -$ SD was negative or unreasonable, the minimum value of the parameter from the landslide database was used as the lower bound.

3.2. Baseline Case. Figure 7 presents the evolution of slope failure in the baseline case at $t = 1, 5, 7.5, 10,$ and 25 s in terms
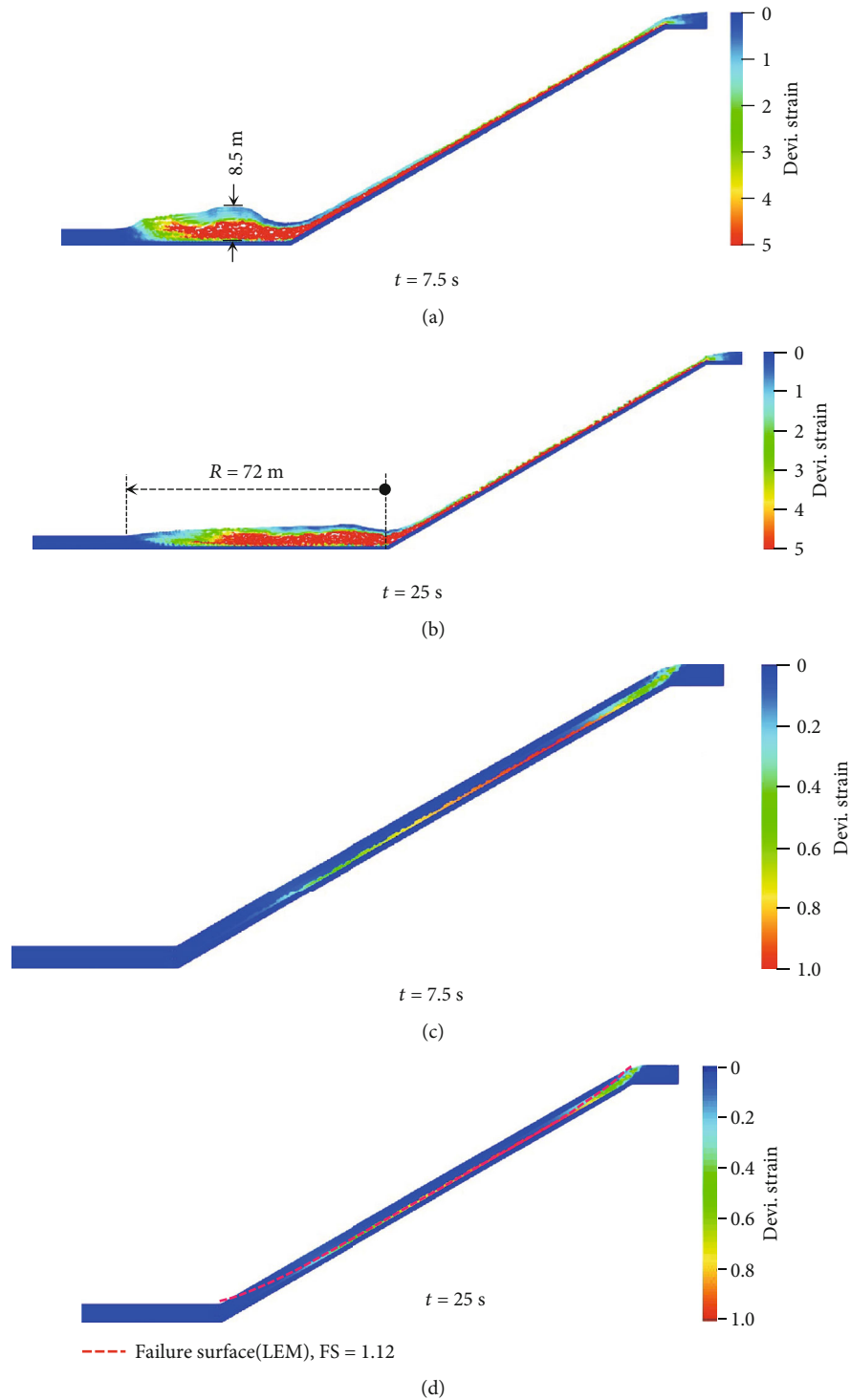
FIGURE 9: Effect of groundwater level on the post-failure behavior of a slope: (a, b) GWL1 and (c, d) GWL3.

of the deviatoric strain and displacement contours. At the start of the failure stage (Figure 7(a)), the shear strain developed evenly along the soil–bedrock interface on the slope section, and the sliding failure surface extended from the crest to the toe of the slope. The failure mode was categorized as a translational sliding failure. Over time, the landslide mass moved rapidly down the slope along the inclined surface to the toe and extended to the horizontal part of the slope as a complex failure surface. Displacement within a new sliding failure increased in each successive stage (Figure 7(e)–7(h)). Figure 7(d) presents the slope situation at $t = 25$ s, when the sliding failure on the slope was complete. Similar to the results observed in the model validation presented in Section 2.2, the distribution of shear strain in the horizontal part of the slope was affected by combined soil compression and shearing with the formation of multiple

(a) Effect of GWL

(b) Effect of k_s

(c) Effect of c'

(d) Effect of ϕ'

(e) Effect of E

(f) Effect of GWL

(g) Effect of k_s

(h) Effect of c'

(i) Effect of ϕ'

(j) Effect of E
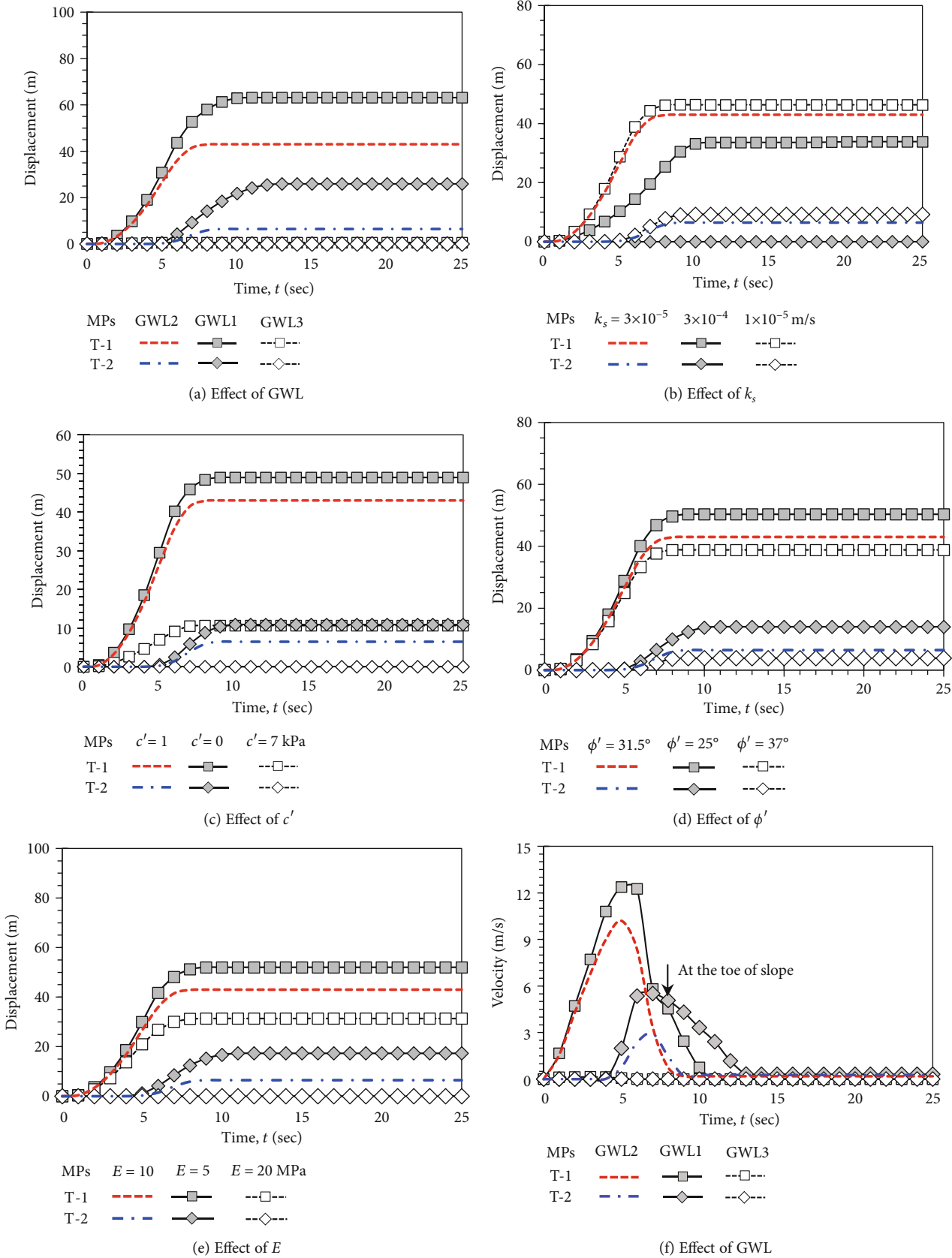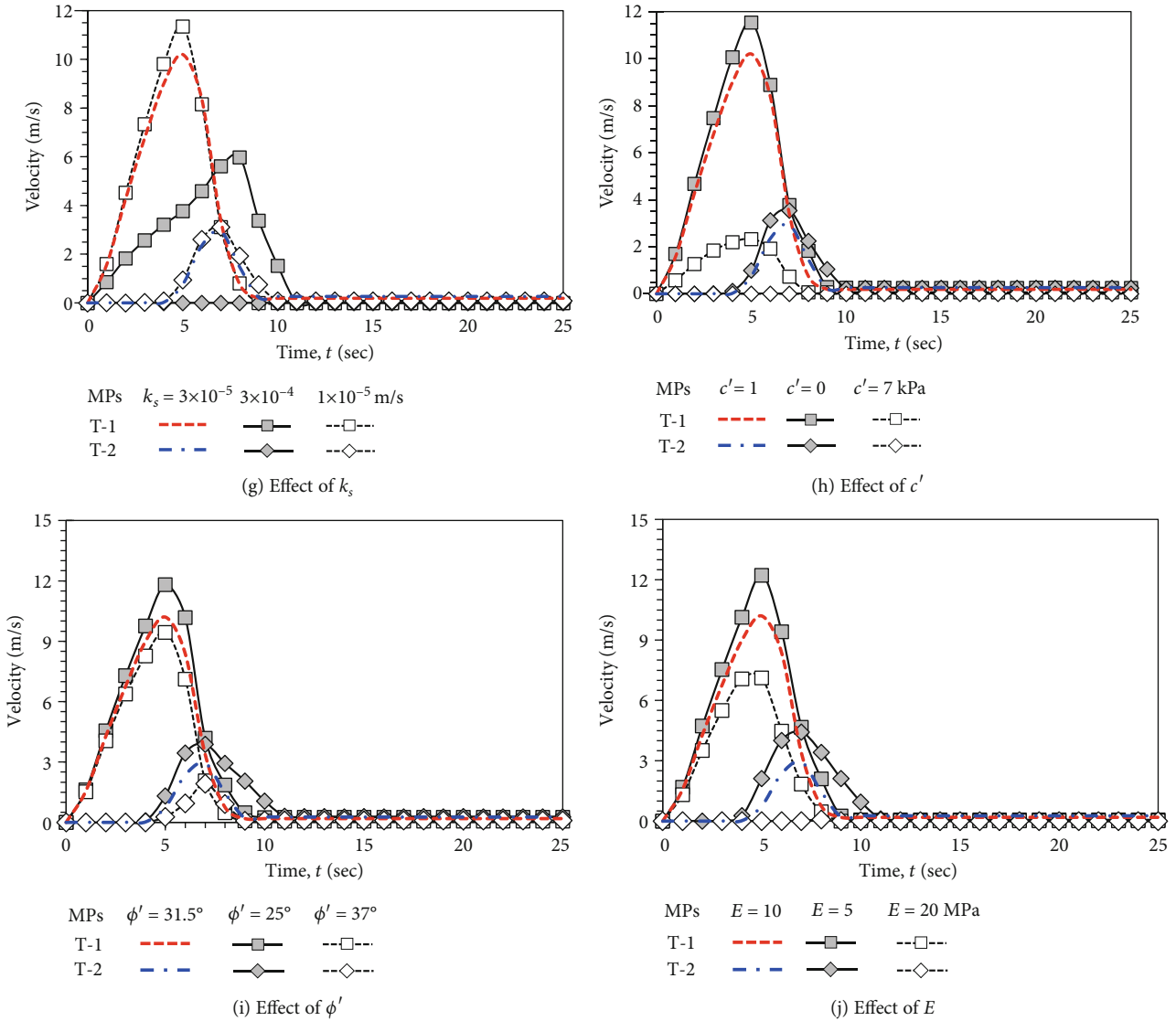
FIGURE 10: Influence of different input parameters on the variation of slope displacement and velocity with time: (a–e) displacement and (f–j) velocity.

plastic shear bands. Figure 7(h) presents the final slope displacement. The runout distance, which was measured in terms of particle movement, was approximately $R = 40$ m, and the ratio of landslide height to travel distance (H_h/L_d) ratio was 0.4.

To highlight the kinematics of the failure, Figure 8 displays a comparison of the displacement and velocity evolutions over time at material points T-1 and T-2 on the slope surface (Sections A and B in Figure 6(a)). In the numerical simulation, the soil mass on the 30° slope moved rapidly downward at a calculated maximum velocity of 10.2 m/s. Subsequently, (1) the kinetic energy of the slope decreased over time because shearing occurred between the flowing and deposited material at the horizontal section, and (2) the slope stabilized after $t = 10$ s (i.e., when slope failure was complete). The maximum thickness of the deposited material was 6.5 m in the final deposition profile (Figure 7(h)). Notably, the movement speed of material points on the 30° slope

section was three times that of the material points in the horizontal section, and the magnitude of the runout and the maximum displacement of points on the slope surface were similar in this study.

3.3. Parametric Study

3.3.1. Effect of Water Table Location. To measure the effect of water table position, three positions on the phreatic surface (hereafter referred to as GWL) were adopted in the analysis, namely, GWL1, GWL2, and GWL3, which corresponded to the top, middle, and bottom of the soil layer, respectively (Figure 6(b)). The material model for the soil layer was assumed to be saturated-fully coupled and dry the corresponding water table was located at the surface slope (i.e., GWL1) and at the soil–bedrock interface (i.e., GWL3), respectively. Section A in the middle part of the slope and section B at 20 m away from the toe of the slope were selected

$t = 5\,\mathrm{s}$

(a)

$R = 8\,\mathrm{m}$

$t = 25\,\mathrm{s}$

(b)

$t = 5\,\mathrm{s}$

(c)

$R = 47.5\,\mathrm{m}$

$t = 25\,\mathrm{s}$

(d)
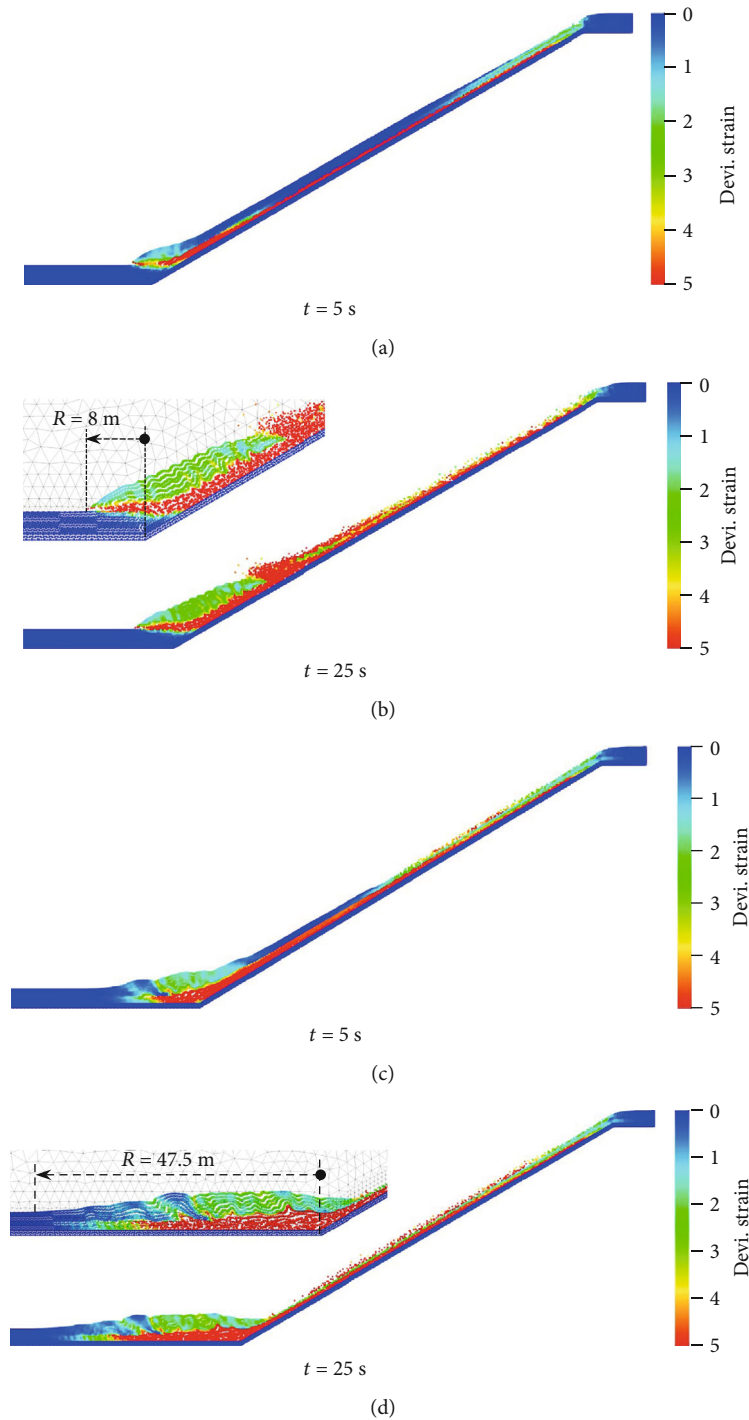
FIGURE 11: Effect of saturated permeability on the post-failure behavior of a slope: (a, b) $k_s = 1 \times 10^{-4}\,\mathrm{m/s}$ and (c, d) $k_s = 1 \times 10^{-5}\,\mathrm{m/s}$.

to present the numerical results. In addition, the two quantities of runout distance (R), which was defined as the distance between the end of the displaced material after failure and the toe of the initial slope, and the ratio of landslide height to travel distance (H_h/L_d) were used to evaluate the postfailure process in the present study.

Figure 9 depicts the failure evolution for both cases with contour plots of the deviatoric shear strain. The kinematic behavior of the slope after failure was significantly affected

by water table location. In the GWL1 case, the deviatoric shear strain distribution in the horizontal slope section was significantly longer than that in the baseline case (i.e., GWL2). The final runout distance increased to approximately 72 m, and the corresponding H_h/L_d was 0.32. At $t = 7.5\,\mathrm{s}$, the maximum depositional height increased by more than 30% to 8.5 m relative to the baseline case. This likely occurred because (1) excess pore water pressure caused by the large distortions formed after slope failure and (2) the soil

(a)

(b)

(c)

(d)
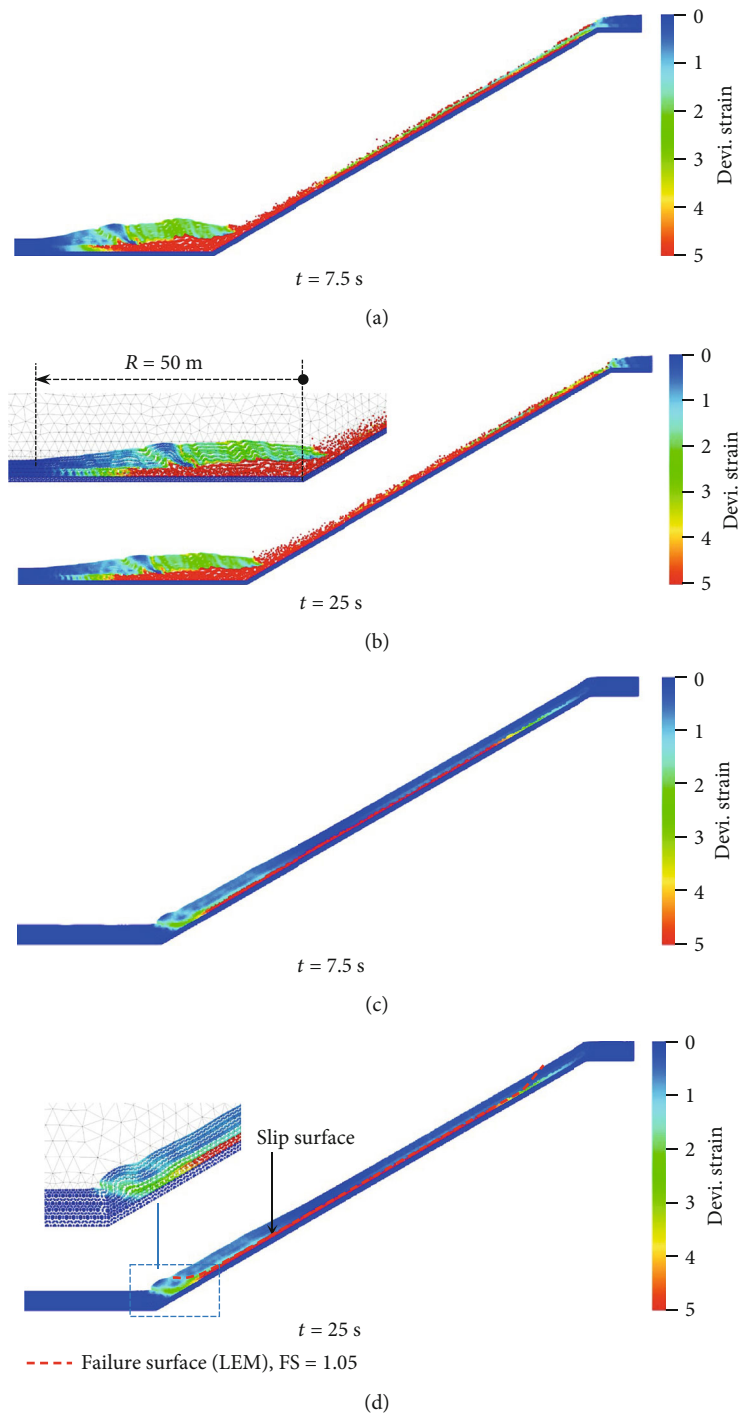
FIGURE 12: Effect of soil cohesion on the postfailure behavior of a slope: (a, b) $c' = 0$ kPa; (c, d) $c' = 7$ kPa.

weight increased as the entire slope became saturated. Figure 9(b) illustrates the evolution of the shear strain contours for the GWL3 case. In contrast to the GWL1 case, the postfailure process in the slope did not occur when the phreatic surface level dropped to the base of the soil layer. This occurred because the initial slope conditions exhibited a minimum factor of safety (FS) larger than 1.0 (stable condition). Because the MPM used in this study cannot provide information related to slope stability, the initial FS

value herein was calculated using the LEM. The obtained FS was 1.12 (Figure 9(d)).

A comparison of velocity at material points T-1 and T-2 between the GWL1 and GWL3 cases is presented in Figures 10(a) and 10(f). The GWL1 case exhibited a rapid development of velocity in the sliding particles on the slope. The velocity of point T-1 peaked at 12 m/s at 5 s (Figure 10(f)); this was much higher than the 0.15 m/s peak in the GWL3 case. Notably, unlike the baseline case, after

$t = 3$ s

(a)

$t = 7.5$ s

(b)

$R = 54$ m

$t = 25$ s

(c)

$t = 3$ s

(d)

$t = 7.5$ s

(e)
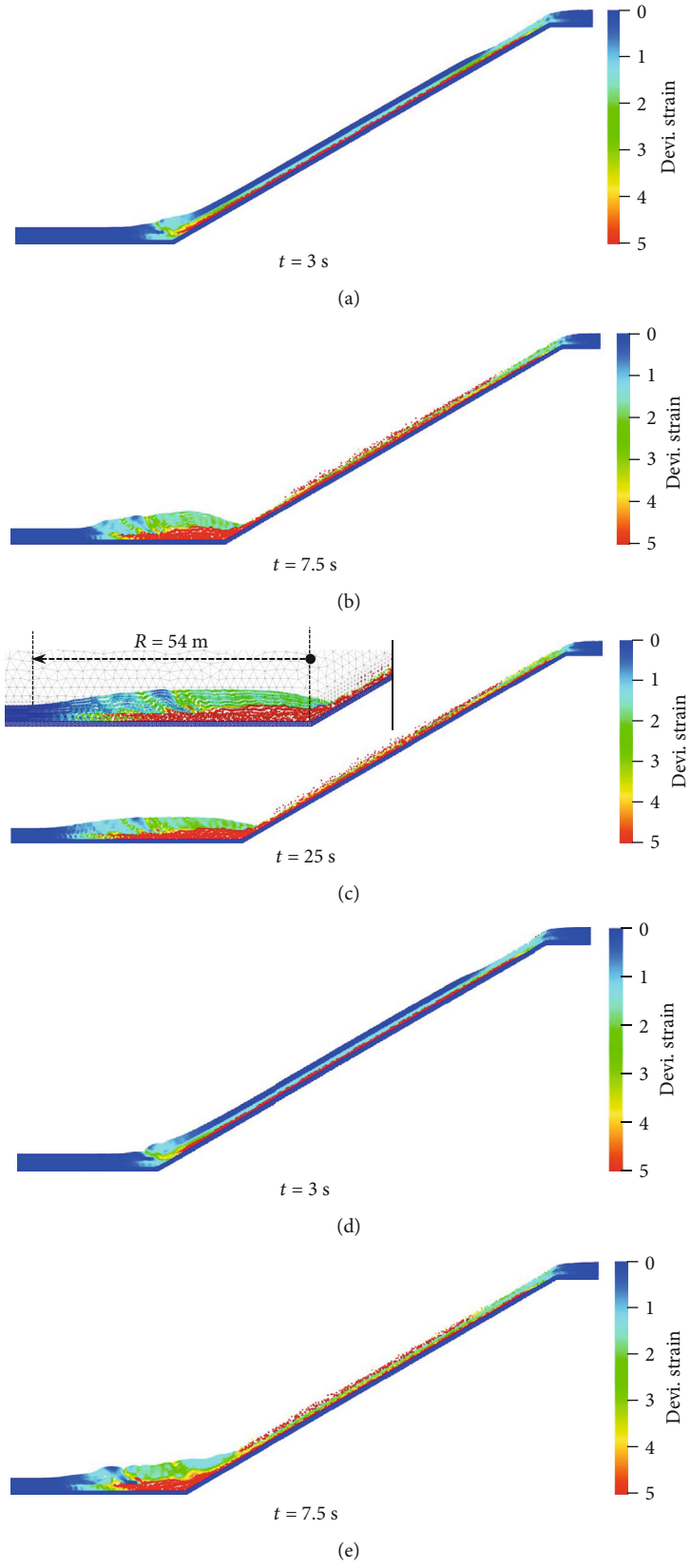
FIGURE 13: Continued.

$t = 25$ s

(f)
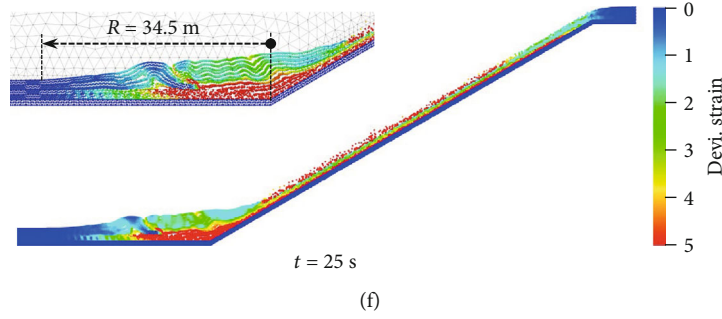
FIGURE 13: Effect of soil friction angle on the postfailure behavior of a slope: (a–c) $\phi' = 25°$ and (d–f) $\phi' = 37°$.

reaching a peak, the velocity of point T-1 exhibited a slight discontinuity at $t = 8$ s when the material points moved to the toe of the slope. As illustrated in Figure 10(f), a new equilibrium of the slope was established after $t = 15$ s. As previously observed in the GWL3 case, because runout did not occur in this case, the displacement and velocity of point T-2 on the horizontal section of the slope was close to zero.

3.3.2. Effect of Soil Permeability. Regarding the effect of saturated hydraulic conductivity, as soil permeability increased, deformation decreased considerably (Figure 11). For the slope with high permeability (i.e., $k_s = 3 \times 10^{-4}$ m/s), the failure plane in terms of deviatoric shear strain formed clearly on the 30° slope section (Figure 11(a)). In the final configuration (Figure 11(b)), the runout (R) was approximately 8 m. By contrast, the slope with low permeability exhibited substantially increased deformation with a maximum runout distance of approximately 47.5 m. This result occurred because, during kinematic postfailure, the generated pore water pressure increment in the slope with low permeability was larger than that in the slope with high permeability. The numerical results are consistent with the findings of Ghasemi et al. [37]. Notably, when $k_s = 1 \times 10^{-5}$ m/s, the final deposit profiles did not differ significantly between the simulated and baseline cases. In other words, when the permeability coefficient was less than a certain value, the final configuration was not affected by changes in k_s. However, low soil permeability can significantly increase computation time, and this finding is consistent with that of Yerro et al. [29].

A comparison of the evolutions of deformation and velocity at different k_s values are presented in Figures 10(b) and 10(g). Both velocity and deformation considerably decreased as k_s increased. Compared with a slope with high permeability (i.e., $k_s = 3 \times 10^{-4}$ m/s), the velocity at material point T-1 doubled when $k_s = 10^{-5}$ m/s. In addition, as illustrated in Figure 10(g), the time to peak velocity for a slope with a high k_s was 8 s, which was longer than the 5 s observed for the slope with a low k_s. Overall, the numerical results indicated that permeability considerably influences the kinematic behavior and soil movement of slopes after the failure stage. Slopes with high k_s values appeared more stable than those with low k_s.

3.3.3. Effect of Soil Mechanical Parameters

(1) Effect of Soil Cohesion. Regarding the influence of soil shear strength, the kinematic behavior of slopes was strongly

affected by soil cohesion and moderately affected by soil friction angle. Figure 12 presents the influence of soil cohesion values (i.e., $c' = 0$ and 7 kPa) on the final configurations of slope collapses. Generally, slopes with low effective soil cohesion had larger deformations. For the slope with noncohesive soil ($c' = 0$ kPa), the behavior of the material on the slope section resembled that of a granular flow [41–45] with extremely large deformation. No distinct shear band was observed in the slope with noncohesive soil, and the time required to reach a new equilibrium condition ($t > 10$ s) was longer than that of a slope with cohesive soil. As illustrated in Figure 12(b), the final runout distance for a slope with $c' = 0$ kPa was 50 m, and the corresponding H_h/L_d was 0.37. Similar to the GWL3 case discussed earlier, for a slope with $c' = 7$ kPa, the FS value of 1.05 obtained using the LEM confirmed that the initial state of the slope was stable, and the runout distance was not observed. The shear strain distribution (Figure 11(b)) was mainly observed on the 30° slope section along the soil–bedrock interface, and it did not extend to the horizontal part. Compared with the baseline case ($c' = 1$ kPa) and the previous case with $c' = 0$ kPa, low cohesion resulted in a shallow slip failure surface, whereas higher cohesion resulted in a deeper sliding failure. Yerro et al. [30] and Shi et al. [22] also obtained similar findings.

The kinematics of the landslide were evaluated using the displacement and velocity evolution of the material points (i.e., T-1 and T-2), as presented in Figures 10(c) and 10(h). The velocity and displacement in the slope with $c' = 0$ kPa were clearly more serious than those of other cases. For a slope with noncohesive soil, the speed of the mass movement on the slope was five times that of movement on the slope with high cohesion (Figure 10(h)). Notably, the time required to reach the peak value (i.e., $t = 5$ s) was unaffected by the cohesion value. In addition, as observed in Figure 10(c), no displacement of material point T-2 occurred in the horizontal section of the slope when $c' = 7$ kPa. In conclusion, soil cohesion substantially affected the postfailure landslide process.

(2) Effect of Soil Friction Angle. The effect of internal friction angle on runout postfailure characteristics was also investigated. Figure 13 compares several slope failure evolutions in terms of deviatoric strain for two soil friction angles (ϕ'), 25° and 37°. As expected, the larger the internal friction angle, the weaker the movement of the sliding mass was. For both

$t = 5$ s

(a)

$t = 7.5$ s

(b)

$R = 64$ m

$t = 25$ s

(c)

$t = 5$ s

(d)

$t = 7.5$ s

(e)
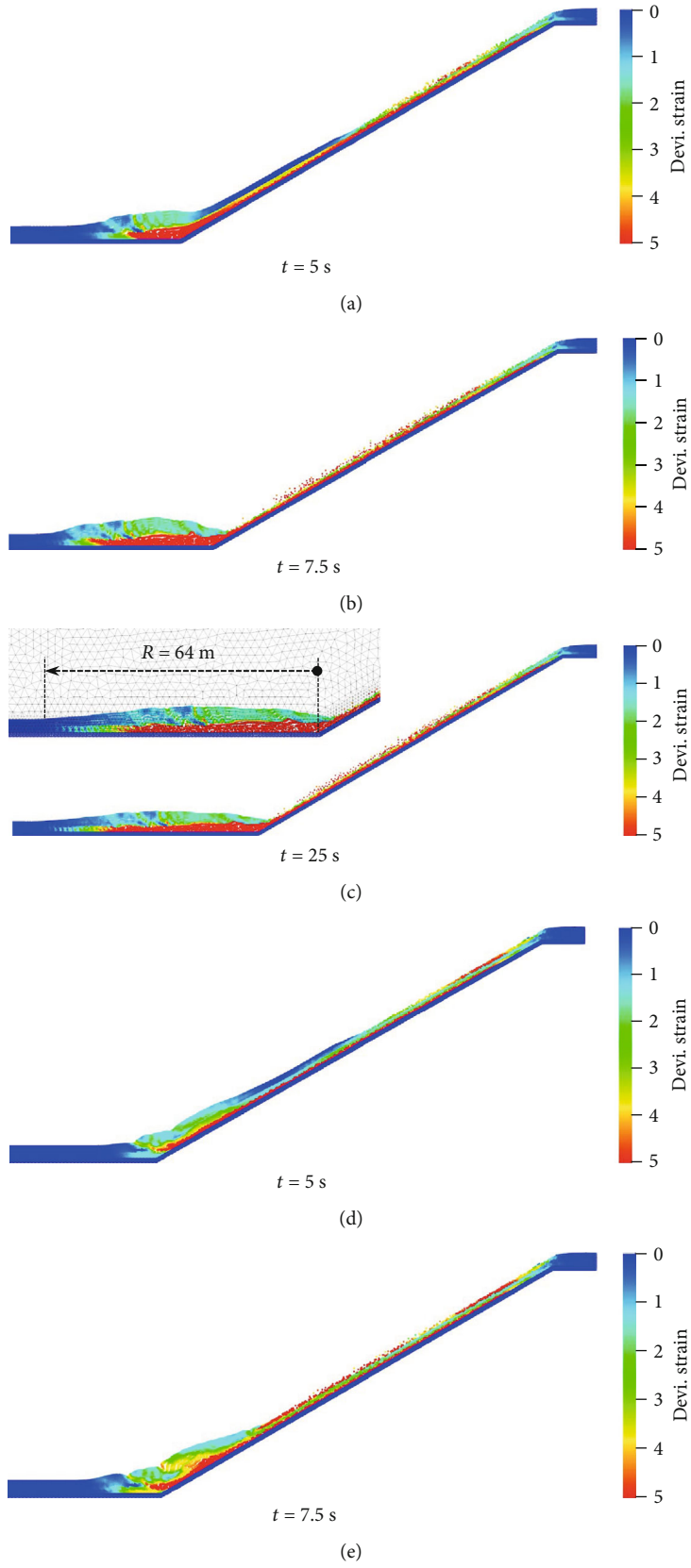
FIGURE 14: Continued.

$t = 25$ s

(f)
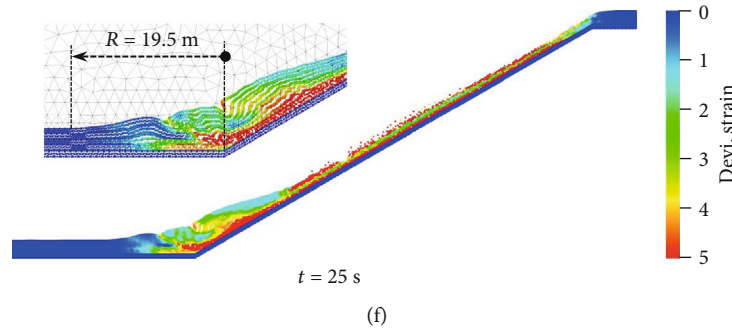
FIGURE 14: Effect of soil modulus on the post-failure behavior of a slope: (a–c) $E = 5$ MPa and (d–f) $E = 20$ MPa.

friction angles, when the failure stage initiated, the shear strain was concentrated mainly along the soil–bedrock interface (Figures 13(a) and 13(d)). However, the sliding of the landslide body toward the slope toe caused compressive forces in the soil mass in the horizontal portion. Consequently, a significant difference in the shear strain evolution was observed in the horizontal section at the final stage between the two friction angles. When $\phi' = 37°$, because of the smaller effect of the soil mass moving from the slope part and the higher soil resistance in the horizontal part, a shorter shear band at the soil–bedrock interface in the horizontal part of the slope was observed. By contrast, at a small internal friction angle, weak resistance in lateral support caused the sliding mass to accumulate in the horizontal part at $t = 7.5$ s. After 7.5 s, the shear strain continued to expand along the soil–bedrock interface in the horizontal section. The maximum calculated runout distances were 54 m and 34.5 m for $\phi' = 25°$ and 37°, respectively.

The displacement and velocity evolutions of monitored points for various friction angles are presented in Figures 10(d) and 10(i). For different ϕ' values, the evolutions of displacement and velocity were similar in the 30° slope section. The maximum velocity decreased as the friction angle increased, and the velocity stabilized at approximately 12 and 9 s for the friction angles of 25° and 37°, respectively. Notably, in contrast to soil cohesion, soil friction angle had ostensibly little influence on postfailure characteristics (Figure 10(i)). Additionally, the sliding failure surface and time required to reach peak velocity (i.e., 5 s) were similar for different friction angle values.

(3) Effect of Soil Modulus. Regarding the influence of soil modulus on postfailure behavior, the evolutions of slope failure at three times points in terms of deviatoric strain contours for different Young modulus values (E) are illustrated in Figure 14. Similar to the influence of soil mechanical parameters, the shape of the final deposition profile of the landslide body was greatly influenced by changes in soil stiffness. The runout distance and deposition height substantially increased as the soil modulus decreased. When $E = 5$ MPa, the maximum simulated depositional height was 7.5 m at $t = 7.5$ s; by contrast, this value was only 5.8 m when $E = 20$ MPa. The difference was due to the change in the Young modulus that affected the effective stress distribution and generation of excess pore water pressure during slope failure. Figures 14(c) and 14(f) depict the final configuration of two simulations with different E values. Similar to the previous cases, the slope with a low Young modulus (i.e., $E = 5$ MPa) exhibited multiple shear zones in the horizontal part during failure. The final runout distance was approximately 64 m, and H_h/L_d ratio was 0.34; by contrast, the maximum horizontal runout distance for the slope with $E = 20$ MPa was approximately 19.5 m, and the H_h/L_d ratio was 0.48. These observations imply that the final configuration is highly sensitive to the value of the Young modulus.

The influence of E on the velocity and displacement evolution of two monitored points over time is presented in Figures 10(e) and 10(j). For both values of E, velocity peaked at $t = 5$ s after the start of the slope failure simulation (Figure 10(j)). As expected, the numerical simulations indicated that both the velocity and displacement of sliding failure considerably decreased as the soil modulus increased. For example, the computed maximum velocity of material point T-1 was 12.2 m/s when $E = 5$ MPa and was larger than that of the baseline case (10.2 m/s), whereas this value was only 7.3 m/s when $E = 20$ MPa.

4. Sensitivity Assessment

Identifying the most influential factor affecting the kinematic behavior of slopes after failure is crucial in landslide risk assessment. A sensitivity analysis of variables, such as soil hydrological and soil mechanical parameters, was performed to identify the influence of each parameter on the maximum velocity and runout distance. Figure 15 presents the sensitivity analysis results in terms of the percent change in maximum velocity and runout distance versus the percent change in input parameters. The results indicate that all input parameters influenced the postfailure behavior of the slope. Among the aforementioned parameters, c' and phreatic level location (i.e., GWL) had the greatest effect on runout distance, followed by E and k_s (Figure 15(a)). For instance, an increase in soil cohesion by up to 600% from its initial value resulted in a decrease in runout distance by up to 100%. Similarly, the runout distance decreased by 80% and 51% when k_s and E were increased by 10 times (i.e., 900%) and 2 times relative to the baseline case, respectively.
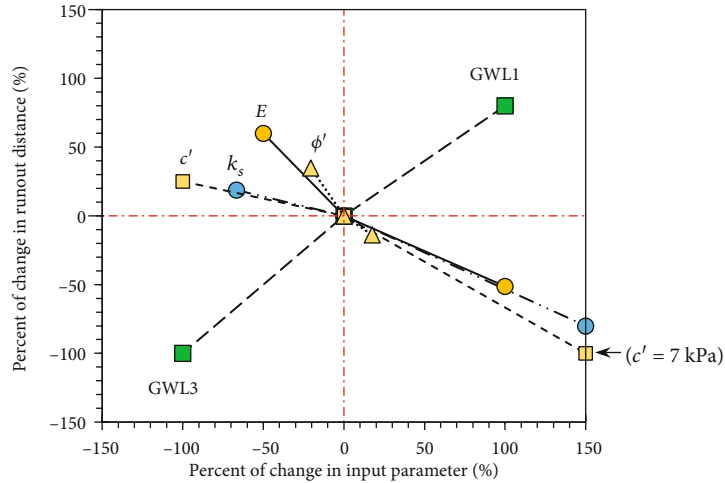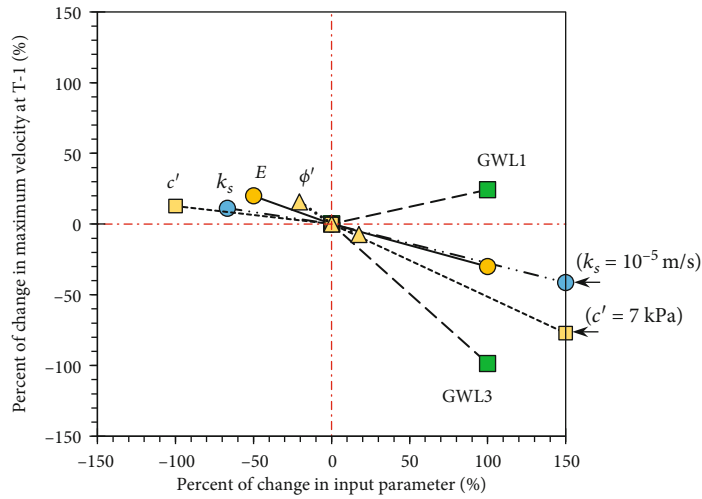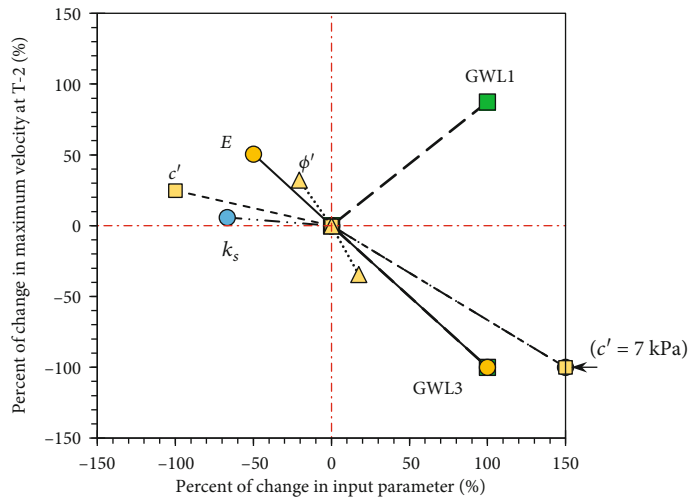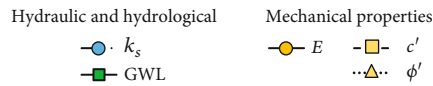
FIGURE 15: Results of sensitivity assessment in: (a) runout distance, (b) velocity of T-1, and (c) velocity of T-2.

Figures 15(b) and (c) indicate that all input parameters, including k_s, E, c', ϕ', and GWL, considerably affected the velocity of the tracked material points. The sensitivity assessment revealed that the velocity of material point T-1 on the 30° slope section was mainly affected by k_s, E, c', and GWL (Figure 15(b)). The velocity of T-1 decreased by 29% and 77% when E and c' were increased by 100% and 600%, respectively. Compared with material point T-1, the sensitivity of input parameters to the velocity of T-2 differed substantially with larger percent changes in velocity (Figure 15(c)). Notably, the sensitivity of the friction angle on the kinematic behavior of the slope was the lowest. A reduction or increase in friction angle by 20% changed the velocity of T-2 by ±33%, and runout distance increased by 35% and decreased by 14% relative to the baseline case, respectively. This was attributable to the negligible contribution of $\tan(\phi')$ on the shear strength of the soil when the change in the internal friction angle is small. In summary, the results of the sensitivity assessment suggested that the kinematic behavior and soil movement of slopes at the postfailure stage are highly sensitive to phreatic level location (GWL), hydraulic parameters (k_s), soil cohesion (c'), and the Young modulus (E).

The landslides simulated in this paper are hypothetical cases based on the landslide case histories compiled from the literature; therefore, the present results discussed in this study still cannot be directly applied or related to real landslides. However, this study identifies several important factors, such as phreatic level location, k_s, c', and E, which can have a significant influence on the postfailure characterization and kinematic behavior of shallow landslides. These findings highlight the importance of obtaining the reliable values of these parameters and quantifying their uncertainties for a better prediction in the kinematic behavior of shallow landslides.

5. Conclusions

In this study, MPM formulations were used in an investigation of the failure mechanism, kinematic behavior, and postfailure processes of unstable shallow slopes. The influences of hydrological conditions, soil hydraulic parameters, and soil mechanical parameters on the kinematic behavior of a failure mass were evaluated in terms of deviatoric strain, displacement, velocity, and runout distance. The effects of each parameter on velocity and runout distance were quantitatively compared in a systematic sensitivity assessment. The following conclusions were drawn based on the numerical results.

(1) The numerical model validation indicated that the MPM can effectively model situations that feature extremely large deformation. The runout distance and the shape of the final configuration in the simulation were consistent with the experimental data, demonstrating that the Mohr–Coulomb model used in the present study can describe material behavior

(2) The numerical results indicated that the slip failure surface for shallow slopes constitutes a translational slide in the slope section. Additionally, the failure mechanism in the horizontal section is complex and generates multiple plastic shear bands

(3) The parametric study and sensitivity assessment results revealed that all input parameters (i.e., hydrological conditions and soil hydraulic and soil mechanical parameters) considerably influence the kinematic postfailure processes. Among these parameters, c' had the largest effect on runout distance. The magnitude of runout distance decreases with increasing soil cohesion. The behavior of a slope with noncohesive soil (i.e., $c' = 0\,\mathrm{kPa}$) resembles a flow process with relatively high velocity in the sliding mass

(4) Regarding the kinematic behavior of slopes in terms of velocity and displacement, the numerical results indicated that when the failure mechanism is shallow, the magnitudes of maximum surface displacement on the slope and runout distance are similar. For all slope cases, the velocity of the material points in the middle of the slope reached peak values at the same time (i.e., $t = 5\,\mathrm{s}$), indicating that the time of peak velocity is not affected by changes in input parameters. Furthermore, the movement speed of material points in the slope section was approximately two to three times that of the material points in the horizontal section

In reality, soil shear strength parameters may decrease under large strains. This may result in differences in the failure mechanisms and postfailure characteristics of shallow slopes. In future studies, the strain-softening behavior (i.e., strain-dependent and shear strengths) of soil should be analyzed to quantify the influence of these parameters on the kinematic behavior of slopes after failure.

Data Availability

The data used to support the findings of this study are available from the corresponding author upon request.

Conflicts of Interest

The authors declare that they have no competing interests.

Acknowledgments

References

[1] M. A. Llano-Serna, M. M. Farias, and D. M. Pedroso, "An assessment of the material point method for modelling large scale run-out processes in landslides," *Landslides*, vol. 13, no. 5, pp. 1057–1066, 2016.

[2] G. Klubertanz, L. Laloui, and L. Vulliet, "Identification of mechanisms for landslide type initiation of debris flows," *Engineering Geology*, vol. 109, no. 1-2, pp. 114–123, 2009.

[3] S. Mohammadi and H. Taiebat, "Finite element simulation of an excavation-triggered landslide using large deformation theory," *Engineering Geology*, vol. 205, pp. 62–72, 2016.

[4] G. B. Crosta, F. V. De Blasio, M. De Caro, G. Volpi, S. Imposimato, and D. Roddeman, "Modes of propagation and deposition of granular flows onto an erodible substrate: experimental, analytical, and numerical study," *Landslides*, vol. 14, no. 1, pp. 47–68, 2017.

[5] S. Cuomo, S. Moretti, and S. Aversa, "Effects of artificial barriers on the propagation of debris avalanches," *Landslides*, vol. 16, no. 6, pp. 1077–1087, 2019.

[6] M. Farin, A. Mangeney, and O. Roche, "Fundamental changes of granular flow dynamics, deposition, and erosion processes at high slope angles: Insights from laboratory experiments," *Journal of Geophysical Research: Earth Surface*, vol. 119, no. 3, pp. 504–532, 2014.

[7] A. Mangeney, O. Roche, O. Hungr, N. Mangold, G. Faccanoni, and A. Lucas, "Erosion and mobility in granular collapse over sloping beds," *Journal of Geophysical Research: Earth*, vol. 115, no. F3, 2010.

[8] I. Manzella and V. Labiouse, "Empirical and analytical analyses of laboratory granular flows to investigate rock avalanche propagation," *Landslides*, vol. 10, no. 1, pp. 23–36, 2013.

[9] R. M. Iverson, "Scaling and design of landslide and debris-flow experiments," *Geomorphology*, vol. 244, pp. 9–20, 2015.

[10] C. W. W. Ng, C. E. Choi, D. Song et al., "Physical modeling of baffles influence on landslide debris mobility," *Landslides*, vol. 12, no. 1, pp. 1–18, 2014.

[11] L. Wang, X. Zhang, and S. Tinti, "Shallow landslides modeling using a particle finite element model with emphasis on landslide evolution," *Earth Surface Dynamics Discussions*, vol. 2019, pp. 1–19, 2019.

[12] X. Zhang, L. Wang, K. Krabbenhoft, and S. Tinti, "A case study and implication: particle finite element modelling of the 2010 Saint-Jude sensitive clay landslide," *Landslides*, vol. 17, pp. 1117–1127, 2019.

[13] J. M. Duncan, "State of the art: limit equilibrium and finite-element analysis of slopes," *Journal of Geotechnical Engineering*, vol. 122, no. 7, pp. 577–596, 1996.

[14] D. M. Potts, G. T. Dounias, and P. R. Vaughan, "Finite-element analysis of progressive failure of Carsington embankment," *Geotechnique*, vol. 40, no. 1, pp. 79–101, 1990.

[15] A. Troncone, E. Conte, and L. Pugliese, "Analysis of the slope response to an increase in pore water pressure using the material point method," *Water*, vol. 11, no. 7, p. 1446, 2019.

[16] W. Chen and T. Qiu, "Numerical simulations for large deformation of granular materials using smoothed particle hydrodynamics method," *International Journal of Geomechanics*, vol. 12, no. 2, pp. 127–135, 2012.

[17] Z. Wieckowski, S. K. Youn, and J. H. Yeon, "A particle-in-cell solution to the silo discharging problem," *International Journal for Numerical Methods in Engineering*, vol. 45, no. 9, pp. 1203–1225, 1999.

[18] A. Troncone, "Numerical analysis of a landslide in soils with strain-softening behaviour," *Geotechnique*, vol. 55, no. 8, pp. 585–596, 2005.

[19] G. R. Liu and M. B. Liu, *Smoothed Particle Hydrodynamics: A Meshfree Particle Method*, World Scientific, Singapore, 2003.

[20] W. Peng, S. Y. Song, C. J. Yu, Y. D. Bao, J. X. Sui, and Y. Hu, "Forecasting landslides via three-dimensional discrete element modeling: Helong landslide case study," *Applied Sciences (Basel)*, vol. 9, no. 23, p. 5242, 2019.

[21] P. A. Cundall and O. D. L. Strack, "A discrete numerical model for granular assemblies," *Géotechnique*, vol. 29, no. 1, pp. 47–65, 1979.

[22] B. T. Shi, Y. Zhang, and W. Zhang, "Analysis of the entire failure process of the rotational slide using the material point method," *International Journal of Geomechanics*, vol. 18, no. 8, article 04018092, 2018.

[23] K. Soga, E. Alonso, A. Yerro, K. Kumar, and S. Bandara, "Trends in large-deformation analysis of landslide mass movements with particular emphasis on the material point method," *Geotechnique*, vol. 66, no. 3, pp. 248–273, 2016.

[24] D. Sulsky, Z. Chen, and H. L. Schreyer, "A particle method for history-dependent materials," *Computer Methods in Applied Mechanics and Engineering*, vol. 118, no. 1-2, pp. 179–196, 1994.

[25] S. Andersen and L. Andersen, "Modelling of landslides with the material-point method," *Computational Geosciences*, vol. 14, no. 1, pp. 137–147, 2010.

[26] S. Bandara, A. Ferrari, and L. Laloui, "Modelling landslides in unsaturated slopes subjected to rainfall infiltration using material point method," *International Journal for Numerical and Analytical Methods in Geomechanics*, vol. 40, no. 9, pp. 1358–1380, 2016.

[27] S. Bandara and K. Soga, "Coupling of soil deformation and pore fluid flow using material point method," *Computers and Geotechnics*, vol. 63, pp. 199–214, 2015.

[28] E. Conte, L. Pugliese, and A. Troncone, "Post-failure stage simulation of a landslide using the material point method," *Engineering Geology*, vol. 253, pp. 149–159, 2019.

[29] A. Yerro, E. E. Alonso, and N. M. Pinyol, "The material point method for unsaturated soils," *Geotechnique*, vol. 65, no. 3, pp. 201–217, 2015.

[30] A. Yerro, E. E. Alonso, and N. M. Pinyol, "Run-out of landslides in brittle soils," *Computers and Geotechnics*, vol. 80, pp. 427–439, 2016.

[31] A. Yerro, K. Soga, and J. D. Bray, "Runout evaluation of Oso landslide with the material point method," *Canadian Geotechnical Journal*, vol. 56, no. 9, pp. 1304–1317, 2019.

[32] Anura3D_v2019, *MPM Research Community*http://www.anura3d.com.

[33] H. Moriwaki, T. Inokuchi, T. Hattanji, K. Sassa, H. Ochiai, and G. Wang, "Failure processes in a full-scale landslide experiment using a rainfall simulator," *Landslides*, vol. 1, no. 4, pp. 277–288, 2004.

[34] I. Jassim, D. Stolle, and P. Vermeer, "Two-phase dynamic analysis by material point method," *International Journal for Numerical and Analytical Methods*, vol. 37, no. 15, pp. 2502–2522, 2013.

[35] F. Zabala and E. E. Alonso, "Progressive failure of Aznalcollar dam using the material point method," *Geotechnique*, vol. 61, no. 9, pp. 795–808, 2011.

[36] E. Fern, A. Rohe, K. Soga, and E. Alonso, *The Material Point Method for Geotechnical Engineering: A Practical Guide*, CRC Press, 1st edition, 2019.

[37] P. Ghasemi, S. Cuomo, A. Di Perna, M. Martinelli, and M. Calvello, "MPM-analysis of landslide propagation observed in flume test," in *Proc. of 2nd International Conference on the*

Material Point Method for Modelling Soil-Water-Structure Interaction, Cambridge, UK, 2019.

[38] K.-H. Yang, T. S. Nguyen, H. Rahardjo, and D.-G. Lin, "Deformation characteristics of unstable shallow slopes triggered by rainfall infiltration," *Bulletin of Engineering Geology and the Environment*, vol. 80, pp. 317–344, 2020.

[39] K. Abe, K. Soga, and S. Bandara, "Material point method for coupled hsfydromechanical problems," *Journal of Geotechnical and Geoenvironmental Engineering*, vol. 140, no. 3, article 104013033, 2014.

[40] D. V. Griffiths, J. S. Huang, and G. F. Dewolfe, "Numerical and analytical observations on long and infinite slopes," *International Journal for Numerical and Analytical Methods*, vol. 35, no. 5, pp. 569–585, 2011.

[41] H. H. Bui, R. Fukagawa, K. Sako, and S. Ohno, "Lagrangian meshfree particles method (SPH) for large deformation and failure flows of geomaterial using elastic-plastic soil constitutive model," *International Journal for Numerical and Analytical Methods in Geomechanics*, vol. 32, no. 12, pp. 1537–1570, 2008.

[42] E. J. Fern and K. Soga, "The role of constitutive models in MPM simulations of granular column collapses," *Acta Geotechnica*, vol. 11, no. 3, pp. 659–678, 2016.

[43] G. Lube, H. E. Huppert, R. S. Sparks, and A. Freundt, "Collapses of two-dimensional granular columns," *Physical review. E, Statistical, nonlinear, and soft matter physics*, vol. 72, no. 4, article 041301, 2005.

[44] Z. R. Mao, G. R. Liu, and X. W. Dong, "A comprehensive study on the parameters setting in smoothed particle hydrodynamics (SPH) method applied to hydrodynamics problems," *Computers and Geotechnics*, vol. 92, pp. 77–95, 2017.

[45] W. T. Solowski and S. W. Sloan, "Evaluation of material point method for use in geotechnics," *International Journal for Numerical and Analytical Methods*, vol. 39, no. 7, pp. 685–701, 2015.

[46] X. Li, Y. Wu, S. He, and L. Su, "Application of the material point method to simulate the post-failure runout processes of the Wangjiayan landslide," *Engineering Geology*, vol. 212, pp. 1–9, 2016.

WILEY | Hindawi

Research Article
Lessons from the Case History of a Massive Landslide Dam

Fawad S. Niazi ID,[1] **Aranzazu Pinan-Llamas** ID,[2] and **Kamran Akhtar** ID[3]

[1]Department of Civil & Mechanical Engineering, Purdue University Fort Wayne, Indiana 46805, USA
[2]School of Polytechnic, Purdue University Fort Wayne, Indiana 46805, USA
[3]National University of Sciences and Technology, Balochistan Campus, Quetta, Pakistan

Correspondence should be addressed to Fawad S. Niazi; niazif@pfw.edu

A massive landslide created a natural dam on two tributaries of Jhelum River near the town of Hattian Bala in Kashmir in October 2005. The landslide was triggered by a 7.6 M_w earthquake. The resulting unconsolidated dam and water impoundment upstream carried hazard potential of downstream damage to both infrastructure and population due to potential flooding caused by its breach. Comprehensive investigations and monitoring were implemented to analyse dam stability. Fresh topographic profiles were generated. Samples of the matrix materials were utilized in the laboratory investigations including grain-size analysis, laboratory electrical resistivity and permeability tests at varying densities and degrees of saturation, and sediment concentration assessment in the seepage discharge. A noninvasive geophysical method was employed together with new topographic information to develop transient subsurface pictures and to assess the advancement of seepage fronts within the dam body. Internal erosion/filtering potential of the matrix material was assessed by comparing grain size distributions with those of the earlier failed dams. Upstream inflows, downstream discharges, daily precipitation, and lake levels monitored during the study period were utilized in hydrological data analysis in an attempt to assess the potential seepage volume. A combination of empirical, analytical, and numerical methods and simulations, together with laboratory and field investigations, led to the interpretations regarding short- and long-term stability of the dam. This paper highlights alternative methods of investigation employed differently from those used by other national and international agencies in analysing the failure potential of this natural dam. It offers lessons learned from a case history that can be beneficial in future evaluation of seepage-induced failure of similar natural features.

1. Introduction

Landslide dams are both common and complicated natural features. They are regarded as transient events on geomorphologic timescale. Their significance lies in the temporal disruption of water channels due to accumulation of debris at the interface between unstable hill slopes and valley floors, resulting in stream impoundments. These impoundments pose vulnerability to the downstream population and infrastructure due to the possibility of catastrophic damage, which can be caused by the dam outburst. Costa and Schuster [1] have shown that most landslide dam failures occur within the first year of their formation and that the outburst floods become more unlikely as they stay longer. However, impact waves triggered by mass movements into the lake and cloud bursts/heavy rains are also known to have caused failure a very long time after the formation of the dam. According to Schuster [2], 55% of 187 investigated examples worldwide failed within one week of their formation, whereas 89% failed within one year.

Failure of landslide dams is known to occur due to overtopping or slope instability or seepage-induced erosion or a combination of these causes. Seepage-induced piping/internal erosion and high confined pore pressures in the body of the landslide dams have been reported as the most probable failure phenomena [3, 4]. Nonetheless, advance prediction of the likely failure mechanism of each dam and assessment of its transient state of stability are constrained by the peculiarities of local geology, topography, geotechnical properties of the dam body, and streamflow/seepage patterns. Owing to their rapid creation, ephemeral nature, and the inhomogeneous properties of the geomaterials within the dam body,
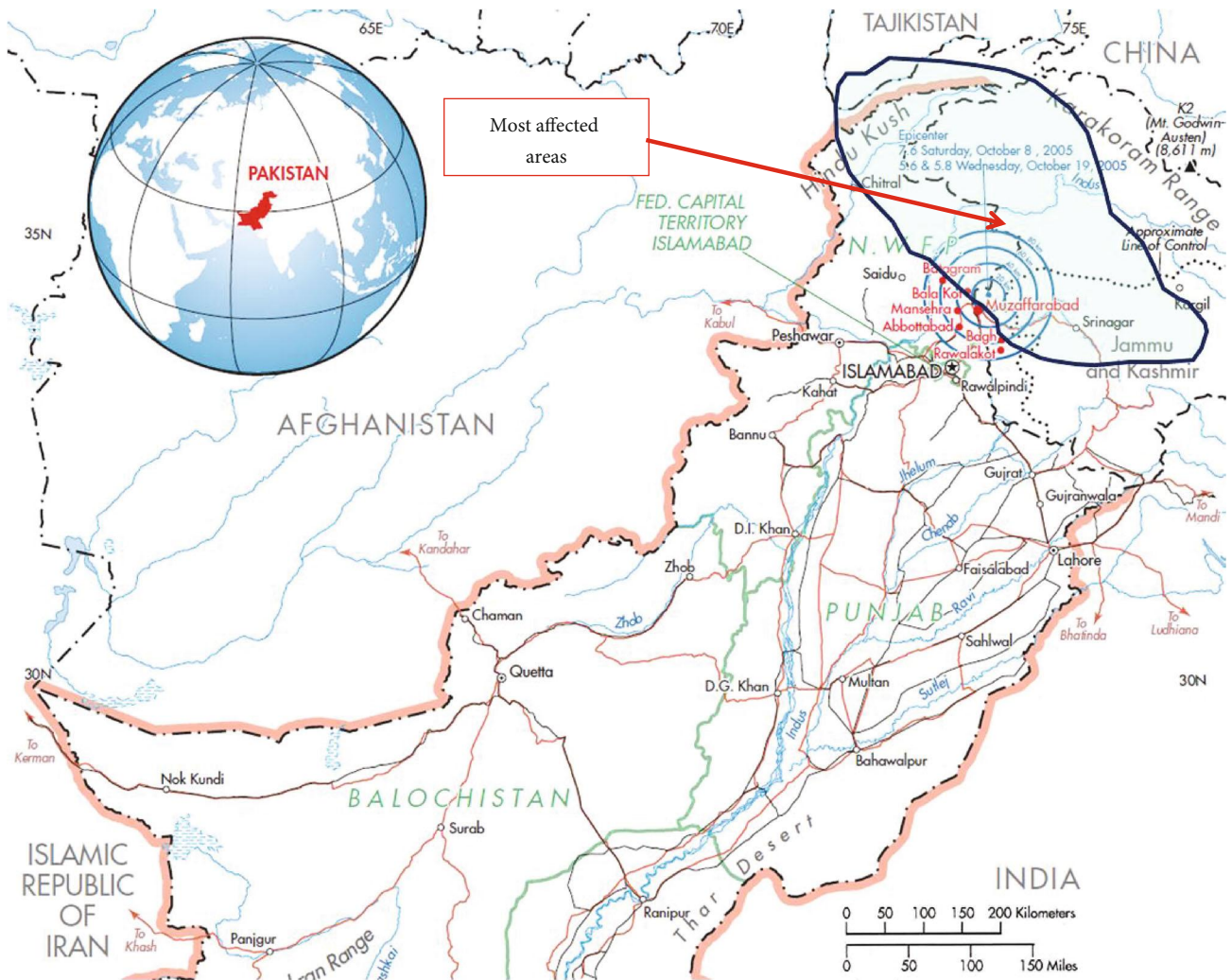
FIGURE 1: Map showing the epicenter of the October 08, 2005, earthquake and the most affected area (adapted from [6]).

a certain degree of lack of understanding of the forms and processes involved still remains. Despite a host of documented case studies, the multivariate geomorphic characteristics inherent in landslide dams continue to pose problems for defining an exact basis of comparison. Yet, it is of high significance to derive, from each case study, a set of key characteristics and indicators. These efforts are likely to assist in continuous improvement of our understanding towards hazard appraisal in future events and for planning of monitoring mechanisms, early warning systems, and mitigation strategies to limit the potential of disasters. This paper has been developed under such motivation.

On October 08, 2005, at 8:50 AM Pakistan Standard Time, a 7.6 M_w earthquake [5] struck in northern Pakistan, Afghanistan, and Kashmir. The earthquake epicenter was located near Muzaffarabad, about 100 km north-northeast of Pakistan's capital city of Islamabad, along a fault associated with the Indian microplate moving northward and indenting at a rate of about 40 mm/yr in the Eurasian plate [6]. Pakistan-administered Kashmir, known as Azad Jammu and Kashmir (AJK), and the eastern districts of Pakistan's

Khyber Pakhtunkhwa Province (previously known as N.W.F.P.) bore the full force of the earthquake (see Figure 1). Since the affected region was predominantly mountainous, it was badly struck by slope failures in the form of small to large landslides.

The most significant single landslide triggered due to this catastrophic event that caught the world's attention was the one located 3.5 km upstream of the confluence of the Jhelum river and Karli water channel near the town of Hattian Bala, AJK [5] (see Figure 2(a)). This landslide originated on Dana Hill (2080 m above sea level (AMSL), 34°09′N/73°43′E) [1] and carried a debris volume of around 85 million m³, which blocked two tributaries of Jhelum River, namely, Karli (a.k.a. Zalzal) and Tung (a.k.a. Salmeah) water channels at their confluence (see Figure 2(b)). This blockage resulted in impoundment of water and creation of lakes on the upstream sides of the debris material (hereinafter referred to as a landslide dam). These lakes turned into a potential hazard for the downstream population and infrastructure, principally in the case of the Karli channel because of its higher inflow rate, significantly large impoundment capacity (i.e., >60 million m³
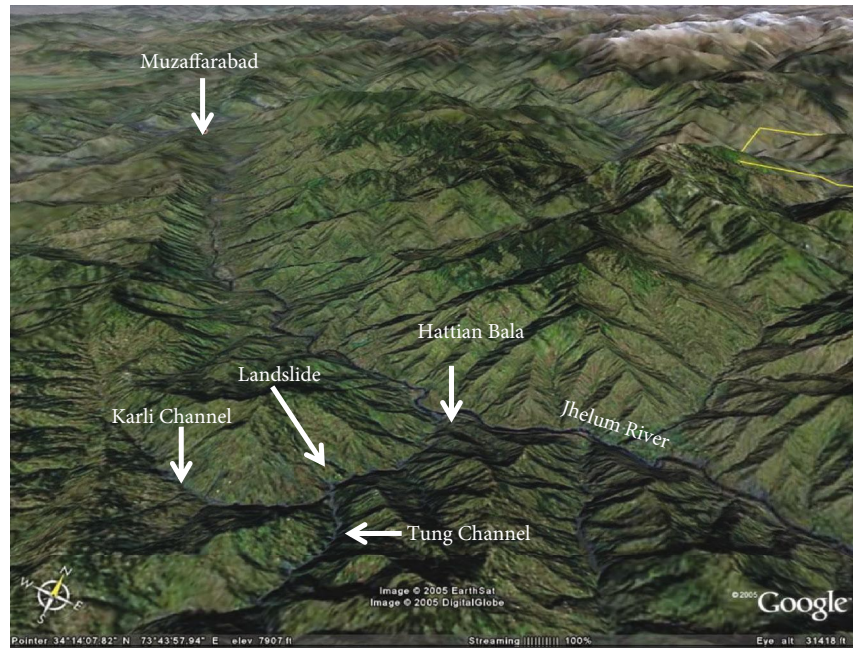
(a)
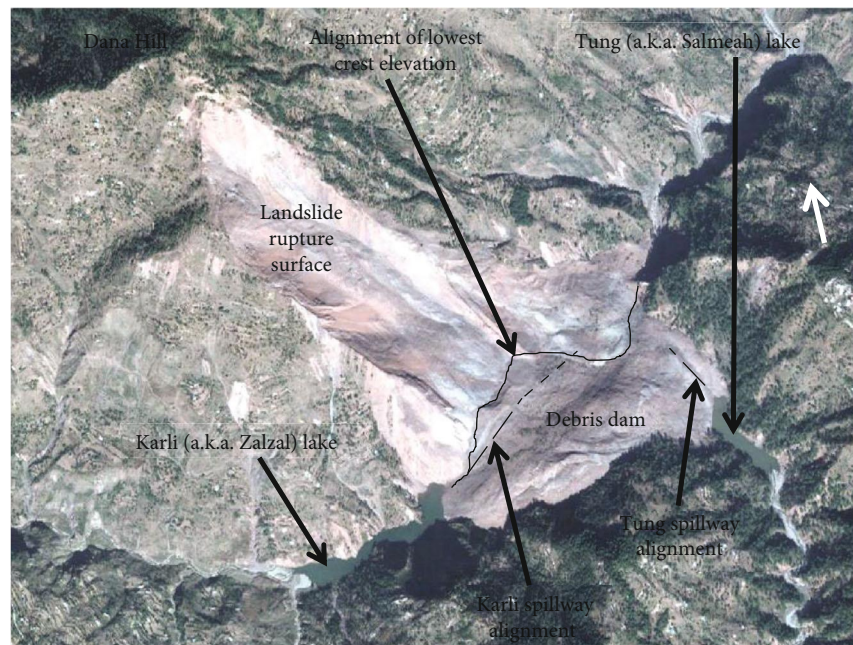
(b)

Figure 2: (a) 3D view of Hattian Bala landslide and surrounding area [7]; (b) satellite imagery of Hattian Bala landslide, dam, and lakes [5].

of water), and the major portion of the landslide dam blocking its flow. Figure 3 shows different pictorial views of the landslide dam area for comprehension of the orientation and scale of the problem. Certain details marked on these pictures (e.g., spillways) are discussed in later parts of this paper.

2. Preliminary Investigations and Initial Recommendations

To analyse the situation, a number of studies were undertaken and monitoring systems were set by various national and international agencies. Of notable mention are those by the Norwegian Geotechnical Institute (NGI), Pakistan Army Engineer-in-Chief's Task Force consisting of Frontier Works Organization (FWO), Geological Survey of Pakistan (GSP), Water and Power Development Authority (WAPDA), Army Survey Group Engineers (ASGE), and National Engineering Services Pakistan (NESPAK) Limited. It is important to note that the fundamental purpose of these studies was the estimation of threat potential and the enforcement of monitoring, and appropriate mitigation measures before the transitory stability of the dam were overcome by the driving forces.
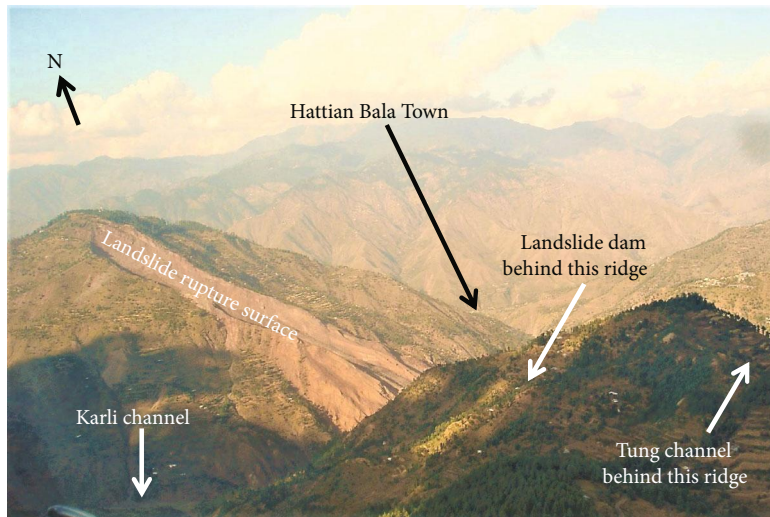
(a)
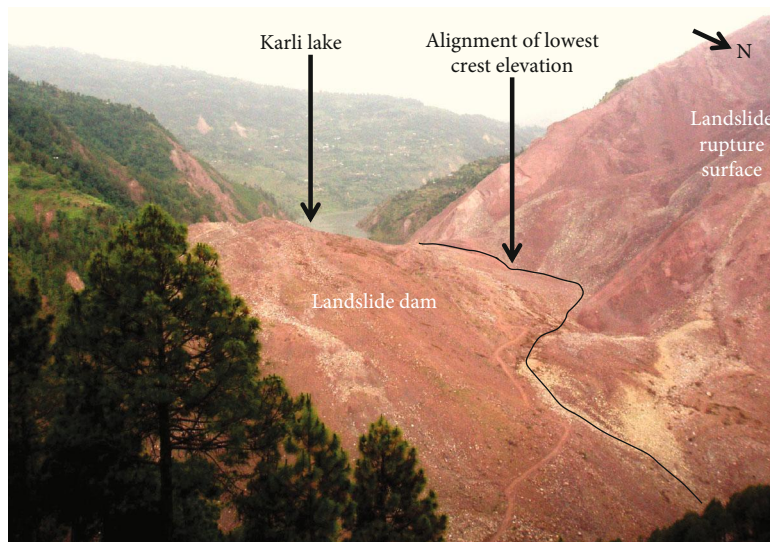
(b)

FIGURE 3: Continued.
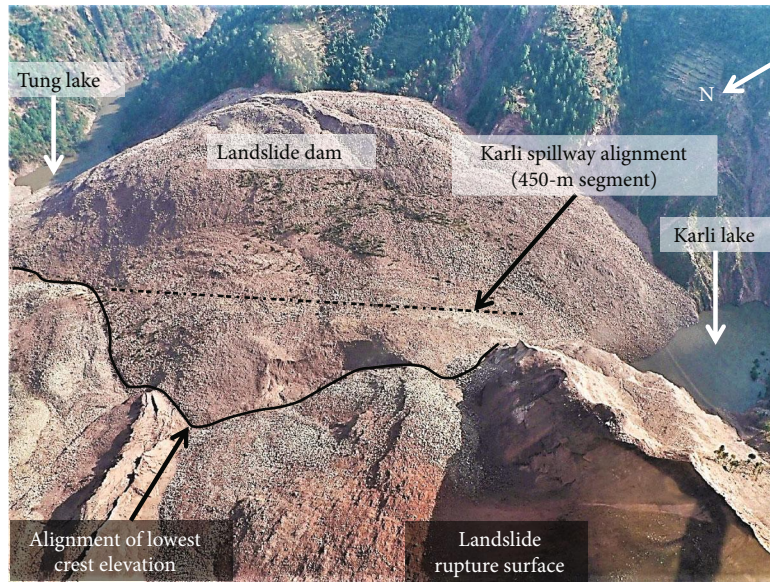
(c)
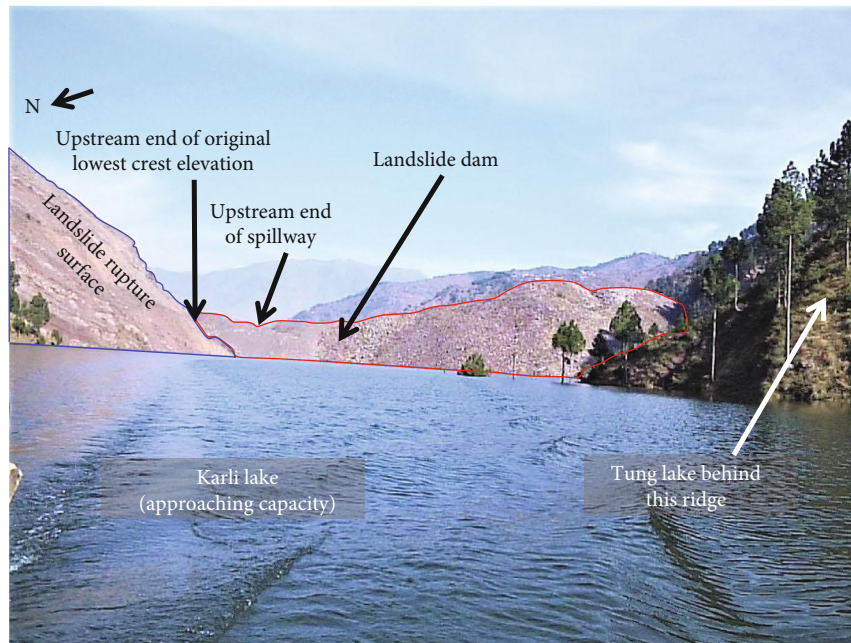
(d)

FIGURE 3: Pictures showing (a) landslide rupture surface and Karli water channel, taken from the upstream side of the dam facing eastward (November 2005); (b) landslide rupture surface, dam, Karli lake, and alignment of the original lowest crest elevation along the dam, taken from the downstream side of the dam facing westward (April 2006); (c) landslide rupture surface, landslide toe, dam, Karli and Tung lakes, and alignments of the original lowest crest elevation and the Karli spillway along the dam surface, taken from the top of the landslide (November 2005); (d) landslide rupture surface, dam, Karli lake, and upstream ends of the original lowest crest elevation and the Karli spillway, taken from Karli lake (December 2006).

2.1. Investigations and Data Collection. The following is a list of data collected and investigations performed by these agencies:

(i) 2D and 3D satellite imageries of the area

(ii) 1 : 50,000 scale topographic map and 1 : 10,000 scale geological map of the area

(iii) Fresh topographic survey and 2 m interval contour map of the landslide dam and the potential lake area

(iv) Hydrological and landslide inventory maps of the area

(v) Seismic refraction tests along five 110 m and one 230 m long survey lines at selected locations on the dam surface

(vi) Laboratory testing on rock and soil samples collected from the dam surface, including water content (w), specific gravity (G_s), uniaxial compression, and index properties

(vii) Hydrological data including lakes' elevation-capacity relationships, average/wet year flows of the two water channels, and average monthly rainfall

(viii) Seepage discharge assessment for increasing lake levels, assuming homogeneous composition of the dam and for a range of permeability (k) values for the dam body and the bed materials

(ix) Slope stability analysis for increasing lake levels, assuming homogeneous dam composition of the dam with a range of cohesion and friction ($c - \phi$) parameters

2.2. Findings. The aggregated salient findings from these studies are summarily presented below [1, 8, 9]:

(i) The Hattian Bala landslide dam was located in a geological zone characterized by the presence of the Early-Middle Miocene Murree and Kamlial Formations (Cenozoic era). These formations include dark red to purple and greenish gray sandstone, purple to reddish brown mudstone (shale), and lenses of conglomerate [1]

(ii) The dam consisted of rock fragments floating in a fine matrix of medium and fine sand with silt and clay-sized particles

(iii) A portion of the dam blocking the Karli channel was composed of cobble-, boulder-, and gravel-sized geomaterials embedded in a dominant matrix of fines, whereas that obstructing the Tung channel was formed mainly by cobble- and boulder-sized debris, with a limited ratio of gravels and finer particles

(iv) The landslide dam body could be divided into two layers with the top layer having smaller proportions of less compacted fine material and the lower layer of comparatively larger proportion of highly compacted fines

(v) The rise in the water level in Karli lake was not commensurate with its recorded total inflow over the study period, indicating significant infiltration into the dam body

(vi) At the average monthly rainfall rate, the dam portion blocking Tung channel would overtop in March 2006, while it could happen earlier with an above-average rate

(vii) The portion of the dam blocking Karli lake would overtop along its lowest crest elevation (adjacent to the toe of the landslide (see Figures 2(b), 3(b), and 3(c))) in March 2011 under average monthly rainfall, and in June 2006 at around the upper limit of 90 percentile rate of rainfall

(viii) The highest point along this lowest crest elevation was 1368 m AMSL, which would become the surface elevation of Karli lake when filled to its maximum capacity

(ix) Failure of the dam could occur due to internal erosion/piping caused by seepage or retrogressive surface erosion due to overtopping flow starting at the downstream toe

(x) With an assumed k of the dam material $\geq 1 \times 10^{-5}$ m/s, and that of the original stream bed as 1×10^{-8} m/s, it would take a minimum of 4 months after the overtopping of Karli lake to develop a steady-state seepage flow through the dam body. Seepage near the downstream toe would develop after that period. This duration would increase if the actual k was lower than these assumptions

(xi) After the filling of Karli lake to its capacity and the development of a steady-state seepage flow, the downstream slope of the dam would become unstable for an assumed effective friction angle (ϕ') of <30° with cohesion intercept of zero for the dam material. It would be stable for ϕ' values $\geq 30°$ under static loading. The upstream slope was estimated to be stable for these assumed values

2.3. Recommendations. The following main recommendations were made to mitigate the hazard potential based on the above findings [1, 8, 9]:

(i) Construction of spillways through the dam in front of both lakes with their sizes and dimensions appropriate to handle extreme discharge events

(ii) Prioritized immediate construction of the Tung spillway to eliminate that part of the overall hazard, followed by the Karli spillway

(iii) Lining the bed and sides of the Karli spillway with boulder- to cobble-sized particles to prevent uncontrolled erosion

(iv) Avoidance of overtopping flow from Karli lake to follow the path along the lowest crest elevation, which could have made the slope along the toe of the landslide rupture surface unstable and result in another catastrophe

(v) Construction of the lined Karli spillway as far eastward of the landslide toe as feasible and dumping of the excavated material along the landslide toe (i.e., into and along the original lowest crest elevation) to enhance its stability

(vi) Implementation of recommended measures prior to the filling of Karli lake to its maximum capacity, preferably before the next monsoon season of year 2006
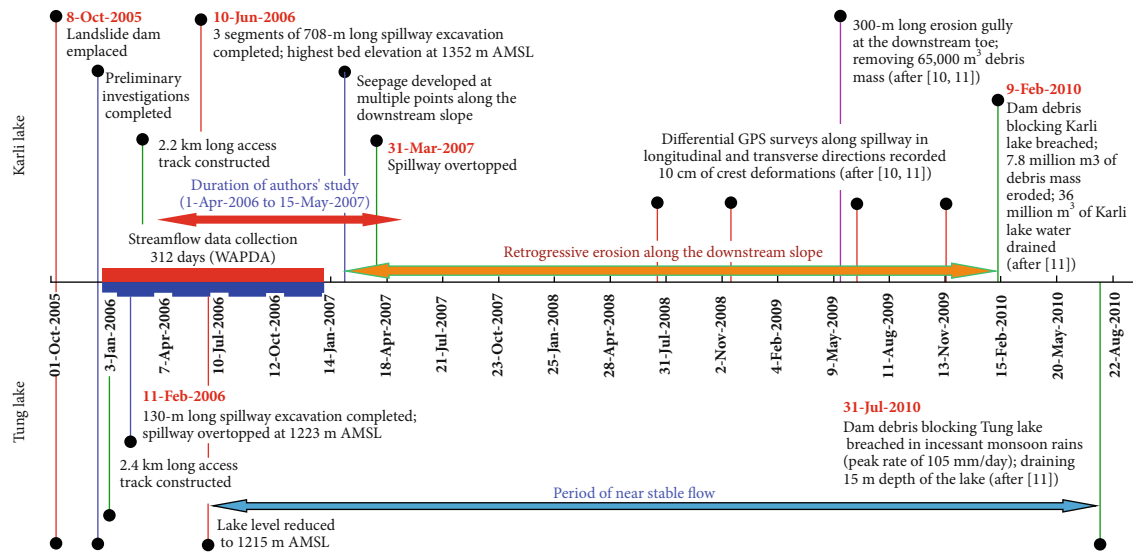
FIGURE 4: Chronology of events that occurred at the Hattian Bala landslide dam site from its creation to its breach (October 8, 2005, to July 31, 2010).

3. Implementation of Mitigation and Monitoring Measures and Chronology of Events

Due to the urgency against the danger of dam breach, recommendations from the investigations and studies summarized above were made to the authorities at the end of December 2005, although formal reports were finalized in a later time frame. The mitigation efforts commenced immediately. A chronology of significant events that took place at the site starting from placement of the landslide dam up to the breach of the dam portion in front of Tung lake in July 2010 is presented in Figure 4. These events include the following:

(i) Fresh topographical surveys of the landslide, landslide dam, and Karli lake areas were completed, and 2 m contour interval maps were prepared by the end of December 2005 (see Figure 5). Figure 5(a) also shows the points of investigation of the authors' study conducted from April 2006 to May 2007 (details are elaborated in later sections of this paper) and the rim of 300 m long erosion gully that developed between December 2008 and June 2009 (as noted in [10, 11]). The thick contour (1368 m AMSL) in Figure 5(b) represents the minimum crest elevation of the landslide dam in its natural state (after Abeer [12]). Karli lake was expected to rise to this elevation without any corrective works

(ii) For transportation of earth moving equipment, a 2.4 km long access track was constructed from the existing road to Tung lake (completed on February 11, 2006) and another 2.2 km long track from Tung to Karli lake (completed on March 1, 2006)

(iii) The WAPDA established a data monitoring system associated with this landslide dam, including daily upstream flows of the two channels, their combined downstream flow, variations in surface elevations of the two lakes, and the daily rainfall. This data was collected for a total of 312 days between December 26, 2005, and December 31, 2006. The approximate locations of the data collection points are shown in Figure 6

(iv) A 130 m long spillway, 11.5 m deep with base width of 4.5 m and elevation of 1235 m AMSL, was excavated through the dam debris in front of Tung lake. The overtopping flow through the spillway began as soon as it was fully excavated on February 11, 2006. The overflow of the lake from Tung spillway and seepage through that part of the dam body caused washing out of the fines through surface erosion and piping over the next about 4 months. Resultantly, lake surface elevation was reduced to 1228 m AMSL by June 20, 2006. Figure 7 shows the cross-sectional dimensions of the Tung spillway at its deepest excavation point and a picture of the overtopping flow through Tung spillway. Although signs of seepage erosion were noticed later, Tung lake experienced a near steady flow across the dam over the next 4 years

(v) A 708 m long spillway, with three distinct segments, was excavated through the dam debris blocking the Karli channel (see Figure 8(a)). The first 477 m long segment was excavated at least 15 m east of toe of the main landslide with a maximum base elevation of 1352 m AMSL and an average base slope of 1 : 11. The cross-section of maximum cut location along this segment is shown in Figure 8(b), and photographs of the same section are shown in Figures 8(c)
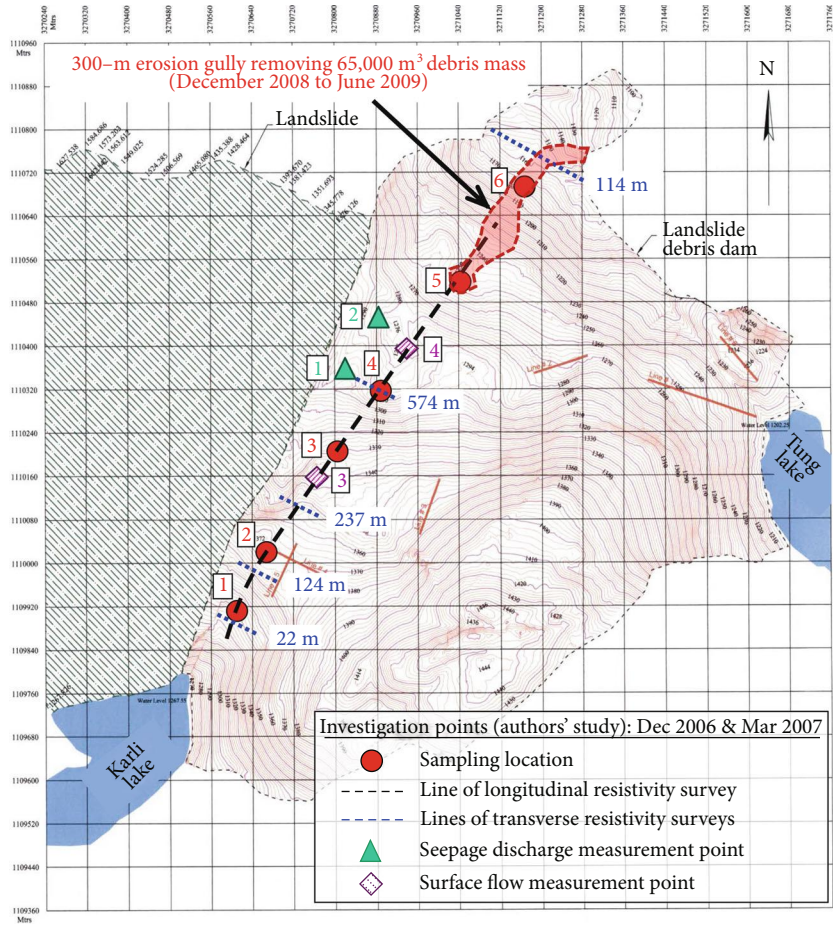
(a)
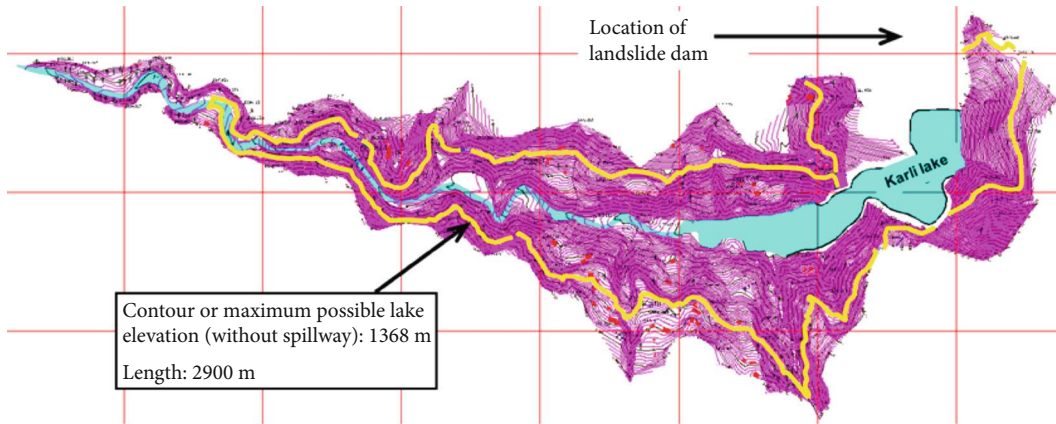
(b)

FIGURE 5: (a) 2 m contour interval topographical map of Hattian Bala landslide dam showing the field investigation points of the authors' study (measurements made in December 2006 and March 2007) and the rim of erosion gully (developed between December 2008 and June 2009); (b) 2 m contour interval topographical map of Karli lake area (adapted from [12]).

and 8(d). In particular, Figure 8(d) shows the spillway bed treatment of this segment by placing boulder- and cobble-sized sandstone rocks from the site. This was done to control rapid surface erosion, especially during a flash flood event. Part of the dam debris excavated from this segment was dumped on the west side in the natural low-

est crest elevation along the toe of the landslide to add to its stability. The middle 71 m long segment had a natural slope of 1 : 2 along the spillway alignment. To ensure that the overtopping flow of water from the first 477 m long segment was directed to the third 160 m long segment, embankments were built on the east and west
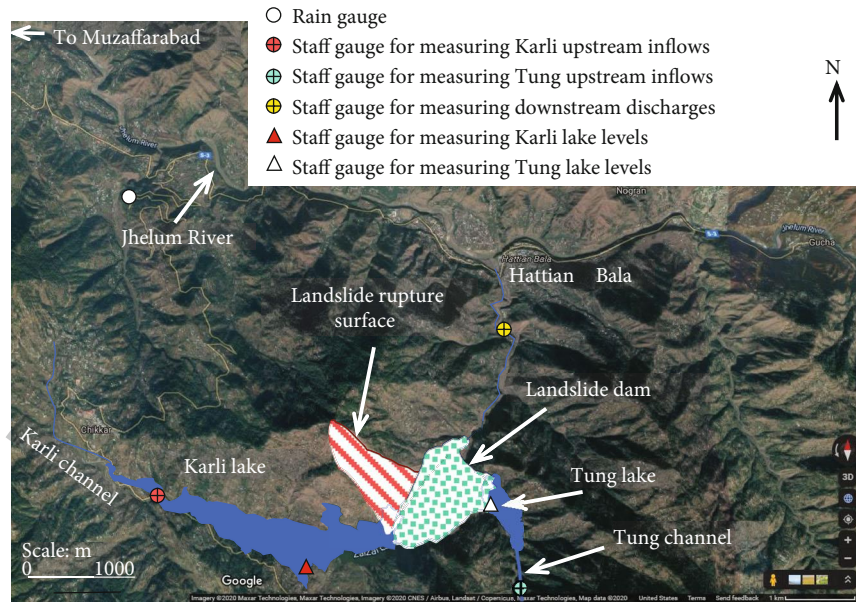
FIGURE 6: Hydrological data monitoring locations marked on the topographical map of the area (data collection period: December 26, 2005, to December 31, 2006) [13].

(a)

(b)
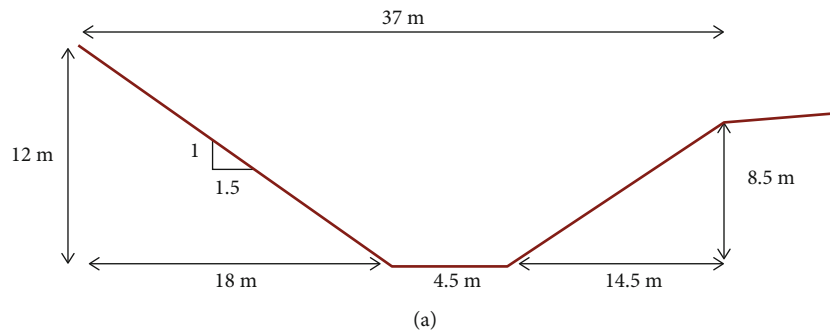
FIGURE 7: (a) Cross-section of the deepest spillway cut along the landslide dam portion blocking Tung lake; (b) photograph of Tung lake overtopping newly excavated spillway (February 12, 2006).

sides of this middle segment from part of the excavated dam debris. The third segment was relatively flat, excavated to the average base elevation of 1277 m AMSL (see Figure 8(e)). A total of about 1.1 million m^3 of debris material was excavated during the construction of this spillway

(vi) While Karli lake continued to fill to its capacity, multiple seepage points along the downstream slope of the dam developed in early February of 2007 (see Figures 5(a) and 9). Karli lake filled to its capacity and started overflowing through the spillway on March 31, 2007 (see Figure 9)

(a)

(b)

(c)

(d)

(e)
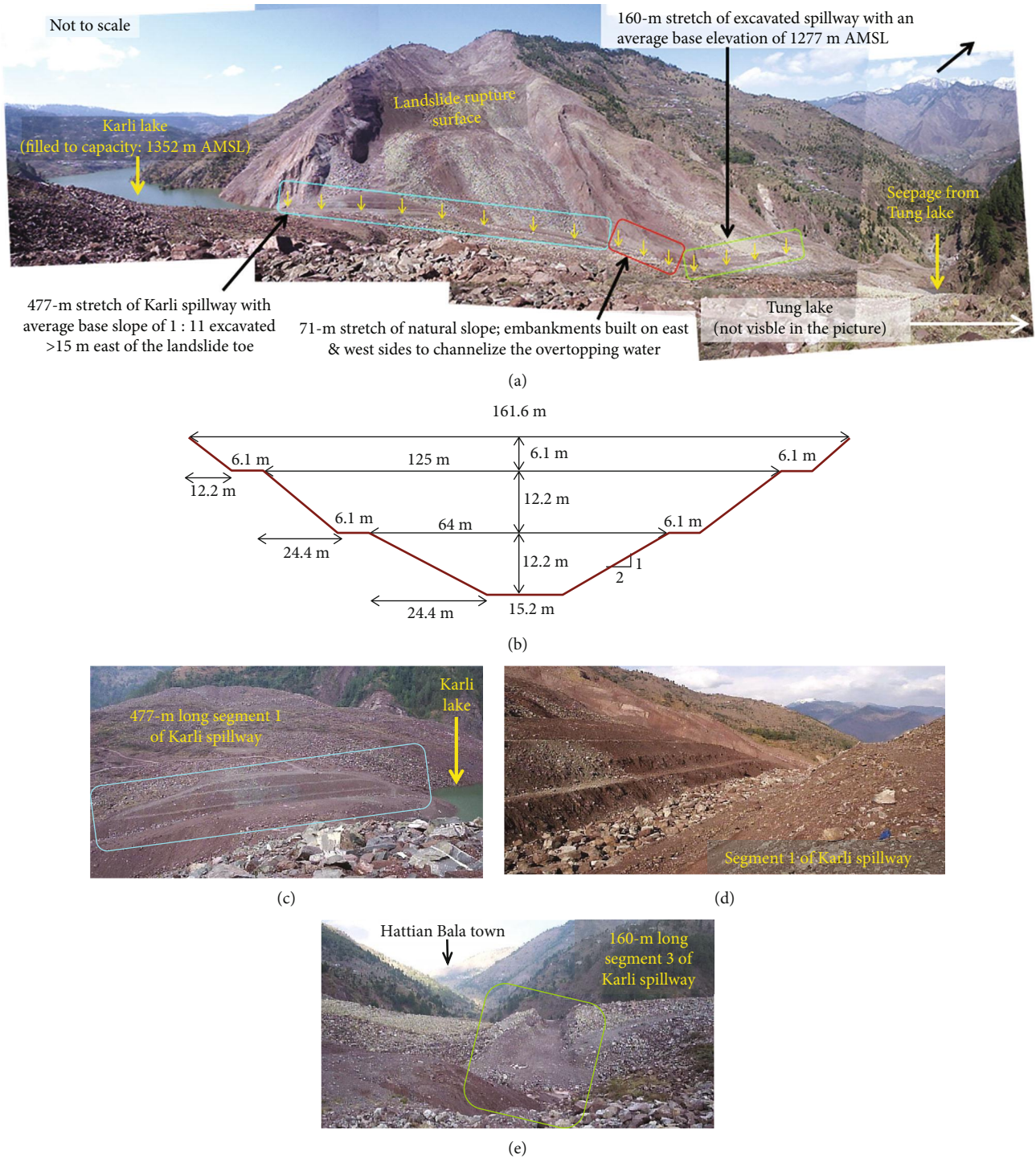
FIGURE 8: (a) Photomosaic showing complete view of the landslide rupture surface (scarp to toe), Karli lake, landslide dam portion blocking Karli channel, Karli spillway, and Tung lake seepage location (31 March 2007); (b) cross-section of segment 1 of the deepest spillway cut along the landslide dam portion blocking Karli lake; (c) photograph showing a complete view of segment 1 of Karli spillway (May 2006); (d) photograph showing bed treatment of Karli spillway segment 1 (May 2006); (e) photograph showing segment 3 of Karli spillway (December 2006).

(a)

(b)

(c)
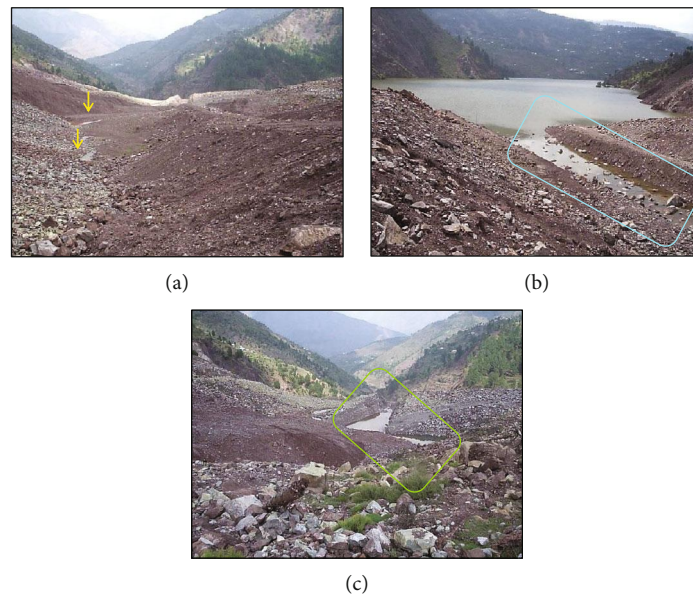
FIGURE 9: Photographs showing (a) locations of seepage points along the downstream slope of the dam (February 2007); (b) Karli lake filled to its capacity overtopping through segment 1 of Karli spillway (April 2007); (c) overtopping water from Karli lake flowing through segment 3 of Karli spillway (April 2007).

(vii) Over a period of the next 3 years, retrogressive erosion was intermittently observed along the downstream slope from the presence of sediments in the downstream flow, although no formal measurements were made until July of 2008

(viii) Quantitative measurements of creep deformation were made along the Karli spillway in longitudinal and traverse directions using Differential Global Positioning System (DGPS) in July and November of 2008 and in June and November of 2009, as reported elsewhere [10, 11, 14, 15]. Deformation in the dam debris mass reported over this period was not significant (the crest subsided by 10 cm while the toe part heaved slightly up) except for a 300 m long erosion gully at the toe of the landslide dam that developed between November 2008 and May 2009, which detached approximately 65,000 m^3 of soil mass (see Figure 5(a) for the location). The slakable nature of the dam material combined with heavy rainfall was found to be the cause of the deformation [14, 15]

(ix) Due to incessant rains in early February of 2010, the water of the Karli lake breached the landslide dam on February 9, 2010, eroding 7.78 million m^3 of debris mass and immediately draining about 36 million m^3 of water from Karli lake (see Figure 10). The flushed debris mass was deposited along the downstream stretch of Karli channel [11]. This breach caused the loss of one life and two dozen houses on the downstream stretch of Karli channel [10]. The lake ultimately reduced to a surface elevation of about 1298 m AMSL over the next decade

(x) The unprecedented floods caused by the monsoon rains in 2010 breached Tung lake as well around the end of July 2010. The lake surface elevation was reduced by 15 m [11], and it has been flowing steadily since then

(xi) An event, not immediately related to the landslide dam itself, but an ultimate consequence of the drawdown of the Karli lake, combined with the disturbance of the pore water pressure equilibrium introduced by unusually heavy rainfall, was reported by Basharat et al. [16]. A translational landslide was triggered on October 24, 2014, upstream of the dam, part of which transformed into earth flow (see Figure 10(c) for the location). This earth flow destroyed 3 houses along the scarp of the landslide and rendered many others to potential risk of future damage

4. Authors' Contributions to Hattian Bala Case Study

The investigations and studies regarding this case study, cited in the foregoing, can be broadly classified into two categories: (1) preliminary investigations to immediately propose measures for minimizing the hazard potential and (2) monitoring projects intended to quantify the evolving scenario at the site. Because of their inherently rapid forming process and ephemeral nature, combined with their complex composition, this general approach of dealing with landslide dams is rather appropriate. Nonetheless, each case has its distinct peculiarities and settings, requiring the use of engineering judgement and consideration of alternative methods of investigation.

The authors' investigations and analyses on the Hattian Bala landslide dam span over a period of 13.5 months (April 1, 2006, to May 15, 2007). Upon review of literature on the topic, reassessment of the above cited investigations, and a

(a)

(b)

(c)
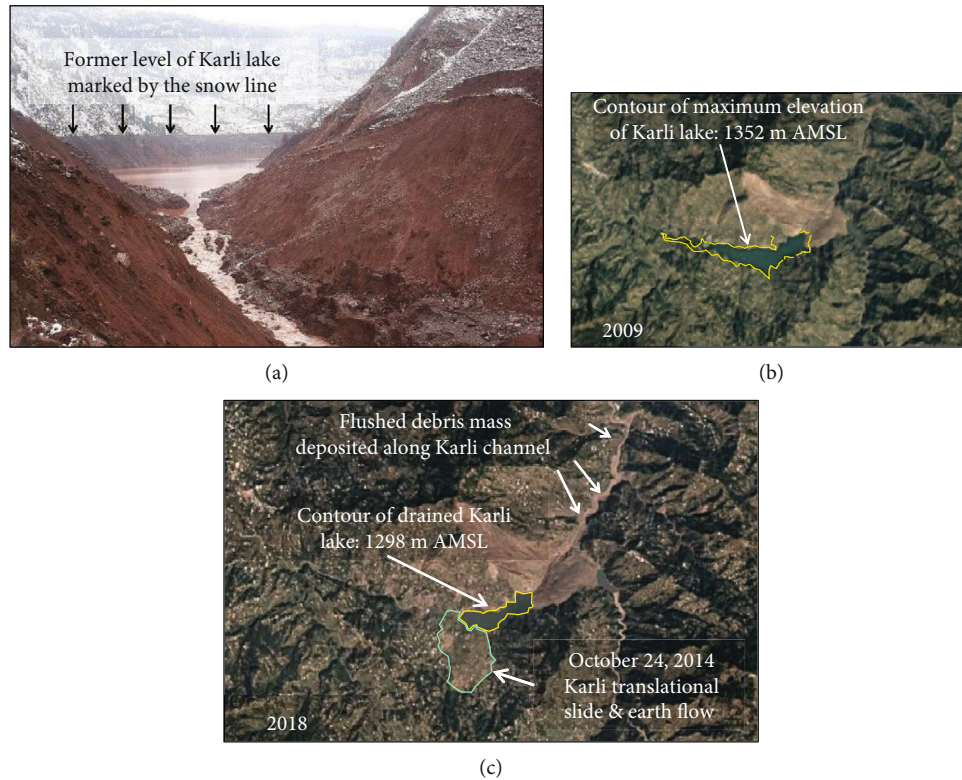
FIGURE 10: (a) Photograph showing the breached landslide dam in front of Karli lake (after [17]; photo courtesy of Dr. Kausar from GSP, dated February 10, 2010); (b, c) Google Earth Timelapse imageries of the Hattian Bala landslide area (year 2009, before landslide dam breaching, and year 2018, most recent available) [16, 18].

week-long site reconnaissance in the first week of April 2006, the following observations were noted:

(i) The recommendations proposed in the preliminary studies were based on geotechnical investigations limited to surface observations and seismic surveys at random locations. The soil and rock sampling for laboratory testing was also done from the dam surface. This did not assist in developing a true subsurface picture of the landslide dam. With the excavation of segment 1 of Karli spillway nearing its completion, the subsurface profile of the most critical part of the landslide dam had now been exposed (average cut depth > 20 m), and more representative samples could be collected for laboratory investigations

(ii) Due to the overall devastated infrastructure and colossal loss of life in the entire region, the immediate priority of the authorities during the early months post this October 8, 2005, earthquake event went to rescue, relief, and rehabilitation activities including opening of communication infrastructure. That, combined with extreme difficulties in transporting field investigation equipment, likely forced the preliminary study teams to make simplifying assumptions regarding important geotechnical parameters (e.g., topographic profiles, k, ϕ', and c). Ranges of assumed parameters were used in the seepage and slope stability analyses to hypothesize

different anticipated scenarios. In reaching their conclusions, more reliance had to be placed on the expertise of geotechnical engineers and geologists with prior experience on similar events

(iii) The model of the landslide dam, prepared for numerical simulations in seepage analysis, did not represent the profile of the dam based on the updated topographic data

(iv) The heterogeneous nature of the landslide dam, coupled with increasing size and volume of water in Karli lake and the evolving processes of consolidation, seepage, and erosion, necessitated in-depth field and laboratory investigations to decide about the monitoring mechanism and prepare an early warning system for the downstream population in case of emergency

(v) Additional data, particularly the streamflows, lake elevations, and daily precipitation, was being compiled in the year 2006. An objective seepage analysis was possible by integrating this new set of information

These observations made it clear that the use of alternative investigation tools was required towards a more rational analysis.

4.1. Materials and Methods. The main focus of the authors' work was the stability study of the landslide dam portion blocking the Karli channel (then turned into a lake), since it was a
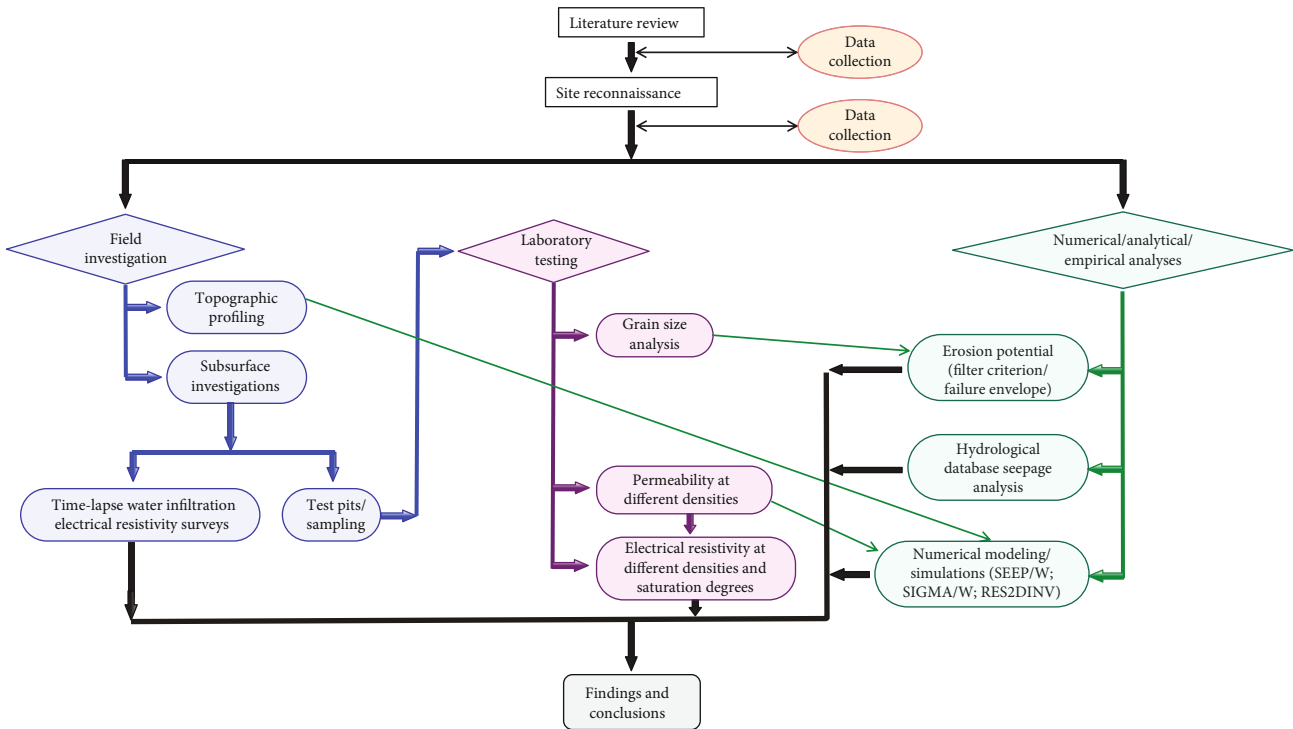
FIGURE 11: Flow chart of the authors' investigations for Hattian Bala landslide dam.

significant evolving hazard. The decision regarding the employment of investigation methods was taken based on their feasibility and reliability, vis-à-vis limitations of accessibility to the site, and the size and scale of the landslide dam. Investigations were aimed at determining the subsurface conditions including the stratigraphy, saturation levels, and seepage conditions affecting the dam stability. A flow chart explaining the investigation methodology adopted in this study is shown in Figure 11. The field investigations were done in two phases, with each phase spanning over a period of about 2 weeks (phase 1 in November/December 2006 and phase 2 in February/March 2007). The following is a summary of the investigations and analyses performed for this study and sets of information relevant to each method and testing approach adopted or analysis performed during this entire process (see Figure 5(a) for locations of field investigation points).

4.1.1. Topographic Surveys.
Using a DGPS, and the pre- and postevent topographic maps, five transverse and one longitudinal surface topographical profiles were obtained along the Karli spillway (see Figures 5(a) and 12). These locations and alignments were selected for the field electrical resistivity surveys planned in the two phases mentioned above and their subsequent numerical simulation and computer modelling.

Since the newly constructed spillway was approximately aligned with that of the preevent trace of the Karli channel, it was logical to predict that when the Karli lake water, entering from the upstream slope of the dam, seeps through its main body, it would concentrate beneath the bed of the spillway. This formed the basis for alignment of the longitudinal survey line.

Locations of the transverse survey lines were selected at critical points along the spillway bed to validate the results of the longitudinal surveys and to support other relevant subsurface investigations. Three of these transverse survey lines were selected over the first half of segment 1 of the spillway, under which the seepage would initiate. The location of the second survey line was selected close to the least elevation point of the 71 m long naturally sloping segment 2, where the seepage water was expected to reappear along the downstream slope. The fifth location was selected near the toe of the landslide dam debris. This location was surveyed in the second phase of the field investigations, when the Karli lake was approaching its maximum capacity, so that any signs of the seepage water reaching that toe of the dam could have been investigated.

4.1.2. Sampling.
For laboratory testing, bulk samples of matrix material were obtained from six locations along the bed of the open cut spillway (see Figure 5(a) for the locations). With such a large scale and quantity of the debris material, selective testing was a compulsion, rather than a choice. It was anticipated that under the static loading conditions, the overall deformations, in the dam body in short to medium term, would result from the seepage/piping and surface erosion, but not from the displacement of heavier and coarser fragments (i.e., boulders and cobbles), and that seepage would concentrate below the Karli spillway. Therefore, the laboratory investigations were focussed on the finer matrix collected from the spillway bed.

4.1.3. Time-Lapse Water Infiltration Electrical Resistivity Surveys.
In general, the material classification of the debris mass of the dam was known from the prior investigations
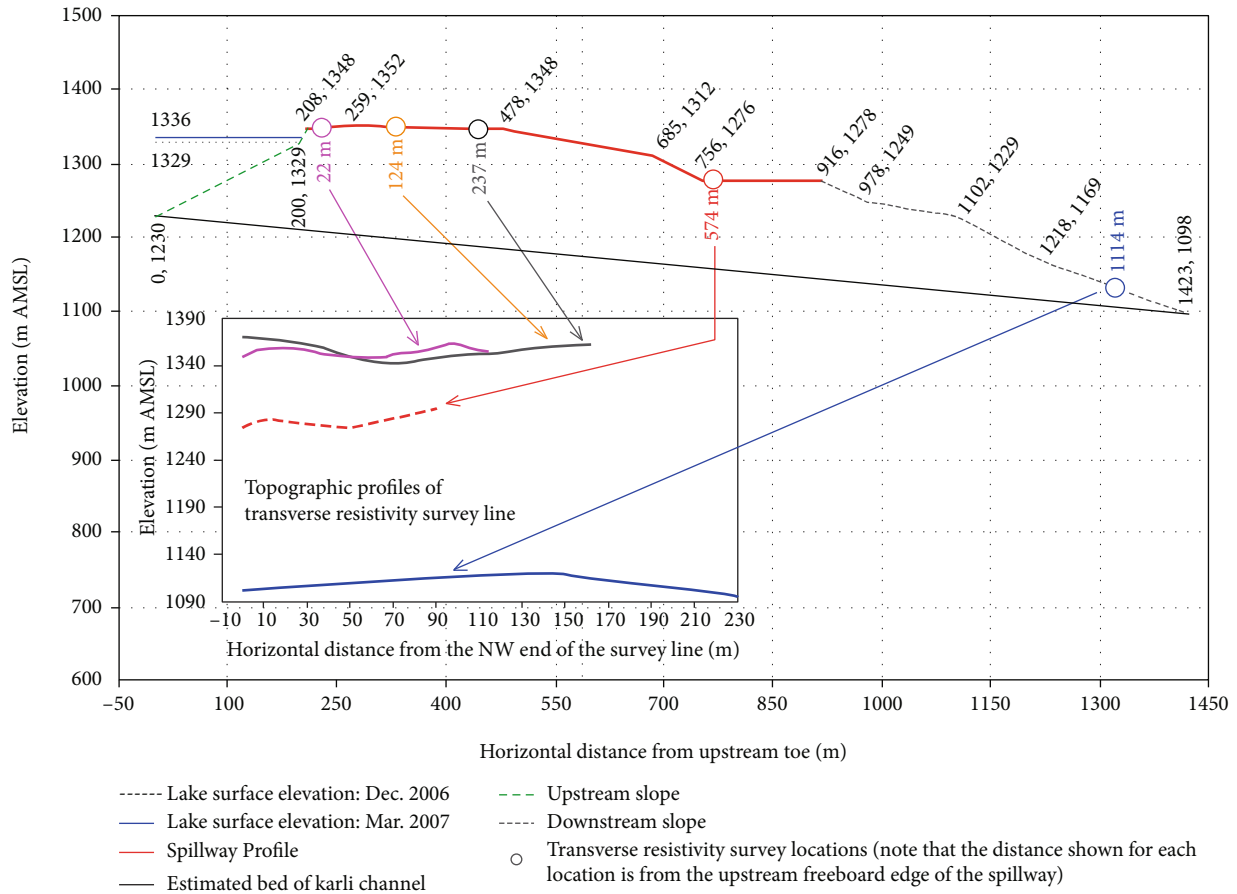
FIGURE 12: Surface topographic profiles of the lines for electrical resistivity surveys; the longitudinal survey line along the Karli spillway and the transverse resistivity locations are shown in the main graph, while the transverse survey lines at 22 m, 124 m, 237 m, 574 m, and 1114 m from the start point of the spillway are shown in the inserted graph.

and geological information gathered from the literature review. Therefore, in evaluating the subsurface conditions, the primary focus was maintained on the permeability assessments and the evolving states of the degree of saturation and material densities. This was accomplished via a series of two-dimensional (2D) electrical resistivity time-lapse water infiltration surveys (with a time-lapse of 3 months) along the survey lines shown in Figures 5(a) and 12. A 2D model is relatively accurate for the subsurface imaging where resistivity changes are common in the vertical and horizontal directions along the survey line.

The surveys include one longitudinal and four in the transverse direction in phase 1 and one repeat of the longitudinal survey besides one transverse survey near the toe end of the dam in phase 2. The second longitudinal survey was conducted as a series of resistivity imaging in time and space to determine the ingress of water from the Karli lake into the dam body.

The surveys were performed by employing the procedure outlined in [19] and by using the Wenner (alpha) electrode array. A 4-electrode resistivity meter system was used. The test parameters are shown in Table 1. Figure 13 shows the electrode locations marked before the field survey and the electrical resistance readings being recorded at the site.

Wenner (alpha) has a simpler arrangement vis-à-vis the length of the longest survey line, the terrain difficulty at the site, and its property of yielding higher signal strength and better ver-

tical resolutions than most of the other arrays [20]. Two outer current and two inner potential electrodes are placed with equal mutual spacing (ES = a) at the start of the survey line, and the resistance of the subsurface is obtained via a resistivity meter. After each reading, the array is advanced along the survey line by a distance "a," and the next reading is recorded. This continues until the electrode array has reached the end of the survey line. The whole procedure is then repeated for the next sequence with the electrodes' mutual spacing ES doubled to "2a" while maintaining the advancing distance between two consecutive readings = 1a. The sequences are continued until the electrode spacing ES = L/3, where L is the length of the survey line.

The raw readings of the resistivity meter are the resistance values used to calculate the "apparent" resistivity values of the subsurface, from which the "true" resistivity is determined via an "inversion" problem. Inversion methods attempt to determine a model for the subsurface whose response agrees with the measured data [20]. The RES2DINV module in the Geotomo software package, with its inbuilt inversion feature, was used for modelling of the field acquired data. In the cell-based method used by the RES2DINV, model parameters are the resistivity values of model cells, while the data are the measured apparent resistivity values. The mathematical link between the model parameters and the response for 2D resistivity models is provided by finite element methods [20].

TABLE 1: Test parameters of the field electrical resistivity surveys at the Hattian Bala landslide dam.

Survey location	Length of survey line (m)	No. of sequences	No. of data points	Maximum investigation depth (m)	Initial electrode spacing (m)	Electrode array
Phase 1 (November/December 2006)						
Longitudinal	894	59	3675	155		
Transverse at 22 m	114	6	57	20		
Transverse at 124 m	150	8	100	26	6	Wenner alpha
Transverse at 237 m	162	9	117	28		
Transverse at 574 m	90	5	35	16		
Phase 2 (February/March 2007)						
Longitudinal	894	59	3675	155	6	Wenner alpha
Transverse at 1114 m	234	26	1001	41	3	

(a)

(b)

FIGURE 13: Field electrical resistivity survey in progress along the longitudinal survey line of the Karli spillway. The pictures illustrate (a) the marking of the electrode locations and (b) the resistivity system.

TABLE 2: RES2DINV modelling parameters for the Hattian Bala landslide dam.

Category	Method used	Remarks
Inversion	Combined inversion method	Marquardt (or ridge regression) and Occam (or smoothness-constrained)
Model discretization	Extended model method	Model extended to survey lines' edges
Topographic modelling	Distorted finite element grid	Uniform distortion

A summary of the methods used in the RES2DINV program to build the subsurface pseudosections is given in Table 2. To determine true resistivity values, a "combined inversion" method was selected, which is used in situations where data sensitivity values of model cells are distorted by large resistivity variations [20]. By combining "Marquardt" and "Occam" inversion methods, distortions found due to large resistivity variations in the model were reduced. To account for the topographic variations along the survey lines, the coordinates, shown in Figure 12, were included as part of the input data. A "distorted finite element grid with uniform distortion" was selected for the topographic modelling. This enabled matching the surface nodes of the mesh to the actual topography. With this option, nodes below the surface (and the model layers) shifted by the same extent as the surface nodes.

4.1.4. Laboratory Investigations. The samples of matrix material were used in the following laboratory tests:

(i) Classification Tests. Including the grain size analysis and the Atterberg limit determination following the ASTM Standards [21–23] for textural classification based on the Unified Soil Classification System (USCS) [24]

(ii) Erosion Potential Assessment. Additional grain size analyses towards employing an empirical approach for the assessment of erosion potential (detailed methodology is explained in a separate subsection below)

(iii) Permeability Tests. Performed over a range of selected dry densities following the ASTM Standard [25] (the k values from these tests were used in the seepage analysis, explained later) (see Figures 14(a) and 14(b) for the testing arrangement)

(iv) Laboratory Electrical Resistivity Tests. Performed as per the ASTM Standard [26]. The adopted testing methodology is detailed below.

The electrical resistivity values determined from the field tests are characteristic not only of the type of the subsurface geomaterial but also of its dry density (ρ_d) and the degree of saturation (S) [20]. The saturation levels within different zones below the field survey lines (which are also an indication of the seepage trends) could, therefore, be estimated if a correlation could be established between the field and laboratory determined resistivity values at different densities and degrees of saturation. Accordingly, a series of laboratory resistivity tests were performed on the samples of matrix material over a range of the same seven different densities used in the permeability tests and for five distinct degrees of saturation at each ρ_d (i.e., S = 20%, 40%, 60%, 80%, and 100%). A laboratory resistivity box (6.2 cm × 3.91 cm × 22.9 cm) was used to house the calculated quantities of the sample and water to achieve each ρ_d and S. Each sample was compacted in layers in a static compaction machine (see Figure 14(c)). The predetermined quantity of water was evenly added for the desired degree of saturation, and the resistivity box was placed in the vacuum chamber for about 30 minutes to allow uniform distribution of water within the sample. The resistance was measured with a resistivity meter after connecting it to the box with the current and potential electrodes embedded in the prepared sample (see Figure 14(d)). The resistivity (ρ) values were then calculated using the following expression:

$$\rho = R\,\frac{A}{a}, \tag{1}$$

where R is measured resistance, A is the cross-sectional area of the sample perpendicular to the current flow (6.2 cm × 3.91 cm), and a is the inner electrode spacing [26]. Since these are apparent resistivity values, the calibrations for the field densities and degrees of saturation in different zones of the subsurface were also performed using the apparent resistivity values from the field

4.1.5. Empirical Approach for the Assessment of Erosion Potential. A common approach to assess the vulnerability of a dam to internal erosion is to apply the filter criteria in the transition areas from fine to coarser material [27]. This method of analysis was not appropriate for a naturally deposited heterogeneous landslide dam without developing a subsurface picture and accurately locating the zones of such transitions within the dam body. Based on the suggestions by Meyer et al. [28], the empirical approach of comparing the grain size distribution curves of the matrix materials from the six sampling locations on the landslide dam with Sherard's failure envelope [29] was adopted. This envelope was drawn from the analysis of numerous embankment dams that exhibited failure due to internal erosion; the curves of the soils falling within this envelope provide inadequate internal filtering capability. The envelope and the comparison are shown in Results and Interpretations.

The filter performance of the landslide dam, as suggested by D_{15}/D_{85} Kézdi [30], was also investigated. To explain this application, a filter criterion, commonly expressed as D_{15}/D_{85}, is often used in the soil drainage problems, including the selection of materials for erosion-free drainage through the embankment dams and the retaining walls, etc. Here, D_{15} is the particle size corresponding to 15% finer of the grain size distribution curve of the coarse material (also termed as the filter), whereas, D_{85} is the size corresponding to 85% finer of the grain size distribution curve of the retained or protected finer soil (also termed as the base). For the embankment dams to be stable against internal erosion, the $D_{15,\text{filter}}/D_{85,\text{protected soil}}$ ratio of its material should be less than 4 to 5.

In applying this criterion to the matrix samples from the landslide dam, the grain size distribution curve of the whole material of each sample was separated at 6 different particle sizes (0.15 mm, 0.43 mm, 0.85 mm, 2.00 mm, 4.75 mm, and 9.53 mm). Thus, a total of 36 separations were made for the 6 samples. For each separation, the complete coarser fraction was treated as the filter material and the entire remaining finer fraction was considered as the base or protected material. Separate grain-size distribution curves were drawn for the filter and base fractions. Then, D_{15} of the grain size distribution curves of the filter and D_{85} of the grain size distribution curves of base fraction were determined. Figure 15 illustrates the method of determining the D_{15}/D_{85} ratio for one of the 6 samples from the Hattian Bala landslide dam at a separation size of 0.15 mm between coarse and fine fractions. As shown, the grain size distribution curves of the coarse fraction (red-dashed) and the fine fraction (blue-dotted) are plotted separately besides that of the whole sample (black-solid), and their respective D_{15} and D_{85} are determined.

In addition to the individual D_{15}/D_{85} ratios at 6 separation points, the means of those 6 were also calculated for each sample as well as for each separation point. The values were compared against the filtering capability criteria mentioned above.

4.1.6. Hydrological Database Analysis. The WAPDA and the Metrology Observatory at Garhi Dupatta collected hydrological data during a total period of 371 days (from December 26, 2005, to December 31, 2006) via the monitoring system shown in Figure 6. The actual data from each gauge was collected for the number of days shown below (these data are plotted in Figures 16(a) and 16(b)):

(i) Daily Karli channel inflow: 312 days

(ii) Daily Karli lake surface elevation: 312 days

(iii) Daily Tung channel inflow: 312 days

(iv) Daily Tung lake surface elevation: 286 days

(v) Daily downstream discharge: 286 days

(vi) Daily precipitation records: 371 days (actual rainfall: 73 days)

In addition to the above data, with the new contour maps now available at 2 m intervals, the plan areas of the lake surfaces corresponding to each contour and the matching volumes of water in the two lakes were also calculated and utilized for this study (see Figure 16(c)). The key data of catchment areas for both the channels is given in Table 3.
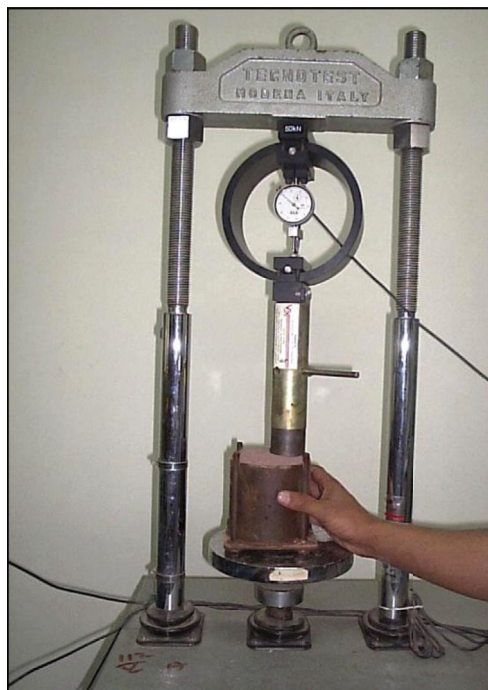
(a)
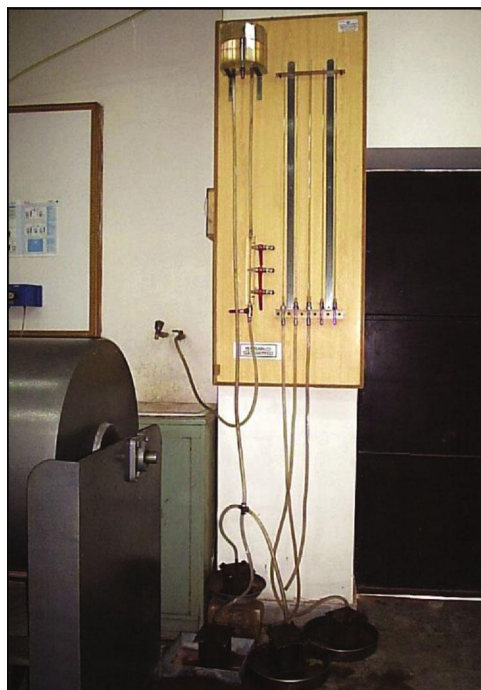
(b)
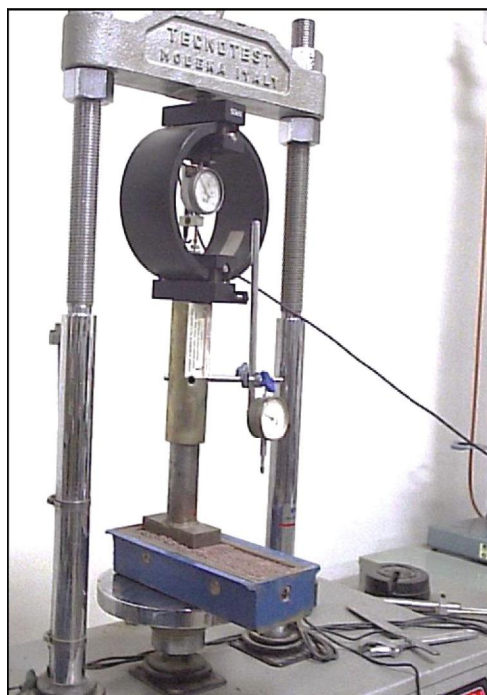
(c)
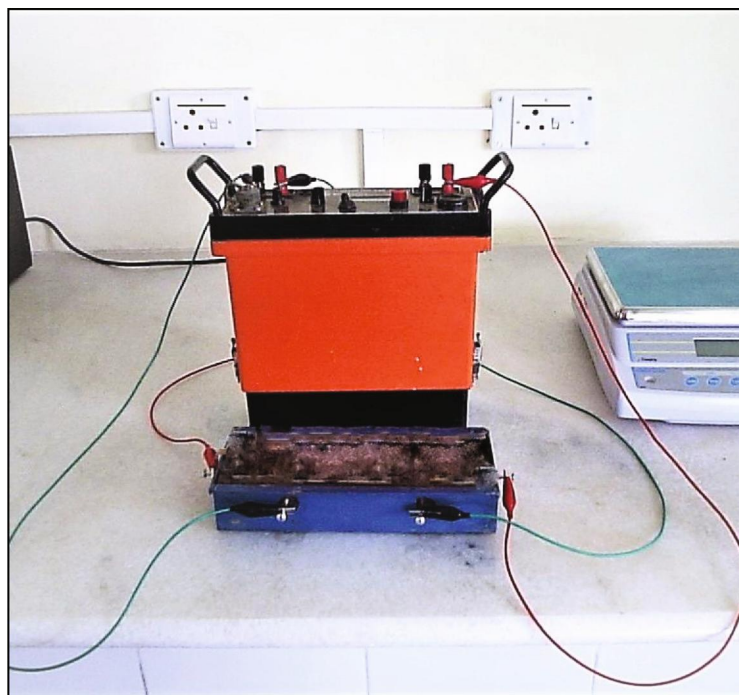
(d)

FIGURE 14: Selected laboratory tests on matrix material: (a) sample being compacted to the desired density in compaction-mold permeameter; (b) permeability test in progress on multiple samples; (c) sample being compacted to the desired density in the resistivity box; (d) resistivity box and sample connected to the resistivity meter with current and potential electrodes embedded in the sample.
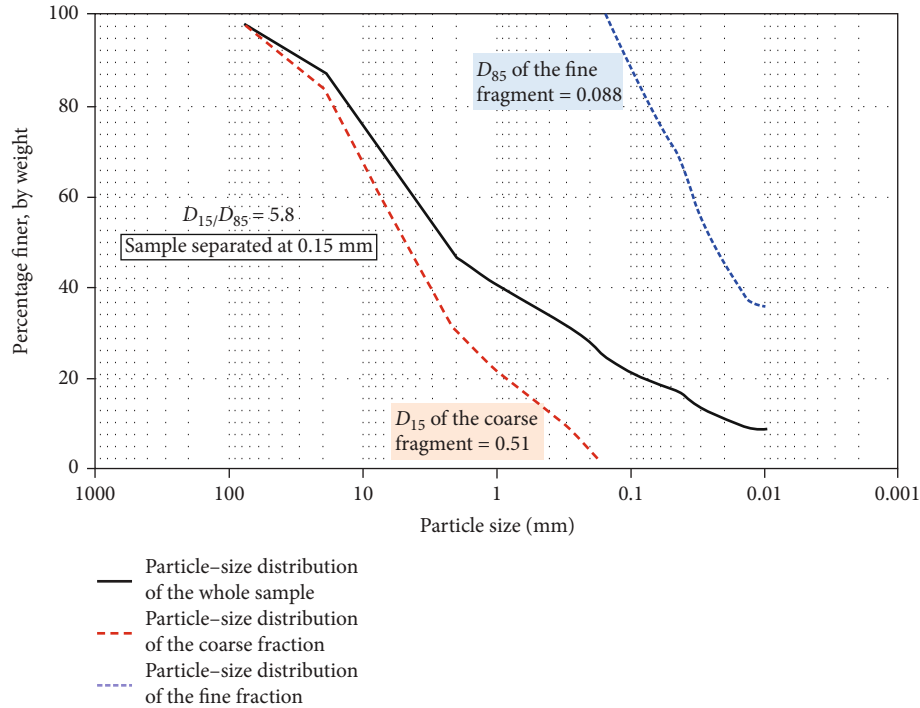
FIGURE 15: Illustration that shows the determination of D_{15}/D_{85} of matrix sample material from the Hattian Bala landslide dam from its grain size distribution separated at 0.15 mm particle size.

Regardless of the extensive data mentioned above, the following significant, yet practical, limitations had to be dealt with in an effort to estimate the quantities of seepage into the landslide dam:

(i) The downstream discharge measurements were recorded at a location significantly distant from the toe of the landslide dam along the downstream stretch (see Figure 6). This implied possible contributions to the discharge from springs and nonperennial channels between the toe of the dam and the downstream measurement location, especially during the rainy days

(ii) Of the number of the catchment areas' springs listed in Table 3, the discharge data of those located between the upstream inflow measurement points of the two lakes and their respective interface with the upstream toe of the dam were not available

(iii) Runoff during the precipitation between the upstream measurement points and the upstream slope of the dam went ungauged into the lakes

(iv) The closest contour interval on the topographical maps of the catchment areas was scaled at 2 m, whereas the daily fluctuations in the water levels in the Tung lake and the rise in that of the Karli lake were happening at the scale of millimeters. Therefore, the volume change measurements could not be compared with the inflow on daily basis with much accuracy

(v) The nearest meteorological observatory at Garhi Dupatta was located nearly 30 km northwest of the site. Since the site was at a higher elevation, the daily temperature data recorded at that observatory were not very useful in calculations of the evaporation losses from the lakes

The following analyses were performed from the data graphically presented in Figure 16:

(i) Comparisons of the periodic lakes' levels with their respective inflows

(ii) Upstream inflows versus combined downstream discharges with effort to account for the precipitation

(iii) The influence of precipitation on the inflows and downstream discharge

(iv) Development of polynomial expressions representing the relationship between the plan areas (y) and their corresponding surface elevations (x) of the two lakes:

$$\text{Karli lake } \left(\text{with } R^2 = 0.998\right): y = 46.05 \, x^2 - 1.115 \\ \times 10^5 x + 6.744 \times 10^7,$$

$$\text{Tung lake } \left(\text{with } R^2 = 0.941\right): y = 24.11 \, x^2 - 5.317 \\ \times 10^4 x + 2.906 \times 10^7$$

$$(2)$$
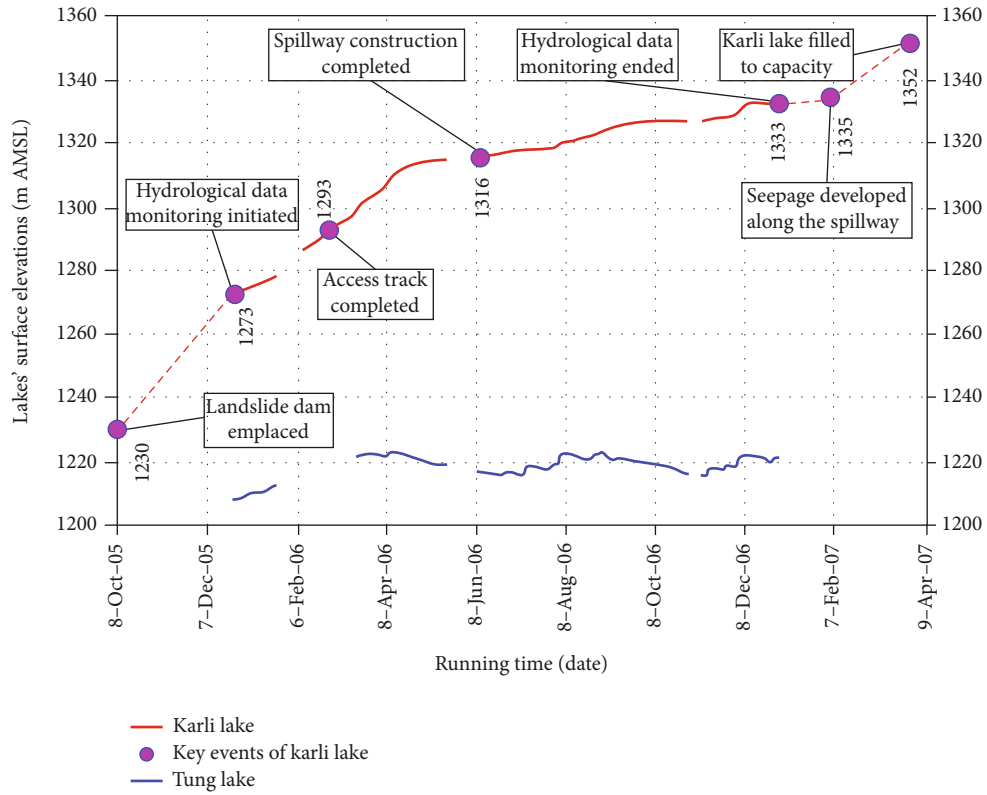
(a)
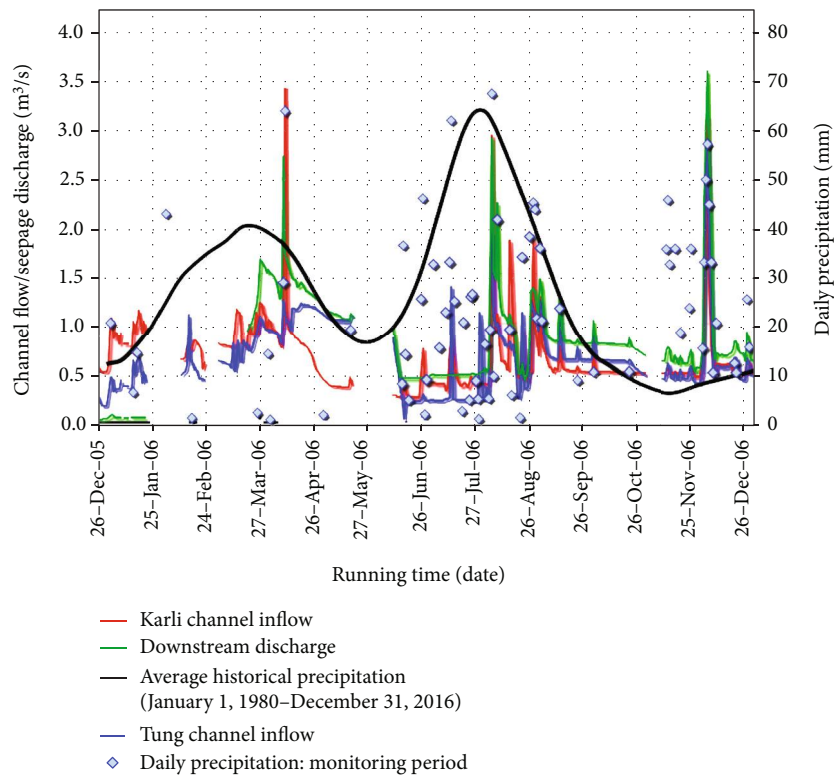
(b)

Figure 16: Continued.

(c)
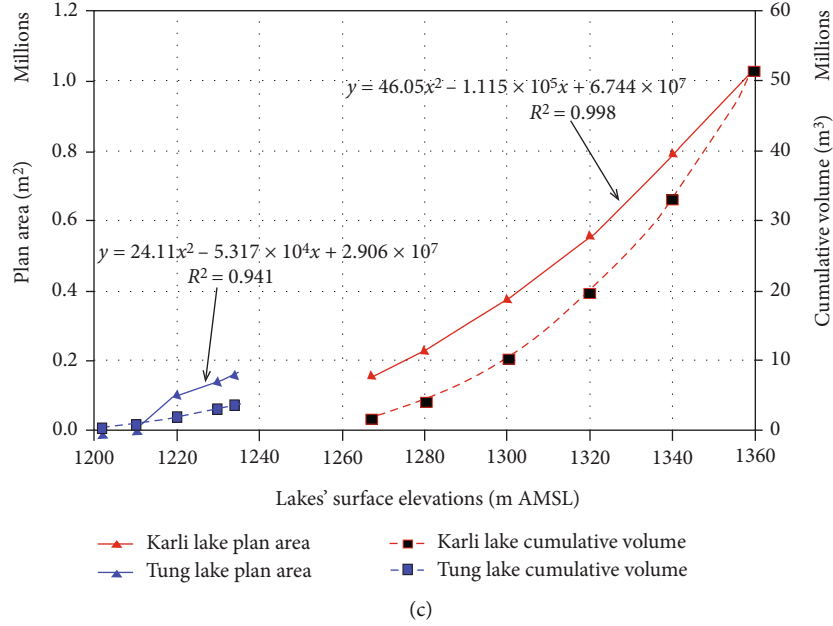
Figure 16: (a) Filling curves and lake periodic surface elevations for Karli and Tung lakes (significant events related to Karli lake are also shown): October 08, 2005, to March 31, 2007; (b) hydrological data including inflows of the two lakes and the downstream discharge from Hattian Bala landslide dam, daily precipitation in Hattian Bala area, and the average historical precipitation from NOAA [31]: December 26, 2005, to December 31, 2006; (c) plan area and corresponding cumulative volume vs. lake surface elevation for Karli and Tung lakes calculated from the contour maps.

Table 3: Key data of catchment areas of Karli and Tung channels (after Hoeg et al. [8] and NESPAK and GSP [9]).

Channel	Area (km^2)	Length (km)	No. of springs
Karli	45	13	232
Tang	30	8	102

(v) Comparisons of the daily increase in water volume of the Karli lake and fluctuation in the Tung lake based on the above expressions taking into account their daily inflows

(vi) Estimation of the seepage volume from the methodology is detailed below.

The seepage volume can be estimated if $Q_{vol.dis.} > Q_{vol.cont.}$, where $Q_{vol.dis.}$ is the upstream inflow volume and $Q_{vol.cont.}$ is the volume between contours (i.e., the actual lake volume). To calculate the seepage volume in other cases, where $Q_{vol.cont.} > Q_{vol.dis.}$ or $Q_{vol.cont.} = Q_{vol.dis.}$, the ungauged flow must be determined. The general expression for the seepage discharge may be written as

$$Q_{out} = Q_{in} + Q_{i?} - \frac{\Delta h \, A_{ave.}}{\Delta t}, \qquad (3)$$

where Q_{out} is potential seepage discharge, Q_{in} is the upstream inflow, $Q_{i?}$ is the ungauged flow (e.g., rainfall on the surface area of lake + runoff from catchments), $\Delta h \, A_{ave.}/\Delta t$ is change

in the storage, $\Delta h/\Delta t$ is the periodic change in the height of water in the lake, and $A_{ave.}$ is the average plan area with respect to $\Delta h/\Delta t$. Since the measuring interval was 24 hours, converting equation (3) from the rate of volume to volume basis yields

$$Q_{out} \, \Delta t = (Q_{in} + Q_{i?}) \, \Delta t - \Delta h \, A_{ave.}. \qquad (4)$$

The above expression is suited for the analysis during the rainy period, which was discarded due to the larger number of unknown variables during those days (especially, due to the increase in the ungauged flow). Only dry period data (collected during days with positive potential seepage volume) were considered for the analysis. Data collected during a total of 92 dry days (April, May, September, and October of 2006) were analysed. For the dry period, equation (4) reduces to

$$Q_{out} \, \Delta t = Q_{in} \, \Delta t - \Delta h \, A_{ave.}. \qquad (5)$$

When $Q_{out} \, \Delta t$ is zero, $Q_{in} \, \Delta t = \Delta h \, A_{ave.}$ (i.e., inflow entirely goes into storage plus evaporation; hence, there is no water for seepage). When $Q_{out} \, \Delta t > 0$, it can be inferred that water is available for seepage. If $Q_{out} \, \Delta t < 0$, it implies anomalous results, which can perhaps be attributed to the contribution of springs in the catchment area, which continues even during dry weather.

A set of calculations were performed for (1) the sums of upstream inflows and downstream discharges for both lakes, (2) seepage volumes of both channels (expressed as the percentage of the upstream and downstream flows), and (3) seepage volume within the pore spaces of the dam body.

4.1.7. Seepage Discharge and Surface Flow Measurements from Karli Lake. The seepage water appeared at multiple new locations along segment 2 of the Karli spillway (see Figures 5(a) and 9(a)) starting on February 5, 2007, when the lake surface elevation was at 1335 m AMSL. Unusual rainfall in the month of March 2007 also accelerated the process of lake filling, as evident from the slope steepness at the end of the filling curve shown in Figure 16(a). Karli lake overtopped the spillway on March 31, 2007. Measurements of water at the new seepage points and from the overtopping flow could reveal information, possibly aiding in the assessment of surface erosion/piping through the dam body. Accordingly, discharge/flow rate measurements and water sampling were done at both of the newly developed seepage locations and later at two other points along the spillway: one near the end of segment 1 and a second one at the lowest elevation point along segment 2. The seepage locations, flow/discharge rates, and the suspended sediment concentration measurements from the water samples were analysed against the Karli inflow and RES2DINV resistivity model. The sediment concentrations were measured using Test Method A of the ASTM Standard [32].

4.1.8. Numerical Simulations for Seepage Analysis. The finite element-based SEEP/W module of GEOSLOPE software was used for seepage analyses of the Hattian Bala landslide dam. These analyses were performed under static loading conditions, including simulations for two distinct downstream boundary conditions (i.e., zero flux, and downstream head commensurate with the original channel bed, i.e., at 1\100 m AMSL), and for the following pondage levels of the Karli lake:

(i) 1329 m AMSL, recorded during phase 1 of the field investigations

(ii) 1336 m AMSL, recorded during phase 2 of the field investigations

(iii) 1352 m AMSL, commensurate with maximum lake capacity and the highest bed elevation of the Karli spillway

The finite element model of the subsurface developed in SEEP/W was replicated from the pseudosection obtained from the RES2DINV resistivity program. The model consisted of 22,690 elements and 23,074 nodes. Different zones within this model were assigned k values based on the calibrations performed during the laboratory investigations between k, ρ, and ρ_d values and comparing those with the RES2DINV pseudosection. Simulations were run for likely combinations of the boundary conditions. Effort was made to conceptualize various threshold combinations of conditions and parameters, which could generate instability in the dam. The SEEP/W model prepared for these simulations along with the permeability values assigned to various zones is shown in Figure 17. It can be noticed that the zone at the toe of the landslide dam (orange) was assigned a very low permeability value. This zone consisted mainly of boulder- and cobble-sized particles in which longitudinal electrical resistivity surveys could not be extended in both phases of the investigations. The 234 m long transverse resistivity survey conducted with great difficulty at the 1114 m location in the phase 2 investigations indicated very high subsurface resistivity. The low permeability values were, thus, assigned to match with the calibration model mentioned above.

4.2. Results and Interpretations. The following collective interpretations were derived from the results and findings of the combination of the investigative methodologies employed by the authors to study the stability of this landslide dam.

4.2.1. Index Tests. The dam was a heterogeneous body of landslide debris mass comprising of materials ranging from boulders to clay-size particles. Figure 18 presents the formal grain size analysis and the USCS classification of the six samples of matrix material collected from the Karli spillway. On average, about 60% of the matrix material consisted of particles finer than the #4 sieve (4.75 mm), 50% finer than the #10 sieve (2.00 mm), 38% finer than the #40 sieve (0.425 mm), and 28% contribution of fines (clay and silt-sized particles). Examples of the variety of the coarser fragments of the debris material from different parts of the dam are also shown in Figure 19.

4.2.2. Erosion Potential. Results from the comparison of the grain size distribution curves with that of the Sherard failure envelope [29] (see Figure 18) indicated that the dam material was significantly susceptible to internal erosion due to the seepage forces. However, since the material in the subsurface was a random assemblage of coarse and fine fragments of the crushed source rock, piping could not develop or advance in its classical sense. Instead, it was expected to be a slow process, extended over months and possibly years.

The results from the "no erosion filter criterion" analyses: D_{15}/D_{85} ratio [33] are summarized in Table 4. Out of a total of 36, twelve results (4 samples separated at 5 different particle sizes) satisfied the criterion. All the other ratios did not fit in the criterion. The overall mean value of 20.26 was considerably beyond the acceptable range, implying that the material forming the dam body was nonresistant to internal erosion. Nevertheless, this criterion would best work in embankments where the transition zones from fine to coarse material are somewhat definable. Therefore, clear erosion patterns through this dam with inhomogeneous configuration, composition, and grain size could not be assessed with much precision.

Based on the data, it was expected that erosion would develop due to overtopping flow and retrogressively advance from the toe to the upstream until the crest of the dam would start to erode. Piping was also anticipated to develop and advance at a relatively slower but constant pace at multiple locations along the dam body. This was also validated from the results of the suspended sediment concentration measured on the water samples from the two seepage points mentioned in the previous section (those results are discussed in a later subsection).

Permeability values assigned to zone

🟦 6.3×10^{-7} m/s		🟨 3.95×10^{-9} m/s	
🟦 1.5×10^{-7} m/s		⬜ 1.0×10^{-9} m/s	
🟩 8.4×10^{-8} m/s		🟧 9.7×10^{-10} m/s	
🟩 9.8×10^{-9} m/s			
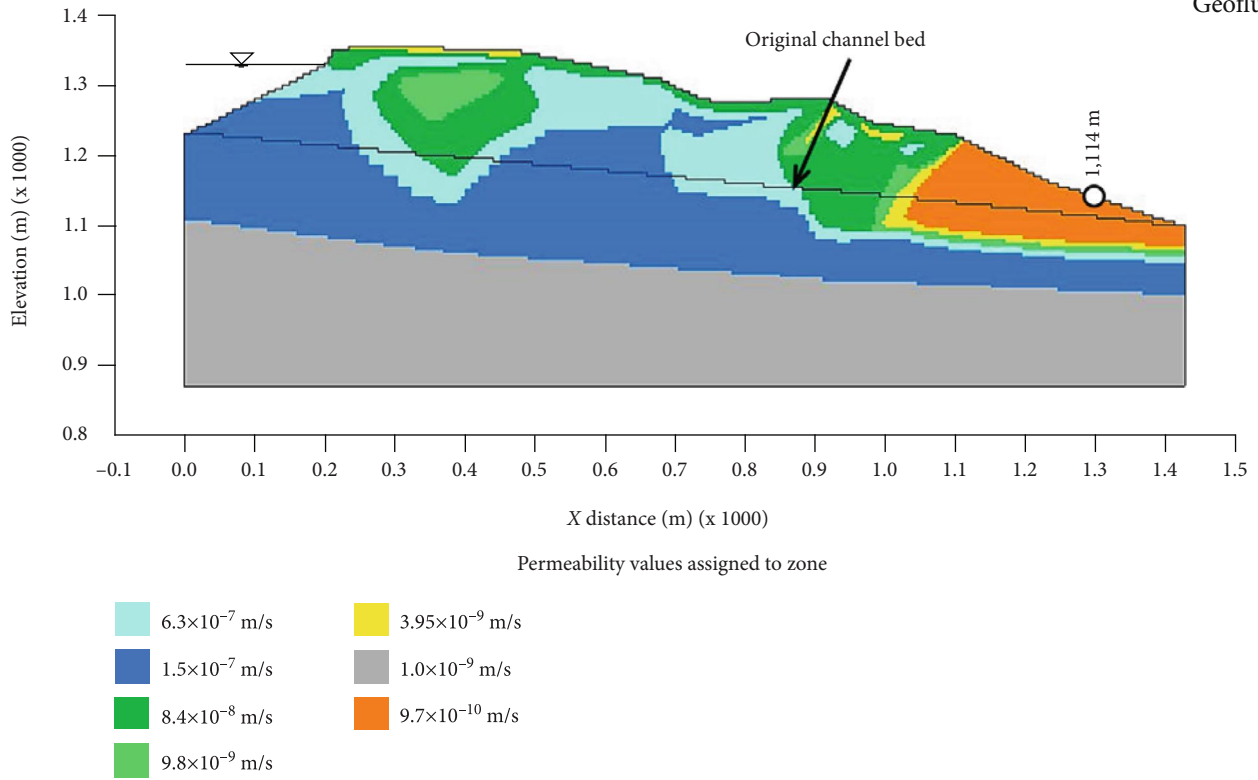
FIGURE 17: Finite element model used in SEEP/W for seepage analyses of the landslide dam section along the longitudinal survey line.

Sample no	Particle size distribution (%)			LL (%)	PL (%)	PI (%)	USCS
	Gravel	Sand	Silt/clay				
1	37.7	42.5	19.8	19.8	16.0	3.8	SM (d)
2	26.8	49.5	23.7	24.7	16.3	8.3	SC
3	47.3	30.3	22.4	17.6	13.4	4.2	GM–GC
4	48.3	31.9	19.8	18.8	16.1	2.7	GM (d)
5	42.6	11.8	45.6	19.5	12.6	6.9	GM–GC
6	37.4	25.4	37.2	20.2	13.4	6.8	GM–GC
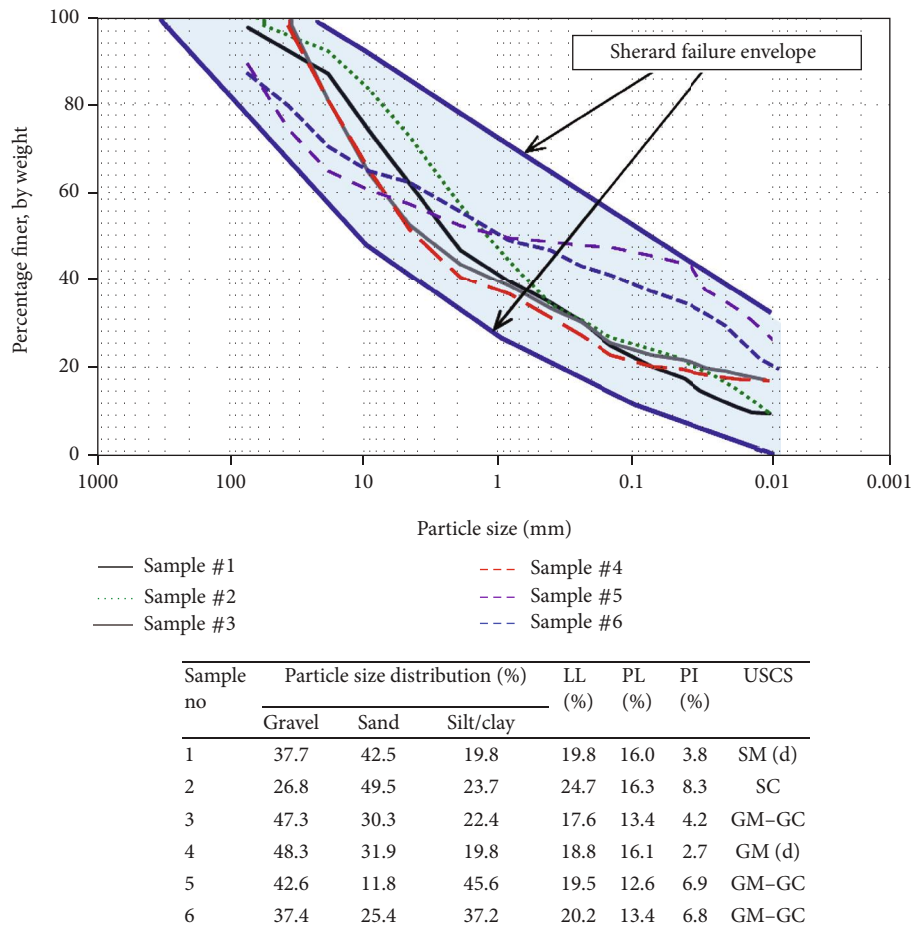
FIGURE 18: Grain size distribution curves, Atterberg limits, and the USCS classification of matrix samples from Karli spillway.

(a)

(b)

(c)
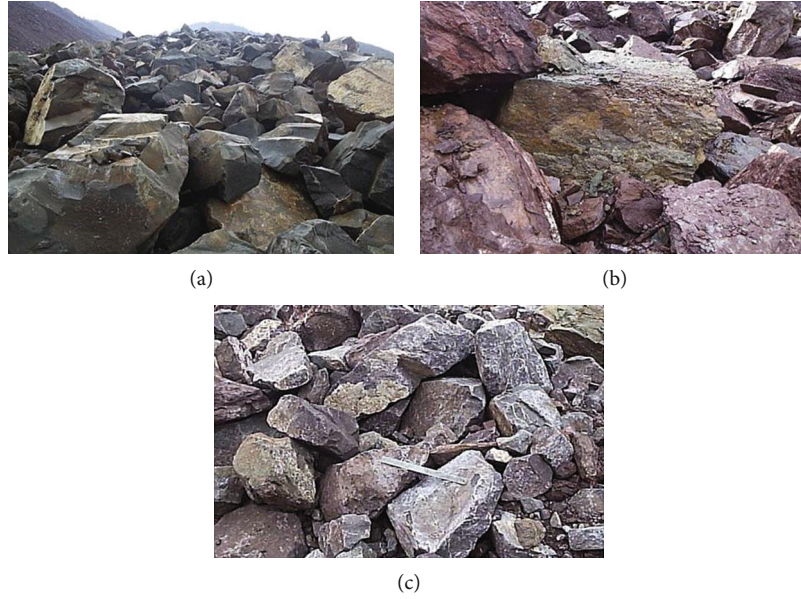
FIGURE 19: Examples of coarse materials from Hattian Bala landslide dam: (a) grey sandstone; (b) purple to reddish-brown mudstone (shale); (c) sandstone (used as a scale is a 12″ stainless steel ruler).

TABLE 4: D_{15}/D_{85} ratios for samples of the matrix material from the Hattian Bala landslide dam separated at selected particle sizes.

| Sample no. | Particle size of separation (mm) | | | | | | Mean D_{15}/D_{85} |
	0.15	0.43	0.85	2.00	4.75	9.53	
1	5.80	6.11	5.68	3.69	2.51	2.01	4.30
2	10.21	4.02	2.71	2.58	2.53	2.42	4.08
3	9.12	9.48	7.73	6.07	3.38	1.89	6.28
4	14.69	9.47	7.29	6.29	2.77	1.69	7.03
5	103.19	114.31	127.66	135.21	26.88	14.41	86.94
6	21.10	15.53	13.10	9.02	9.81	9.16	12.95
Mean D_{15}/D_{85}	27.35	26.48	27.36	27.14	7.98	5.26	20.26

4.2.3. Laboratory Calibration for Resistivity, Saturation, Permeability, and Density. The combined results of resistivity (ρ) vs. dry density (ρ_d) and degree of saturation (S) and permeability (k) vs. ρ_d from a series of laboratory tests are shown in Figure 20. The overall k of the dam was low, decreasing by about two orders of magnitude from 6.3×10^{-7} to 4.0×10^{-9} m/s over the range of ρ_d that represented a natural state of the material within the dam body (i.e., 1520 to 2090 kg/m^3). The corresponding ρ values calculated from the laboratory measurements were influenced by both ρ_d and S. The overall range of ρ was found to be 37.9 to 218.3 ohm-m, decreasing for ρ_d as well as S. The decrease in ρ with the increase in ρ_d was more pronounced for the samples tested in a drier state compared to those with higher degrees of saturation. The ρ values of the samples tested at different ρ_d converged to an average value of 39.9 ohm-m for $S = 100\%$.

The matrix material used in this testing was a mix of naturally crushed rock from their sources of limestone and mudstone (shale). The resistivity values obtained from this test series were, therefore, also compared with the typical range of resistivity values for sandstone: 10 ohm-m (wet) to 2500 ohm-m (dry) and shale: 25 ohm-m (wet) to 1500 ohm-m (dry) [20]. These results and analyses offered a fair assessment of the expected ranges of resistivity, permeability, degree of saturation, and density at the site, interpretation of the RES2DINV pseudosections of the surface from field resistivity data, and selection of permeability values for different zones in the SEEP/W analysis.

4.2.4. Subsurface Pseudosection from Field Electrical Resistivity Surveys. The subsurface 2D pseudosections resulting from the field electrical resistivity survey data of the two phases and their inverse modelling in RES2DINV are shown in Figure 21. It may be noted that the resistivity values shown are the true values obtained from "inversion" of the resistivity values calculated directly from the measured resistance data in the field. Due to the overlapping range of typical resistivity values of shale and sandstone in their wet to dry states, it was
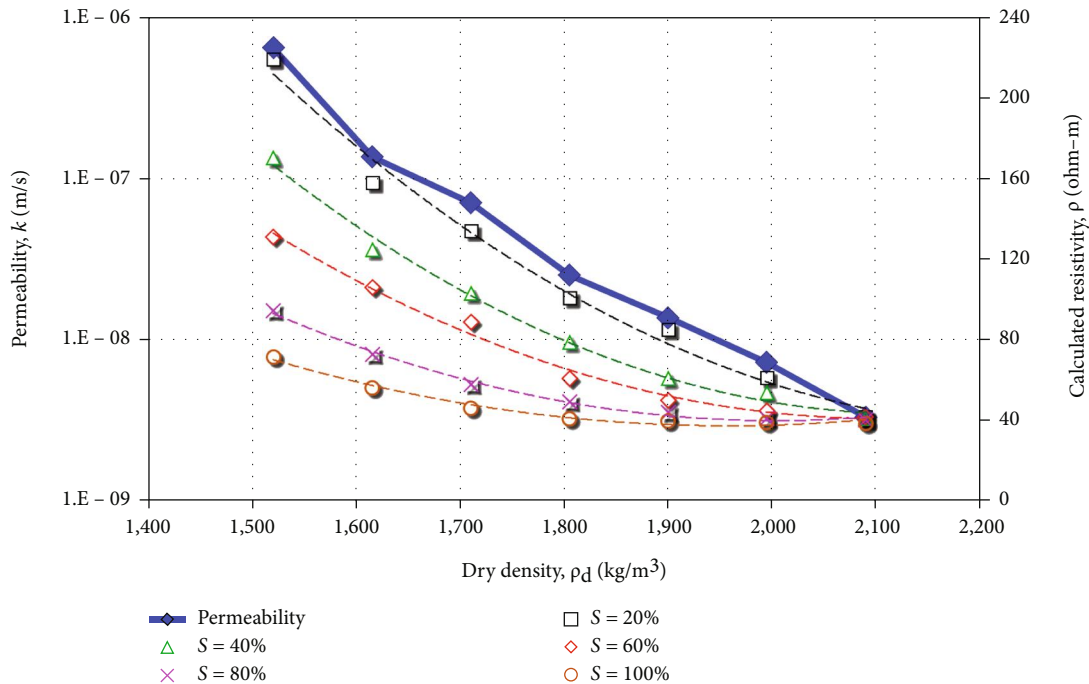
FIGURE 20: Results of laboratory tests on samples of matrix material from the Hattian Bala landslide dam, including permeability tests at different densities (plotted on a semilogarithmic scale on the primary vertical axis), and resistivity at different densities and degrees of saturation (on the arithmetic scale on the secondary vertical axes).

not possible to associate different zones to one type or the other source material. Thus, it was prudent to assume that the entire dam consisted of a mix of crushed sandstone and shale and the resistivity values in different zones were a reasonable representation of their respective densities, degrees of saturation, and permeability. A concise summary of the interpretations derived from these profiles is given below:

(i) *Phase 1 Longitudinal Survey.* This model indicated two low resistivity (interpreted as highly saturated) zones in the dam body. The limits of the first zone adjacent to the upstream toe of the dam were compatible with the Karli lake surface elevation of 1329 m AMSL, noted at that time. From the depth perspective, this zone extended below the original Karli channel bed level, whereas its longitudinal dimension was about 100 m. The second zone extended horizontally from approximately 260 m up to 685 m from the upstream edge of the spillway (freeboard edge), and its depth varied from near the surface to below the original Karli channel bed. A part of this zone also relates to the lowest point along segment 2 of the spillway where seepage water reappeared on the surface at two locations in February 2007. A medium resistivity (interpreted as intermediate density and permeability) zone was sandwiched between the two low resistivity saturated zones, which could hinder the development of smooth flow paths and thus impede the flow of water. A zone characterized by extremely high resistivity values (representing very high density and low permeability) was found in the subsurface towards

the end of the survey line extending horizontally from 780 m to 894 m from the upstream edge of the spillway. The resistivity values in this zone increased from about 650 ohm-m at the spillway bed to more than 6000 ohm-m at 150 m below that bed. Such high resistivity values could be attributed to the existence of very dense material and the possibility that the seepage fronts had not advanced through those layers by that time.

(ii) *Phase 1 Transverse Resistivity Surveys.* The four transverse resistivity profiles of phase 1 are shown in Figure 21. As mentioned above, these additional surveys were conducted to verify the profile obtained from the longitudinal survey. Since the longitudinal survey was conducted along the spillway bed, the main portions of interest from the transverse survey profiles were those below their lowest crest elevations (these elevations correspond to the spillway bed). The maximum depths of investigations for the transverse resistivity surveys at 22 m, 124 m, 237 m, and 574 m extended vertically up to 20 m, 26 m, 28 m, and 16 m below the spillway bed, respectively. The resistivity values of the 22 m transverse survey profile indicated an increase from 175 ohm-m at the spillway bed to 800 ohm-m at 20 m depth, whereas those of the 124 m transverse survey profile increased from 350 ohm-m at the spill bed to about 1000 ohm-m at 12 m depth and then decreased down to about 150 ohm-m at 26 m. For the third transverse resistivity survey at 237 m, the values varied between 95 ohm-m and about 1000 ohm-m
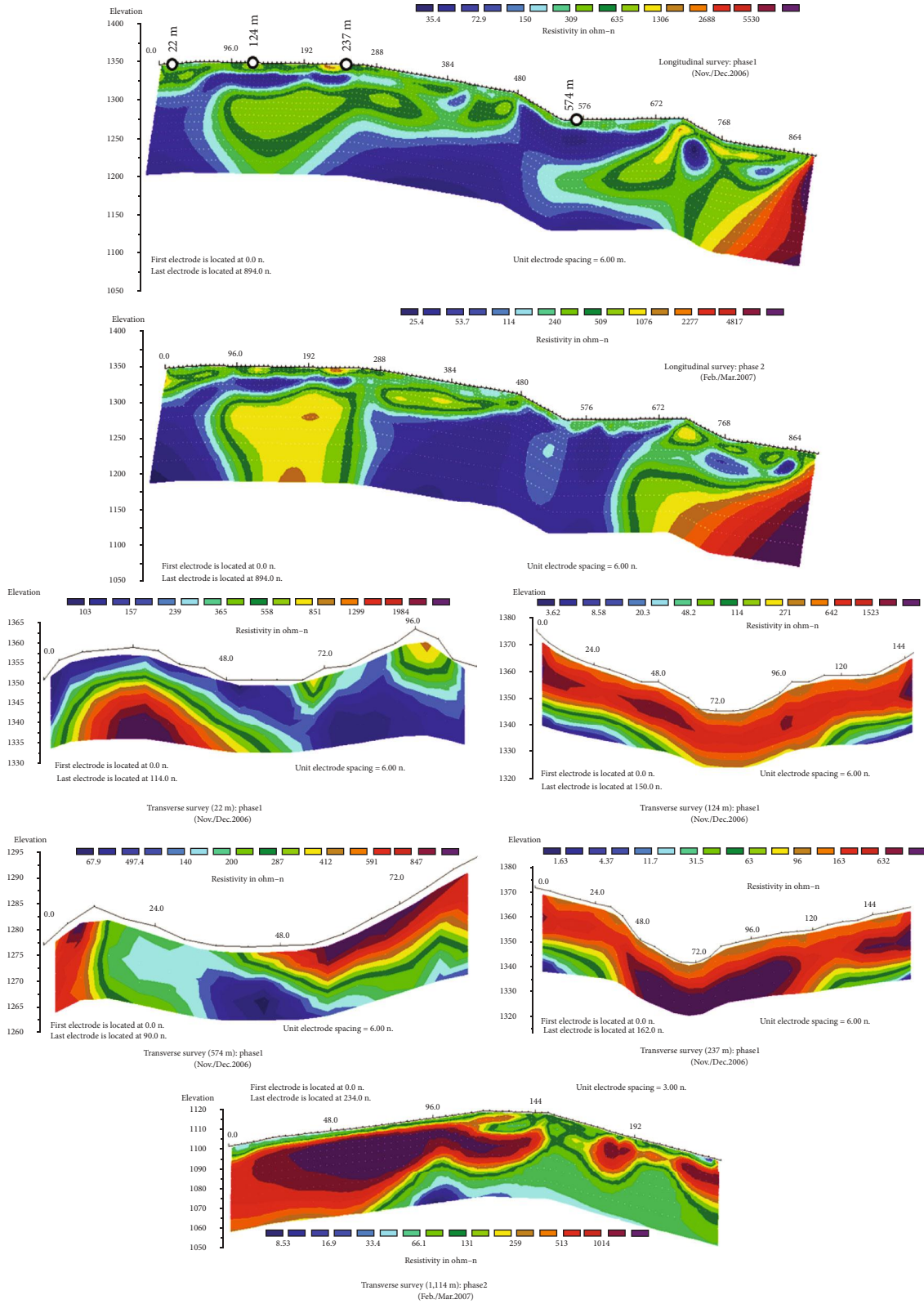
Figure 21: Longitudinal and transverse resistivity profiles of Karli spillway from RES2DINV modelling integrating data from two phases on field investigations.

within the 28 m depth zone, whereas for the transverse survey at 574 m, the value decreased from about 300 ohm-m at the spillway bed to about 60 ohm-m at 16 m depth. Interestingly, these resistivity values obtained from the transverse profiles are in general agreement with the values of the longitudinal profile of that phase, thus validating the subsurface inversion model and the interpreted conditions.

(iii) *Phase 2 Longitudinal Survey.* The time-lapse water infiltration longitudinal resistivity surveys, conducted during the phase 2 field investigations in February/March 2007, exhibited a general increase in the extents of low resistivity (high saturation) zones. This increase could be attributed to (1) rise in the Karli lake surface elevation by 7 m from December 2006 to March 2007 and (2) excessive rainfall (401.5 mm total) during a time-lapse of three months between the two phases of the surveys (Surface Water Hydrology Project, Water and Power Development Authority Pakistan, personal communication, unpublished data, March 2007). The surface runoff from the rainwater accumulated and percolated into the dam body, particularly at the lowest point along segment 2 of the spillway. The decrease in the resistivity values was maximum in the subsurface below that location.

(iv) *Phase 2 Transverse Resistivity Survey.* The only transverse resistivity survey of phase 2 was performed near the toe end of the dam (at 1114 m from the upstream end of the spillway). Accordingly, this survey line was located 220 m towards the downstream side from the end point of the longitudinal survey line of the two phases (also see Figure 12). Because of that distance, the results from this survey could not be used to validate directly any part of the longitudinal profile. However, it was conducted to investigate whether the extremely high resistivity zone observed near the end of the two longitudinal surveys further extended towards the downstream toe end. The profile developed from this 234 m long survey extended 41 m deep below the surface (see Figure 21). The reduced electrode spacing provided higher resolution. The results indicated variation of the resistivity values between 150 ohm-m and 1500 ohm-m within the top 25 m. The values were much lower than those observed in the end segment of the longitudinal surveys of both phases. It was interpreted that the extremely high resistivity zone found below the 780 m to 894 m stretch of the longitudinal survey gradually decreased in values towards the toe end of the dam. In the lower 15 m of the profile, the resistivity values decreased to less than 20 ohm-m. This low resistivity (interpreted as a highly saturated zone) corresponds to depths below the original channel bed. This particular observation hinted to a possible connection with the second low-resistivity saturated zone of the longitudinal surveys through the deeper strata.

4.2.5. Hydrological Database Analysis. The observations noted from the graphical presentation of the hydrological data and the calculations performed using the methodology explained in the previous section are summarized below:

(i) The surface elevation of the Karli lake constantly rose up to its maximum at 1352 m AMSL, when its water overtopped through the spillway on March 31, 2007

(ii) The Tung lake surface elevation fluctuated between 1215.71 m and 1223.10 m AMSL (in sync with periodic rainfall) for the duration of the data collection period. Comparing these levels with the Tung spillway elevation at 1223.10 m AMSL gave a clear indication of seepage resulting from internal erosion from that part of the landslide dam

(iii) The upstream inflows of the two channels and the downstream discharge for the period under consideration fluctuated between the following limits:

(a) Karli upstream: 0.257 and 2.897 m^3/s

(b) Tang upstream: 0.213 and 2.806 m^3/s

(c) Downstream: 0.370 and 2.870 m^3/s

(iv) During the dry spells (April, May, September, and October of 2006), the inflow from both lakes showed a decreasing trend

(v) The sum of the upstream inflow from both channels was distinctly higher (i.e., 1.47 times, on average) than the net downstream discharge (i.e., $Q_{in,combined} > Q_{out,combined}$) over the duration of the data collection period

(vi) The net downstream discharge was more than the net upstream inflow of the Tung channel for 95.44% of the data duration, except for the dates characterized by heavy rainfall (34 mm to 63 mm)

(vii) The two previous observations combined were indicative of one of the two possibilities: (1) water from the Karli lake was already contributing to the downstream discharge via seepage through the dam body or (2) ungauged hydrological features (i.e., nonperennial small channels and springs between the toe of the dam and the downstream measurement gauge) periodically added to the seepage from the Tung lake

(viii) The actual daily increase in the Karli lake volume ($Q_{vol.cont.}$), calculated using the polynomial expression of equation (2), when compared with those calculated as the total daily inflows from Karli channel ($Q_{vol.dis.}$), indicated that $Q_{vol.cont.} > Q_{vol.dis.}$ for the rainy days and few of the following days. However, the dry months (April, May, September, and October of 2006) showed an opposite trend, i.e., $Q_{vol.cont.} < Q_{vol.dis.}$

Table 5: Overtopping flow/seepage discharge and sediment concentration measurements.

Discharge location	February 26, 2007			April 2, 2007		
	Discharge (m^3/s)	Sediment concentration (mg/l)	Sediments smaller than (sieve size)	Discharge (m^3/s)	Sediment concentration (mg/l)	Sediments smaller than (sieve size)
No. 1	0.085	12,000	# 40	0.126	17,500	# 30
No. 2	0.115	23,450	# 20	0.234	29,650	# 16
No. 3	—	—	—	1.07	118,000	# 10
No. 4	—	—	—	0.86	106,500	# 10

(ix) The potential seepage volume ($Q_{out} \Delta t$) calculations from equations (2)–(5) over a period of 92 dry days from the data of the two channels yielded the following results:

(a) Total $Q_{in} \Delta t$ for 92 days = 10.8 million m^3

(b) Total downstream discharge for 92 days = 7.8 million m^3

(c) $Q_{out} \Delta t$ for 92 days = 7.3 million m^3 (67.6% of $Q_{in} \Delta t$ and 93.4% of the downstream discharge)

(d) $Q_{out} \Delta t$ trapped within the dam body = –0.5 million m^3

(x) One-third of $Q_{in} \Delta t$ from the two lakes was lost in seepage and evaporation, combined. The seepage part of the loss was occurring (1) below the Tung spillway, (2) due to water entrapped in the pore spaces of the main dam body (under the Karli spillway), and (3) from infiltration/seepage along the perimeter of the Karli lake surface with water touching fresh and relatively dryer strata for each daily rise in the level

(xi) The apparently unrealistic negative value of the seepage volume trapped within the dam body could also be attributed to contributions to the downstream discharge by the ungauged hydrological features mentioned above

(xii) The final breach of the two lakes, which occurred at a later timeframe (February and July of 2010), can be attributed to the slaking of the remnants of the coarse fragments of shale present within the dam body from the seepage and surface overflow, as reported by Kiyota et al. [14]

(xiii) The daily precipitation recorded for the duration of the data was noted to be less than the historical average shown in Figure 16(b) (except for November and December of 2006). Any future rainfall at or higher than the average could result in an increased rate of surface erosion as well as seepage forces due to the runoff from the adjoining slopes/catchment and the rainwater percolating into the dam surface

4.2.6. Seepage Discharge and Surface Flow Measurements from Karli Lake. The results of the field measurements, sampling, and laboratory testing from the surface water flow and seepage discharge at four locations along Karli spillway are summarized in Table 5. The results indicated the following:

(i) The discharge at the seepage points increased with time; their sediment concentration in the seepage flow was notable, which was a clear sign of internal erosion

(ii) The sediment concentration increased over the measurement period, and so did the sediment size, an indication of the evolution of internal erosion

(iii) The discharge measurements recorded from the overtopping flow at location 3 were lower than the upstream inflow from the Karli channel. Similarly, the discharge at location 4 along the spillway was lower than that at location 3. From this observation, it was deduced that a significant quantity of water from the streamflow was percolating into the dam body, resulting in an increase in the degree of saturation, and seepage pressures

(iv) The sediment concentration in the surface flow was significantly higher than that from the seepage discharge. The largest grain size being eroded due to surface flow was also larger than that from the seepage discharge. This assessment validated the interpretation of possible retrogressive erosion over time, which was derived from the erosion potential assessment detailed above

(v) These interpretations were based on the limited set of the readings tabulated above. Conclusive findings warranted continuous measurements of seepage and surface flow trends, together with upstream and downstream discharges and the lake elevations

4.2.7. Computer-Simulated Seepage Analysis. While numerical simulations and analysis for the seepage of water from Karli lake were performed in the SEEP/W program for three different lake elevations (1329 m AMSL in December 2006, 1336 m AMSL in early March 2007, and the maximum lake capacity of 1352 m AMSL on March 31, 2007), only selected results at the final elevation are presented in Figure 22. For the modelled scenarios, the phreatic surface, the flow lines, and the velocity vectors, shown in Figure 22, provided a decent understanding of the seepage flow patterns below the Karli spillway when reaching a steady-state condition. These assessments helped in relating the overall model to
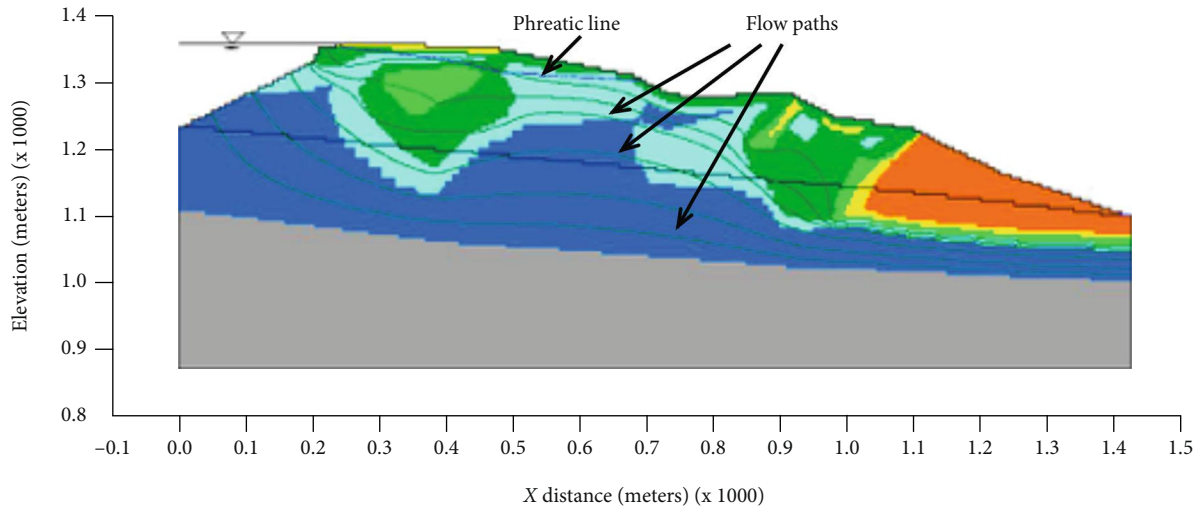
(a)
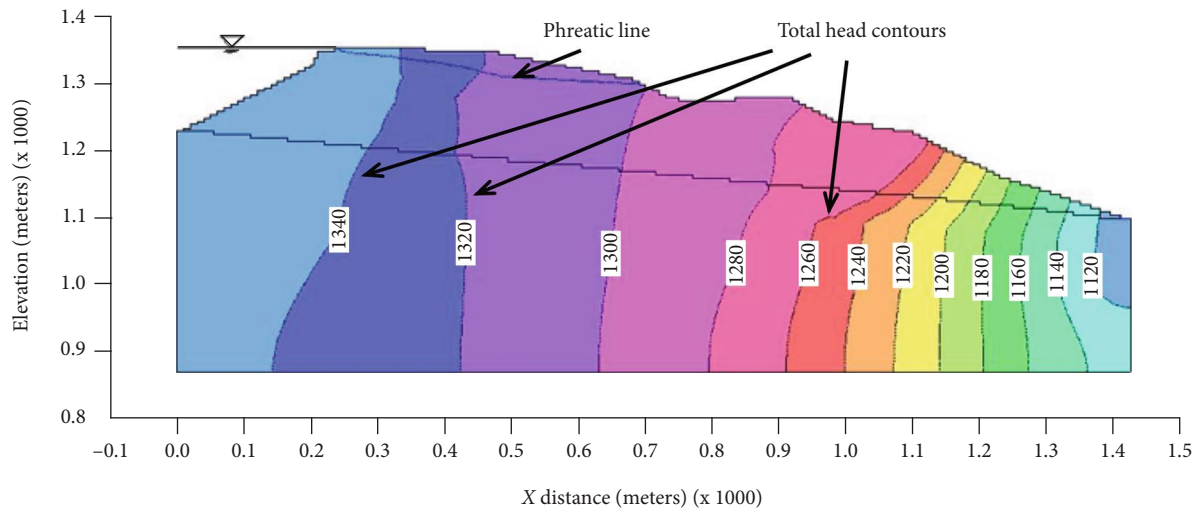
(b)
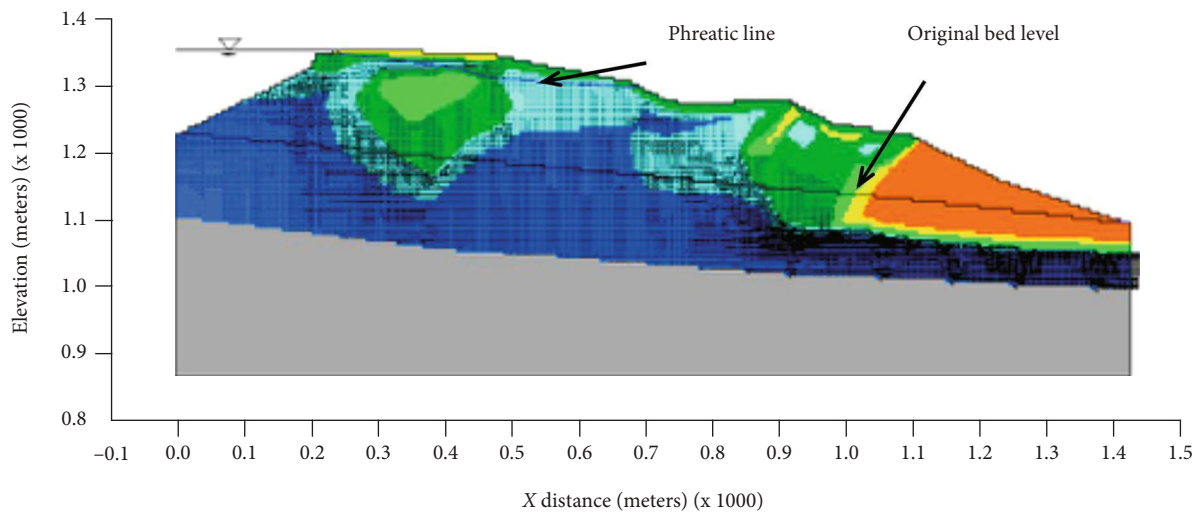
(c)

Figure 22: Continued.

(d)
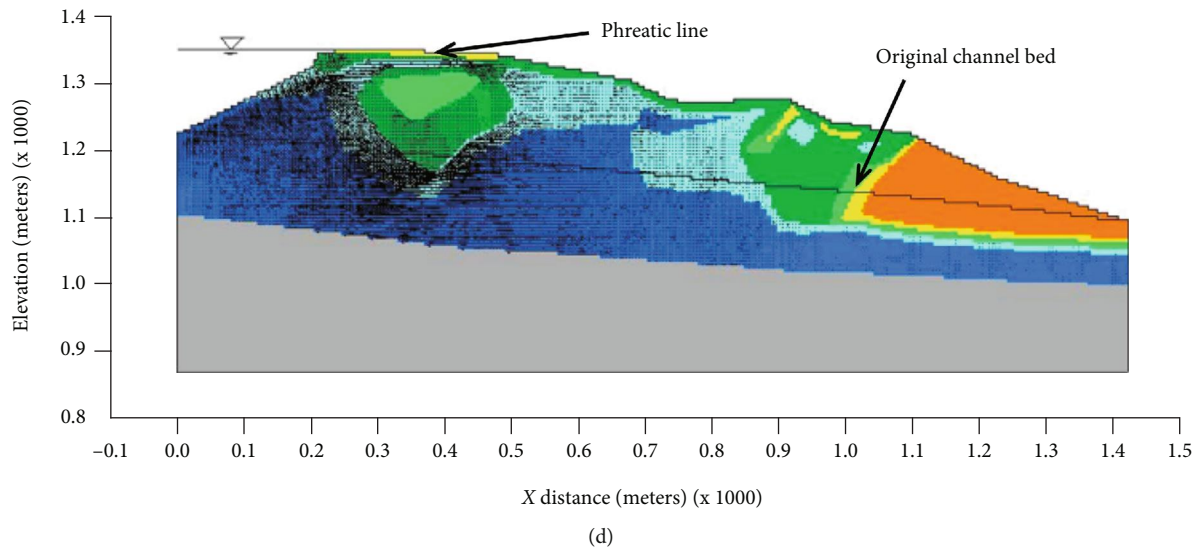
FIGURE 22: SEEP/W simulation results for Karli spillway (lake level at 1352 m AMSL): (a–c) flow paths, total head contours, and velocity vectors, respectively, for the head at the downstream toe end equal to the original channel bed, and (d) velocity vectors for zero flux at the downstream toe end.

the existing seepage locations and in estimating the future possible locations along the spillway. The following were explicated from the results:

(i) In the simulations modelled for three pondage levels with zero flux condition at the downstream toe end, the phreatic line daylights on the spillway surface very close to the upstream face of the dam (see Figure 22(d)). However, no such signs were observed during any phase of the site investigations or visits. It implied the possible use of incorrect downstream boundary conditions and/or a transient state of the actual seepage under the spillway in contrast to the steady-state model for which the analyses were run

(ii) The phreatic line, generated in the simulations with the downstream head at the same elevation as the original channel bed, daylights on the spillway surface near the lowest elevation point of its segment 2 (see Figure 22). As mentioned earlier, the two seepage points, initiated in February 2007, were located adjacent to this spot. Thus, this combination of boundary conditions and simulation seemed to be closer to the actual site conditions

(iii) The concentration of the flow paths (see Figure 22(a)) and the velocity vectors (see Figure 22(c)) lower in elevation than the original channel bed near the toe of the dam suggest that seepage in the toe zone of the dam would be unlikely, and therefore, the possibility of internal erosion/piping due to seepage forces would not be possible in that area (note that erosion in that zone due to surface flow was not analysed in this simulation). Nevertheless, keeping in view the difficulty in

conducting the resistivity survey and the ensuing RES2DINV modelling of the subsurface in the downstream toe segment, cautious interpretations from the simulation results are needed, particularly for that zone of the dam

(iv) The flow paths and the velocity vectors in all modelling and simulation cases indicate that a significant quantity of seepage water entering the dam from its upstream face would surge upwards towards the surface along segment 2 of the spillway after bypassing the first high resistivity (high density and low permeability) zone. The seepage locations 1 and 2 could be conveniently related to these results

(v) The total head contours shown in Figure 22(b) indicate that the head loss over the initial two-thirds of the dam width was less than that in the remaining one-third toe segment of the dam. These results evidenced an uneven distribution of seepage forces in different parts of the dam, which would possibly result in the appearance of seepage water back to the surface at multiple points along the uneven topography of the dam

(vi) To synopsize, a multidirectional approach was adopted for investigating an unconventional geotechnical and geological problem. Because of the inherent complexity and the many ungauged variables involved in the problem, a considerable degree of engineering judgement and observations had to be relied upon to reach reasonable qualitative results. The techniques employed for the analysis were more objective and based on newer data compared to those of the other preliminary studies conducted for this site

(vii) Under normal static conditions, the chance of a catastrophic failure was regarded as a rare possibility. Progressive failure due to internal erosion of fines as well as scouring at the surface and subsequent creep settlements were concluded to be part of the most likely scenario to develop over an extended duration. It was anticipated that an earthquake of high intensity, a sudden increase in the inflow due to excessive precipitation or cloud burst, or a large-scale landslide from the adjoining ridges into the Karli lake were the possible dynamic conditions that could significantly change the scenario

(viii) The hydrogeological immaturity of the dam was the main factor that continued to hinder any better assessment of the time needed for total washing out of fines and/or final development of the steady-state conditions. The findings and interpretations of this study were conveyed to the Engineering in Chief's Task Force in May 2007 along with the recommendation for continuation of the hydrological data monitoring system by the local authorities, together with periodic site visits/surveys to observe seepage and distress points along and besides the Karli spillway. Much of what happened at this site, as covered in the chronology of the events in an earlier section, was consistent with the interpretations from the authors' study

5. Summary of the Lessons

5.1. Observational Method. All landslide dams are characterized by rapid formation and deposition of a complex configuration and composition of geomaterials in the valley floor that are hydrogeologically young and pose a permanent threat to the downstream population and infrastructure due to the possibility of their failure. The fact that a predominant majority of them are known to have failed in the past mostly due to seepage-induced internal or surface erosion, and slope failure caused by the imbalance in the state of equilibrium generated by those seepage forces, calls for a need of their stability assessment. Determination of the condition of stability at any time after their formation or prediction of the period in which their failure would become imminent is extremely difficult. A certain set of investigations applied to one case may end up being mostly irrelevant to another due to the inherent uniqueness at each site, including the distinct dimensional, geological, topographical, and hydrological settings. The evolving scenarios would always depend on a variety of known or measureable variables and also with limitations imposed by some unknown and/or ungauged ones. This entails a substantial degree of reliance on engineering judgement and continuous monitoring.

Indeed, the landslide dams are excellent examples of the application of Terzaghi's Observational Method [34], which suggests initial computations for the working hypotheses based on preliminary data, followed by their confirmation or modification during the project implementation through continuous monitoring and data collection. The hypotheses considered must include the most probable condition as well

as the most unfavourable conceivable deviations. Vigilance is at the heart of this "learn as you go" approach.

5.2. Applicable Investigative Tools and Stages of Investigations. Despite the quandary mentioned above, the overall pattern of faring with these natural geomorphological features may possibly require most of the following:

(i) Site visit/reconnaissance to get the fundamental understanding of the scale of the problem and the overall site

(ii) The study of existing topographical, geological, hydrological, and seismic records of the site and the catchment area

(iii) A fresh topographical survey of the dam area to quantify the volume of the debris material and their thickness and slopes at cardinal points aligned with the original valley floor (or along the most likely alignment of the overtopping flow)

(iv) A higher resolution topographic survey of the catchment area to quantify the impounded volume of water corresponding to different lake levels and that of the maximum capacity

(v) The elaboration of a fresh hazard zonation map, especially including identification of the critical landslide slopes prone to failure in the catchment area

(vi) Bulk sampling of the coarse and fine fragments of the debris material

(vii) Field investigations mainly including the noninvasive geophysical methods/tools

(viii) Laboratory testing, including the grain size analysis, permeability assessment at different densities, erosion and slaking potential, and in situ and reduced density, strength, and stiffness due to the effects of sustained exposure to seepage water, and calibrations for field data including geophysical measurements (if employed)

(ix) A system of continuous monitoring including the inflows and outflows for the dam and the lake elevations, suspended sediment concentration in the seepage and the overtopping flow waters, and distresses and deformations along critical locations using DGPS systems

(x) Numerical modelling for seepage and deformation analyses based on the field measurements and calibrations from the laboratory tests

(xi) Dam break analysis using downstream topography and numerical modelling

(xii) Preparing early warning and evacuation systems and rehearsals for the downstream population

5.3. Need for an Updated Central Database. The Hattian Bala landslide dam has been added to the inventory of those limited cases that lasted for more than one year. The fact that its

failure, more than four years after formation, which was caused by excessive rainfall, is in agreement with the findings reported by Costa and Schuster [1] for previous failure cases. This specific case also attracted wide national and international attention because of the intensity of the earthquake that triggered the landslide and the overall catastrophic damage inflicted in that region. Both of these factors combined provided the required interest, reaction time, and resources to evaluate the problem and implement the mitigation measures. Other cases may not have the same latitude, requiring expeditious actions and with the constraint of even less data available (i.e., more unknown and/or ungauged variables), especially if the downstream population and/or infrastructure is at high risk. Full-scale mitigation work may not be an option due to the time and/or resource constraints. Therefore, employment of only selected investigative tools and steps from the above comprehensive list may be the best option. Availability of a central database of comprehensive case histories (from inception to failure or to stability) of the worldwide landslide dams, a summarized set of information from each case, and the overall comparative analysis will be helpful in handling future events of landslide dams.

5.4. Noninvasive Geophysical Methods. The invasive type of field investigation methods is not suited for this category of geotechnical problems as those methods provide information very specifically related to the point of investigation. Since the composition and configuration of landslide dams can be highly complex and heterogeneous, selective nonconventional tools like the noninvasive geophysical methods may be the only practical solution in the majority of cases. Geophysical methods cover large areas (vertical and lateral extents), they are expedient and less expensive, and they assess characteristics at small strain (i.e., true representation of elastic properties). However, since they develop a general picture instead of precise information (i.e., they provide qualitative results instead of quantitative), their interpretations require considerable prior experience and knowledge. In addition, laboratory calibrations of the measurements on the samples from the site are also warranted.

5.5. Numerical Simulations. Numerical modelling and computer simulations via reliable software can be very helpful in predicting the seepage and deformation of landslide dams. However, the model developed for this purpose, founded on data obtained from the use of geophysical or other investigation tools, must be a good representation of the subsurface strata and composition, and the values of the variables assigned in that model must be based on high-quality laboratory calibrations.

5.6. Hydrological Model. The hydrological database model presented in this paper for estimating the potential seepage volume can be refined for future applications by accounting for evaporation losses during the dry days, provided that temperature measurements are taken at or close to the site. Similarly, the model for the rainy days can also be developed by incorporating surface runoff data and contributions of perennial and nonperennial channels and springs. Accord-

ingly, the authorities and investigators dealing with the analysis of the stability and mitigation of the landslide dams should strive to acquire that information during their data collection phase. Furthermore, the potential seepage volume cannot be estimated reliably until the lake has filled to its capacity or a reasonable pore water pressure equilibrium has been reached within the dam. This entails that the application of this proposed model would require continuous and extended monitoring of the hydrological data.

5.7. Collaborative Investigations. Because of the diverse nature of the variables involved in these problems, a collaborative cross-disciplinary approach of investigations and analysis is needed. Accordingly, knowledge and experience from geology, hydrology, seismology, meteorology, and geotechnical engineering has to be combined towards a cogent solution to such problems. While the application and combination of most of the above-mentioned fields were illustrated in the Hattian Bala case study, the field of seismology is also relevant in view of possible slope failures in the catchment area of the impounded lake due to an earthquake. A sudden slope failure due to a seismic event can generate a tsunami wave in the lake that may result in the dam break.

5.8. Qualitative versus Quantitative Findings. Precise prediction of the rate and progress of internal erosion and scouring and the resulting creep deformations is very difficult due to the extreme heterogeneity of the material within the overall dimensions of the landslide dams. Therefore, the combination of observational methods together with monitoring, vigilance, and early warning systems should be integral to any landslide dam project.

Data Availability

The data that support the findings of this study are available from the corresponding author upon reasonable request.

Conflicts of Interest

The authors declare that there is no conflict of interest regarding the publication of this paper.

Acknowledgments

References

[1] J. E. Costa and R. L. Schuster, "Documented historical landslide dams from around the world," *U.S. Geological Survey Open-File Report no. 91-239*, U.S. Geological Survey, 1991.

[2] R. L. Schuster, "Landslide dams – a worldwide phenomenon," in *Proceedings of the Annual Symposium of the Japanese Landslide Society*, pp. 1–23, Osaka, 1993.

[3] O. Korup, "Recent research on landslide dams - a literature review with special attention to New Zealand," *Progress in Physical Geography*, vol. 26, no. 2, pp. 206–235, 2002.

[4] W. O. Engemoen, "Assessing the risk of a seepage-related dam failure by means of failure mode identification, risk analysis, and monitoring practices," in *Proceedings of the Research Workshop on Seepage Through Embankment Dams*, Denver, Colorado, 2000.

[5] R. P. Denlinger, D. R. H. O'Connell, and M. Jones, *Summary of preliminary 2D inundation modeling for three Hattian landslide dam breach scenarios*, Open-File Report no. 2006–1094, A joint project of the U.S. Geological Survey and the U.S. Department of Interior, Bureau of Reclamation, 2006.

[6] Asian Development Bank (ADB) and World Bank, *Pakistan -2005 earthquake preliminary damage and needs assessment (English), Report no. 34407*, World Bank Group, Washington, D.C, 2005, http://documents.worldbank.org/curated/en/710481468284380489/Pakistan-2005-earthquake-preliminary-damage-and-needs-assessment.

[7] Google Earth, "Satellite image," 2005, http://www.earth.google.com.htm.

[8] K. Hoeg, O. A. Hoydal, V. Kveldsvik, O. Kjekstad, R. OlssonAll et al., *The Pakistan October earthquake report from NGI's second mission, 4–11 January 2006, Hattian Bala landslide dam*, Norwegian Geotechnical Institute, 2006.

[9] National Engineering Services Pakistan, (Private) Limited (NESPAK), and Geological Survey of Pakistan, *Potential hazard of landsliding and mitigation measures at Hattian Bala and other earthquake hit areas, study of Hattian Bala landslide*, A Joint Investigation Report, National Engineering Services Pakistan, 2006.

[10] A. Sattar, K. Konagai, T. Kiyota, T. Ikeda, and J. Johansson, "Measurement of debris mass changes and assessment of the dam-break flood potential of earthquake-triggered Hattian landslide dam," *Landslides*, vol. 8, no. 2, pp. 171–182, 2011.

[11] K. Konagai and A. Sattar, "Partial breaching of Hattian Bala landslide dam formed in the 8th October 2005 Kashmir earthquake, Pakistan," *Landslides*, vol. 9, no. 1, pp. 1–11, 2012.

[12] N. Abeer, *Landsliding and mitigation measures in earthquake affected areas, Engineer-in-Chief's Branch, Pakistan Army*, A power point presentation delivered to Military College of Engineering, National University of Sciences and Technology, Risalpur, Pakistan, 2006.

[13] Google Map, "Satellite imagery," 2020, https://www.google.com/maps.

[14] T. Kiyota, A. Sattar, K. Konagai, Z. A. Kazmi, D. Okuno, and T. Ikeda, "Breaching failure of a huge landslide dam formed by the 2005 Kashmir earthquake," *Soils and Foundations*, vol. 51, no. 6, pp. 1179–1190, 2011.

[15] A. Sattar, K. Konagai, T. Ikeda, T. Kiyota, Z. A. Kazmi, M. Koikes et al., "A quantitative approach to assess landform changes of Hattian Ballah landslide dam formed by the 2005 Kashmir Earthquake," *Bulletin of Earthquake Resistant Structure Research Center*, no. 42, pp. 19-20, 2009.

[16] M. Basharat, J. Rohn, and M. R. Khan, "Effect of drawdown of Karli lake: a case study of Karli landslide hazard in District Hattian, Northeast Himalayas of Pakistan," *Life Science Journal*, vol. 11, no. 9, pp. 610–616, 2014.

[17] J. F. Schneider, F. E. Gruber, and M. Mergili, "Recent cases and geomorphic evidence of landslide-dammed lakes and related hazards in the mountains of Central Asia," in *Landslide Science and Practice*, C. Margottini, P. Canuti, and K. Sassa, Eds., pp. 57–64, Springer, Berlin, Heidelberg, 2013.

[18] Google Earth Timelapse, "Zalzal lake 34°09'17"N, 73°42'11"E, Camera: 9250 m," 2020, https://earthengine.google.com/timelapse/.

[19] ASTM D6431–18, *Standard guide for using the direct current resistivity method for subsurface investigation*, ASTM International, West Conshohocken, PA, 2018.

[20] M. H. Loke, *Tutorial: 2-D and 3-D electrical imaging survey- Course notes*, Geotomo software, Penang, MalaysiaJuly 2020, https://www.geotomosoft.com/downloads.php.

[21] ASTM D6913/D6913M–17, *Standard test methods for particle-size distribution (gradation) of soils using sieve analysis*, ASTM International, West Conshohocken, PA, 2017.

[22] ASTM D1140–17, *Standard test methods for determining the amount of material finer than 75-μm (no. 200) sieve in soils by washing*, ASTM International, West Conshohocken, PA, 2017.

[23] ASTM D4318–17, *Standard test methods for liquid limit, plastic limit, and plasticity index of soils*, ASTM International, West Conshohocken, PA, 2017.

[24] ASTM D2487–17e1, *Standard practice for classification of soils for engineering purposes (unified soil classification system)*, ASTM International, West Conshohocken, PA, 2017.

[25] ASTM D5856–15, *Standard test method for measurement of hydraulic conductivity of porous material using a rigid-wall, compaction-mold permeameter*, ASTM International, West Conshohocken, PA, 2015.

[26] ASTM G57–06, *Standard test method for field measurement of soil resistivity using the Wenner four-electrode method*, ASTM International, West Conshohocken, PA, 2012.

[27] R. Fell, C. F. Wan, J. Cyganiewicz, and M. Foster, "Time for development of internal erosion and piping in embankment dams," *Journal of Geotechnical and Geoenvironmental Engineering*, vol. 129, no. 4, pp. 307–314, 2003.

[28] W. Meyer, R. L. Schuster, and M. A. Sabol, "Potential for seepage erosion of landslide dam," *Journal of Geotechnical Engineering*, vol. 120, no. 7, pp. 1211–1229, 1994.

[29] J. L. Sherard, "Sinkholes in dams of coarse, broadly graded soils," in *Transactions, 13th International Congress on Large Dams (ICOLD)*, vol. 2, pp. 25–35, New Delhi, India, 1979.

[30] A. Kézdi, *Soil Physics*, vol. 25, Elsevier Scientific Publishing Company, Amsterdam; Oxford, New York, 1979.

[31] Climate Data Oline, *Precipitation data: Islamabad, PK (CITY:PK000003) 1980-01-01 to 2018-12-31*National Centers for Environmental Information, National Oceanic and Atmospheric Administration (NOAA)July 2020, https://www.ncdc.noaa.gov/cdo-web/datasets/.

[32] ASTM D3977–97 (Re-approved 2019), *Standard test methods for determining sediment concentration in water samples*, ASTM International, West Conshohocken, PA, 2012.

[33] V. F. De Mello, "Some lessons from unsuspected, real and fictitious problems in earth dam engineering in brazil," in *Proceedings of the 6th Regional Conference for Africa on Soil Mechanics and Foundation Engineering*, Durban, South Africa, 1975.

[34] R. B. Peck, "Advantages and limitations of the observational methods in applied soil mechanics," in *Géotechnique*, vol. 19 of Ninth Rankine Lecture, no. 2, 1969.

WILEY | Hindawi

Research Article

A Comparison of Simplified Modelling Approaches for Performance Assessment of Piles Subjected to Lateral Spreading of Liquefied Ground

Yung-Yen Ko [iD] [1] **and Yu-Ying Lin** [2]

[1]*Department of Civil Engineering, National Cheng Kung University, Tainan 70101, Taiwan*
[2]*National Center for Research on Earthquake Engineering, National Applied Research Laboratories, Taipei 10668, Taiwan*

Correspondence should be addressed to Yung-Yen Ko; yyko@mail.ncku.edu.tw

The lateral spreading of the ground due to liquefaction during earthquakes may considerably damage the embedded piles, which is an important issue in the seismic design of pile foundations. In this paper, nonlinear pseudostatic analyses were performed for the responses of piles subjected to actions of laterally spreading ground, which were modelled as flow displacement and flow pressure, respectively. The former is a displacement-based approach, in which the free-field ground displacement profile is assigned to the pile-soil interaction system; while the latter is a force-based approach, which regards the actions of laterally spreading ground as flow pressure and directly applies it to the pile. The concept of the Winkler foundation was utilized to account for the interaction between pile and soil. The soil springs with elastic-plastic *p-y* curves were used to describe the relationship of soil reaction versus lateral displacement around the pile. The distributed plastic hinges were deployed to simulate the possible flexural failure of the pile. One of the pile failure cases caused by liquefaction-induced lateral spreading in the 1995 Kobe Earthquake was adopted for case study. The analyzed pile response to flow displacement and flow pressure was compared with the field observations, and the validity and capability of both approaches were accordingly discussed. The influence of axial load on laterally loaded piles, namely, the P-delta effect was also examined. These results help to reasonably assess the performance of piles subjected to lateral spreading of liquefied ground.

1. Introduction

Pile foundations are common for their excellent bearing capacity and displacement control capability. The lateral resistance is one of the most important functions of piles in seismic active areas such as Japan and Taiwan, because it helps to withstand earthquake loading. However, the lateral resistance of a pile is mainly attributed to shallow soil layers because its deflection when laterally loaded is larger near the ground surface, where generally higher liquefaction potential is exhibited than at a greater depth for liquefiable ground due to lower overburden stress. Therefore, the seismic performance of piles may be significantly influenced by soil liquefaction.

During earthquakes, not only the lateral inertia loads transmitted from the superstructure but also the actions of lateral spreading of liquefied ground could be applied to piles, and the latter are usually more destructive because the lateral resistance of the pile is simultaneously reduced because the stiffness and strength of soil are degraded by liquefaction. Concerning piles embedded in laterally spreading ground, usually, the flexural failure is dominant because of the considerable bending moment generated by the actions of lateral spreading. Buckling instability may also occur for slender piles due to the combination of axial load and lateral deflection, namely, the P-delta effect [1], as well as the loss of lateral confinement because of the degradation of liquefied soil. Many cases have been reported, mostly related to

foundations of structures near waterfront, such as bridges along or across rivers, or wharves, tanks, and buildings in the port area.

Therefore, this study aims to investigate the lateral performance of piles subject to the actions of lateral spreading of the ground triggered by liquefaction. The widely used the Winkler foundation model, in which the pile is simulated by beam-column elements (also known as frame elements) and soil reactions are simulated by spring elements along the pile, is utilized to represent the pile-soil interaction. Elastic-plastic relationships between soil reaction (p) and lateral displacement (y), namely, p-y curves, are used to define the soil springs. The distributed plastic hinge method is adopted to simulate the possible flexural failure of the pile. Thus, the nonlinear behavior of the pile-soil system can be well exhibited at a reasonable analysis cost. In engineering practice, the actions on piles due to the lateral spreading of the liquified ground are usually simplified as flow displacement, which is also known as the displacement-based approach, e.g., [2, 3], or as flow pressure, which is also known as the force-based approach, e.g., [2, 4], and both will be introduced herein. In addition, a case study of pile failure caused by laterally spreading ground in the 1995 Kobe Earthquake using both modelling approaches will be presented and compared, and their validity and capability will be discussed. The investigation of the influence of axial load on pile performance against lateral spreading will also be included. Results of this study can be therefore served as the reference of the seismic performance assessment of piles embedded in liquefiable ground.

2. Pile Damage due to Lateral Spreading of Liquefied Ground

2.1. Liquefaction-Induced Lateral Spreading. During earthquakes, finite lateral displacement of gently sloping ground underlain by liquefied soil such as loose sands with a shallow groundwater table may occur due to the build-up of excess pore pressure or even liquefaction in the underlying deposit, as shown in Figure 1(a) [5]. This is often called the lateral spreading of the ground. Gently sloping means a slope less than 6%, or the flow failure may occur [6]. A steep free face giving an unrestricted boundary, e.g., riverbank or seashore, is common in lateral spreading.

The profile of laterally spreading ground is shown in Figure 1(b), which can be divided into a nonliquefied (unsaturated, impervious, or clayey) surface layer (so-called crust layer) and a liquefied (saturated, loose, and sandy) underlying layer. Tension cracks or ground fissures perpendicular to the direction of spreading as well as slumping are often found on the ground surface, especially near the upper margins of the spreading area.

2.2. Actions of Lateral Spreading on Piles. Based on the observations in the 1995 Kobe Earthquake, the pile foundations embedded in liquefied and laterally spreading ground were damaged mainly due to the kinematic forces arising from horizontal ground displacement, and for friction piles, settlement and tilting with the adjacent ground surface were

caused [7]. The pile response in liquefiable soils can be differentiated as cyclic phase and lateral spreading phase [8]. In the former, inertial forces mainly from the superstructure are dominant, while in the latter, they play an important role only at the onset of lateral spreading because the shaking intensity diminishes as the spreading progresses. On the other hand, the kinematic load induced by the lateral ground movement becomes the controlling factor of the pile response in the lateral spreading phase.

The actions of lateral spreading on piles can be further examined experimentally via the induced lateral pressure, or, soil reaction to the piles. Brandenberg et al. [9] found through centrifuge tests that the nonliquefied crust displaced more than the liquefiable layer and imposed larger soil reaction on the pile, yet large relative displacements between the pile and the crust were required to mobilize peak crust loads acting on the pile. In contrast, actions from the liquefiable layer could be complex if the crust pulled the pile downslope such that the downslope movement of the pile was greater than that of the liquefiable soil, which was possible for more flexible piles. Haeri et al. [10] reported based on 1-g shaking table tests that the maximum lateral soil pressure along the piles in liquefiable layer increased almost linearly with the depth, namely, showed approximately a triangular pattern same as the simplified flow pressure profile due to lateral spreading proposed by Japan Road Association (JRA) [4], which will be introduced later; however, the observed maximum pressures were higher than those specified in [4] for a single pile, yet were reasonably in agreement for piles with neighboring ones. According to the observations in a large scale 1-g shaking table test, Motamed et al. [11] concluded that the JRA simplified flow pressure seemed appropriate for closely spaced pile groups, which is conformable to [10], and was therefore considered useful in preliminary analysis.

2.3. Cases of Pile Damage Related to Lateral Spreading. In the 1964 Niigata Earthquake, soil liquefaction and its devastating effects started to catch the attention of engineers. For example, a public building suffered flexural failure of piles which concentrated at the interface of the liquefied and nonliquefied layers because the lateral spreading induced permanent ground displacement, and piles moved by nonliquefied soil layers were even worse damaged [12]. Another widely known case is the collapse of the Showa Bridge possibly, which was possibly due to the combined effect of axial load and lateral spreading which led to buckling instability of piles [1].

The Mw 6.9 1995 Kobe Earthquake brought severe damages to reclaimed lands along the shoreline of Kobe City, especially in the Port of Kobe, mainly because of liquefaction and lateral spreading [13]. Several facilities and buildings experienced pile failure caused by laterally spreading ground. In a pile-supported wharf, a horizontal displacement up to 1.7 m at the deck and local buckling of the steel pipe piles associated with significant lateral deformation of the sand layer were observed [14]. The seaward movement of a quay wall damaged the precast concrete (PC) piles of a nearby oil-storage tank in terms of lateral deformation and flexural cracks, which were
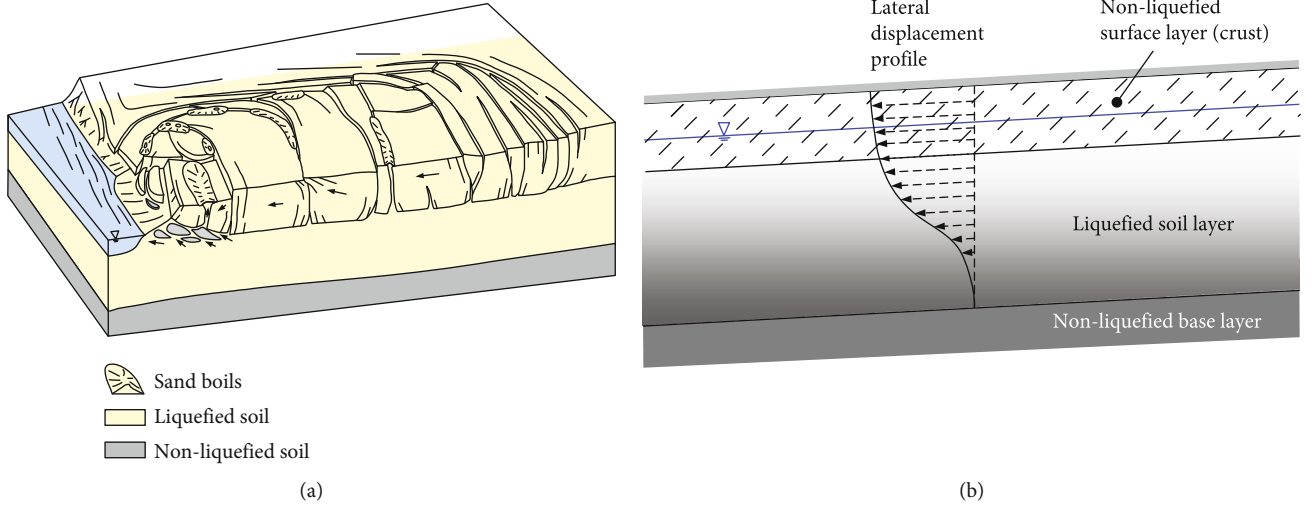
FIGURE 1: Liquefaction-induced lateral spreading. (a) Schematic depiction. (b) Lateral displacement profile. (After [5]).

more severe near the interface of the liquefied fill deposit and underlying silty soil layer [15]. The PC piles of a building near the waterfront were severely cracked and even broken due to a displacement above 1.5 m of the quay wall, which led to considerable tilting of the super-structure [16], which was adopted for case study in this paper and more details will be given later.

A more recent case was reported in the 2016 Kaikoura, New Zealand Earthquake, that a lateral spreading with a displacement of 0.8-1.0 m at the edge of the fill pushed a pile-supported wharf to a tilt of 1~2.5° and a seaward moment of 0.2~0.5 m [17].

3. Modelling of Actions of Lateral Spreading on Piles

Figure 2(a) shows the typical condition of a pile undergoing lateral spreading of liquefied ground. The moving soil body leans against the pile; meanwhile, the soil reaction to provide lateral resistance of the pile is reduced due to liquefaction. Flexural deformation and bending moment of the pile are thus caused. Lateral spreading is even damaging if there is a nonliquefied surface layer, which is also known as the crust layer because its interaction with the pile is more significant. Two methods which are common in engineering practice for the modelling of these actions are introduced as follows.

3.1. Lateral Spreading as Flow Displacement. Firstly, the free-field ground displacements profile due to lateral spreading is estimated and then assigned as the boundary conditions to the free ends of the soil springs (other than those ends attached to the pile) in the liquefied layer, as shown in Figure 2(b). It might be necessary to reduce the subgrade reaction coefficients or the p-y curves of the soil springs based on the liquefaction potential of the corresponding soil layers to account for the degradation of liquefied soil. Then, forced displacement analysis can be accordingly performed.

The simplified approximation of liquefaction-induced ground displacement proposed by Tokimatsu and Asaka [18] was adopted in this study. The horizontal displacement

of the ground surface, $D(x)$, at a distance from the waterfront of x can be approximated as:

$$D(x) = D_0 \left(\frac{1}{2}\right)^{5x/L_{ls}} \tag{1}$$

where $D_0 = D(x = 0)$, denoting the horizontal displacement of the ground surface at the waterfront, and L_{ls} is the length of the laterally spreading area. Based on the field data of ground displacement induced by lateral spreading in the 1995 Kobe Earthquake, $L_{ls} = (25 \sim 100) D_0$, and $L_{ls} = 50 D_0$ can be regarded as representative.

Then, the ground displacement profile of a laterally spreading deposit, $d_{ls}(z, x)$, at a distance from the waterfront of x can be approximated as:

$$
\begin{aligned}
d_{ls}(z, x) &= D_0 \left(\frac{1}{2}\right)^{x/(10 D_0)} && \text{for } 0 \leq z < z_w \\
d_{ls}(z, x) &= D_0 \left(\frac{1}{2}\right)^{x/(10 D_0)} \cos\left[\frac{\pi(z - z_w)}{2 H_L}\right] && \text{for } z \geq z_w
\end{aligned}
\tag{2}
$$

where z is the depth below the ground surface; z_w and H_L denote the depth at the top of the liquefied layer and its thickness, respectively.

3.2. Lateral Spreading as Flow Pressure. As shown in Figure 2(c), the actions of lateral spreading are represented by flow pressure directly imposed on the pile. JRA [4] proposed that the flow pressure profile in the nonliquefied crust layer with respect to the depth z, $q_{NL}(z)$, and that in the liquefied layer, $q_L(z)$, can be expressed as:

$$q_{NL}(z) = c_s c_{NL} K_P \gamma_{NL} z \quad \text{for} \quad 0 \leq z \leq H_{NL}, \tag{3}$$

$$q_L(z) = c_s c_L [\gamma_{NL} H_{NL} + \gamma_L(z - H_{NL})] \text{for} \quad H_{NL} < z \leq H_{NL} + H_L, \tag{4}$$
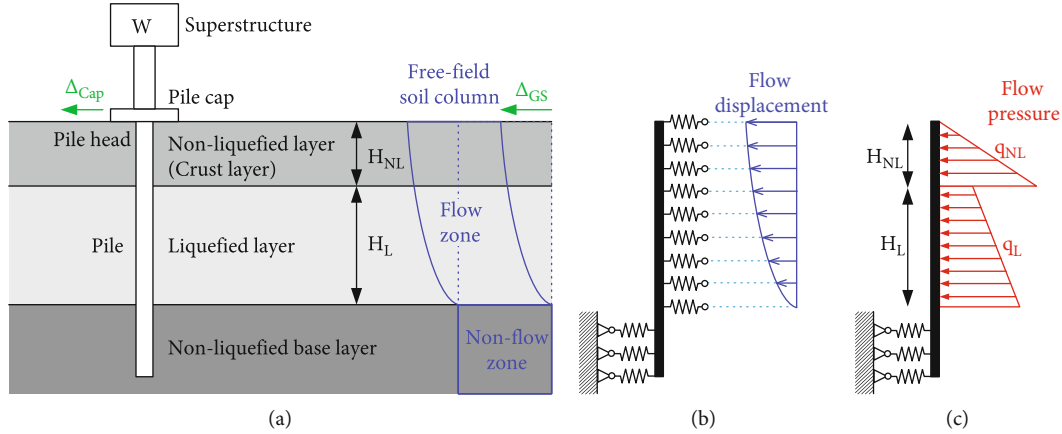
Figure 2: Actions of lateral spreading on pile. (a) Typical condition. (b) Modelled as flow displacement. (c) Modelled as flow pressure.

where K_P is the passive earth pressure coefficient; H_{NL} and H_L are the thickness, and γ_{NL} and γ_L are the unit weight of the nonliquefied crust and liquefied layers, respectively; c_L is the modification factor for flow pressure in the liquefied layer, which is suggested to be 0.3, while that in the nonliquefied layer, c_{NL}, is based on the liquefaction potential index (often denoted as P_L or LPI) defined in [19]; c_s is the modification factor based on the distance from the waterfront. Suggested values of c_{NL} and c_s are listed in Table 1.

As mentioned in Section 2.2, this simplified pressure profile in liquefied layer can be considered reasonable for closely spaced piles [10, 11], and to mobilize the flow pressure in the nonliquefied layer, which is regarded as passive earth pressure in [4], large relative displacements between piles and soil are needed [9]. In addition, it is noted that the flow zone in Figure 2(a) induces flow pressure but provides no soil reaction, while the nonflow zone induces no flow pressure but provides soil reaction.

4. Case Study

4.1. Case Introduction. A 3-story building located at the coastal area of Kobe City which suffered pile damage due to lateral spreading of liquefied ground during the 1995 Kobe Earthquake [16], as mentioned in Section 2.3 and as shown in Figure 3, was adopted for case study. This lateral spreading induced a seaward movement of about 1.6 m of a neighboring quay wall at the waterfront, and a ground surface displacement around 0.9~1.1 m was observed at the base of the building. 38 PC piles which had a length of 20 m and a hollow cross-section with an outer diameter of 400 mm and a wall thickness of 65 mm were installed for this building by preboring method. Pile S-7 and Pile N-7 in Figures 3(a) and 3(b) suffered horizontal and longitudinal cracks at the pile head and near the interface between the reclaimed fill and the underlying sand layer (at a depth of about 9 m), and Pile S-7 was even broken at a depth of 4.5 m with a crack up to 40-100 mm wide. The superstructure was therefore tilted about 3° (or, 1/18).

The boring data of the site from [16] are shown in Figure 3(c), and the corresponding soil types and blow counts of standard penetration test (SPT-N) are listed in

Table 2. The SPT-N values of the reclaimed fill were mostly no more than 10, and this layer could be in a loose state. The sand layer had SPT-N ranged from 14 to 24 and was probably medium dense. Low SPT-N values were noticed in the sandy silt layer, and a relatively high fine content (FC) could be expected though the data were not available. The gravelly sand layer was stiff for its high SPT-N up to 50. Considering a horizontal peak ground acceleration (PGA) of 300 gal based the real earthquake record at a reclaimed land as well as a groundwater level at a depth of 2 m [16], the liquefaction potential was assessed using the simplified procedure proposed by Architectural Institute of Japan (AIJ) [20], which was considered more reasonable in general because it included the influence of fine content on liquefaction potential, as well as the cyclic mobility of dense sand in the reduction of stiffness and strength of liquefied soil [21]. In calculating the factor of safety against liquefaction (F_L) of a soil layer, its cyclic resistance ratio (CRR) is determined by the SPT-N corrected based on the FC values, which were assumed based on the soil types given in [16]. The soil layer is considered liquefied if $F_L < 1$, yet the sandy silt layer was directly regarded as nonliquefiable (N.L.) herein because of its high fine content. The results are given in Table 2, indicating that the upmost nonliquefied (crust) layer above the groundwater table with a thickness around 1~2 m was underlain by a liquefied layer with a thickness around 7~8 m, which was basically the reclaimed fill, and beneath the liquefied layer was the lower nonliquefied layer comprised of sand, sandy silt, and gravelly sand. These results are conformable to [16]. In addition, the reduction factors (D_E) for the mechanical parameters of liquefied soil suggested in [20] based on F_L and SPT-N are also included in Table 2, and D_E will be used in the following analysis to reduce the *p-y* curves for the liquefied layer.

It is noted that the cracks of the piles at a depth of 9 m were in fact at the interface between the liquefied and lower nonliquefied layers, and the breakage at a depth of 4.5 m was within the liquefied layer, close to where $D_E = 0$.

4.2. Analysis Model. The structural analysis software SAP2000 was adopted to perform nonlinear pseudostatic analysis for the response of piles subjected to lateral

TABLE 1: Modification factors for flow pressure [4].

P_L	c_{NL}
$P_L \leq 5$	0
$5 < P_L \leq 20$	$(0.2P_L - 1)/3$
$P_L > 20$	1
Distance to waterfront, s (m)	c_s
$s \leq 50$	1.0
$50 < s \leq 100$	0.5
$s > 100$	0

spreading. The P-delta effect, which involves large tensile or compressive stresses on transverse bending and shear behavior, and large displacement effect, in which deformed configuration is considered in all the equilibrium equations, were included to account for the possible geometric nonlinearity [22]. Figures 4(a) and 4(b) show the analysis models of Pile S-7 and Pile N-7 in Figure 2 in which the lateral spreading modelled as flow displacement and flow pressure, respectively, with the dimensions based on [23]. Details of the models are given as follows.

4.2.1. Modelling of Pile-Soil Interaction.

The Winkler foundation model is utilized for the simulation of pile-soil interaction, that is, the pile is modelled by frame elements, and the soil reactions are modelled by spring elements deployed along the pile. However, for the model in Figure 4(b), no soil springs were generated in the flow zone (including the crust and the liquefied layer) for its not providing soil reaction when modelled as flow pressure. Elastic-plastic p-y curves for the soil springs are used to represent the nonlinearity of supporting soil. A rigid body constraint was specified to both pile caps to approximate the connection provided by the pile cap as well as the grade beam. To account for the possible flexural failure of piles, the distributed plastic hinge method [24] is adopted. Multiple plastic hinges are inserted along the expected plastic zone of a structural member, because the location of maximum moment along a laterally loaded pile may vary as the nonlinearity of surrounding soil develops. The locations of hinges herein are from the pile head to a depth of 13 m (that is, 1 m below the interface of sand and sandy silt layers), as the green solid circles are shown in Figure 4, and thus, the interface of liquefied and lower nonliquefied layers (at the depth of 9 m) is also covered. Thus, the nonlinear behavior of the pile-soil system can be approximated at an acceptable analysis cost, and the performance of the pile can be assessed according to the damage state judged by the development of plastic hinges.

4.2.2. p-y Curves.

In this study, the suggestions of Railway Technical Research Institute, Japan (RTRI) [25] for determining the subgrade reaction coefficient (k_h) for short-term loading as well as the upper bound of the soil reaction to the pile (p_e) were adopted to obtain the p-y curves for defin-

ing soil springs:

$$k_h = \frac{7200(\text{SPT} - \text{N})}{\gamma_{gE}} D^{-3/4}, \tag{5}$$

$$p_e(z) = 3.0(\overline{\gamma_e}z) \tan^2\left(45° + \frac{\phi}{2}\right), \tag{6}$$

where D denotes the pile diameter; γ_{gE} is the coefficient for subsurface investigation, and a value of 1.3 was used; z is the concerned depth from the ground surface; and $\overline{\gamma_e}$ and ϕ are the average unit weight and the representative friction angle of soil at the depth z.

Because only SPT-N values were available in [16], ϕ was estimated using the following equation (4):

$$\phi = 4.8 \ln N_1 + 21, \tag{7}$$

where N_1 is the corrected SPT-N to an effective overburden stress of 100 kPa.

Equations (5) and (6) give a bilinear elastic-plastic p-y relationship as shown in Figure 5, which needs only two parameters to define and is easy to use in engineering practice. Regarding the model in Figure 4(a) (lateral spreading as flow displacement), both k_h and p_e in the liquefied layer were reduced by multiplying D_E listed in Table 2 to consider the soil degradation due to liquefaction, and it is noted that k_h and p_e were reduced to zero at depths of 3~4 m.

4.2.3. Cross-Section and Plastic Hinge Properties of the Piles.

The building for case study used Classification A PC piles with a length of 20 m, an outer diameter of 400 mm, and a wall thickness of 65 mm, and their design compressive axial load was 40 tons [16]. The Young modulus $E = 34.3$ GPa and the moment of inertia $I = 0.001025$ m^4 of the pile cross-section were specified based on [23]. The properties of plastic hinges on piles were defined moment-curvature (M-ϕ) curves as shown in Figure 6, where M_{cr}, M_y, M_u, and M_{res} denote the cracking moment, yielding moment, ultimate moment, and residual moment of the cross-section of the pile. It should be mentioned that the influence of axial load variation on the properties of the pile cross-section, such as the axial load-bending moment (P-M) interaction, was not included since the comparison of the cases with and without axial load from the superstructure in this study which will be presented later emphasized on the P-delta effect. Considering a Classification A PC pile under a design compressive axial load of 40 tons for simplification [16], it was obtained based on JIS A 5373 [26] that $M_{cr} = 83.3$ kN-m and $M_u = 136.8$ kN-m. In practice, M_y is usually regarded as 0.85-0.95 times of M_u [27–29], and $M_y = 0.9M_u$ was adopted. After cracking, section rigidity of the pile (that is, slope of M-ϕ curve, EI) was reduced to 1/5 of its initial value [23], which was widely adopted in engineering practice. After yielding, a curvature ductility ratio ($\mu_\phi = \phi_u/\phi_y$) of 20 was achieved as the M_u was reached, which gave a section rigidity reduced to 1/400 of its initial value. It is noted that $\mu_\phi = 20$ was based on an allowable displacement ductility ratio (μ) of 4 at pile head

(a)

(b)

(c)
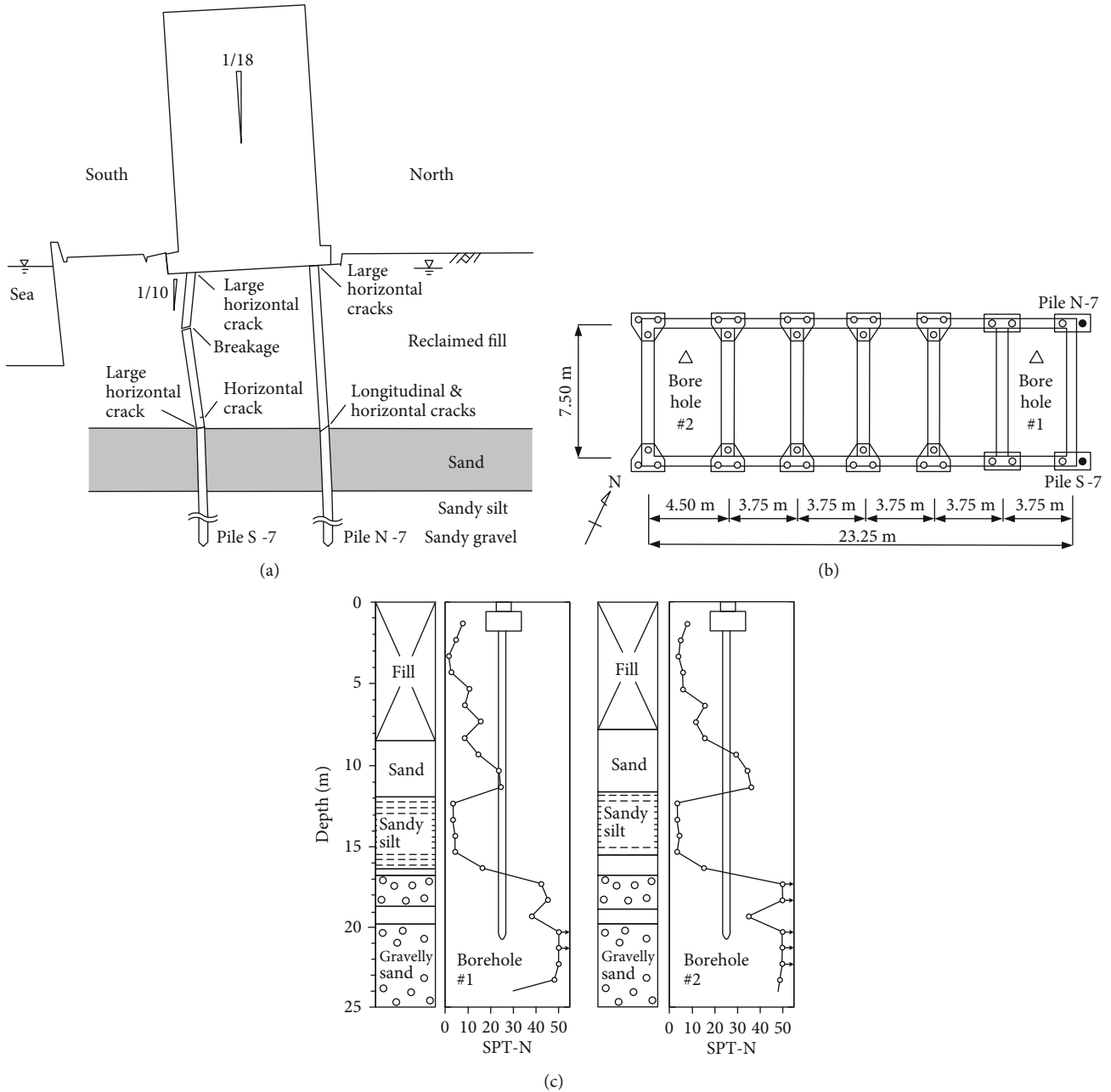
Figure 3: A building near waterfront suffered pile damage during the 1995 Kobe Earthquake. (a) Tilt of the building and damages along piles. (b) Foundation layout. (c) Boring log of the site. (After [16]).

for vertical piles suggested in [4] with the usage of the following equation [30]:

$$\mu_\phi = 1 + \frac{\mu - 1}{3\left(L_p/L\right)\left[1 - 0.5\left(L_p/L\right)\right]}, \qquad (8)$$

where L is the pile length; L_p denotes the plastic hinge length and is defined as the spacing between hinges in the distributed plastic hinge method [24].

After reaching M_u, the flexural strength of the pile significantly degraded until a residual moment of $M_{res} = 0.2M_u$ was attained according to FEMA 356 [31] if the pile was

regarded as a beam or a column, and this was considered the final state that a complete flexural failure of the pile had occurred.

The mentioned main analysis parameters for the piles are listed in Table 3.

It is noted that the procedure to determine the moment-curvature relationship in this study needs no section analysis and is thus easy for application in engineering practice.

4.2.4. Actions of Lateral Spreading. Concerning the model in Figure 4(a), the flow displacement was assigned using the simplified approximation in [18] mentioned in Section 3.1. Although field observation gave a value up to 1.0 m at Pile

TABLE 2: Liquefaction potential assessment of the site of case study.

Depth (m)	Soil type	FC (%)	SPT-N	N_1	F_L	D_E
1.00	Fill	10.0	8	17.9	2.15	—
2.00	Fill	10.0	4	6.3	0.82	0.2
3.00	Fill	10.0	1	1.4	0.53	0
4.00	Fill	10.0	2	2.6	0.53	0
5.00	Fill	10.0	10	11.9	0.82	0.2
6.00	Fill	10.0	9	10.1	0.71	0.1
7.00	Fill	10.0	15	15.8	1.14	—
8.00	Fill	10.0	8	8.0	0.61	0.1
9.00	Sand	10.0	14	13.3	0.86	0.2
10.00	Sand	10.0	23	21.0	2.51	—
11.00	Sand	10.0	24	21.0	2.54	—
12.00	Sandy silt	60.0	3	2.6	N.L.	—
13.00	Sandy silt	60.0	3	2.5	N.L.	—
14.00	Sandy silt	60.0	4	3.3	N.L.	—
15.00	Sandy silt	60.0	4	3.2	N.L.	—
16.00	Sandy silt	60.0	16	12.4	N.L.	—
17.00	Gravelly sand	0.0	42	31.7	6.29	—
18.00	Gravelly sand	0.0	46	33.8	9.47	—
19.00	Sand	0.0	38	27.2	2.76	—
20.00	Gravelly sand	0.0	50	34.9	12.0	—

S-7 and around 0.8 m at Pile N-7 [16], these were not free-field displacements but influenced by soil-structure interaction. Therefore, Equation (1) was used to estimate the free-field surface displacement at the piles locations, in which $D_0 = 1.6$ m was specified according to [16], and $L_{ls} = 50D_0 = 80$ m was adopted. It gave a value of 1.23 m at Pile S-7 and 0.88 m at Pile N-7. Then, Equation (2) was utilized for the ground displacement profile, in which $z_w = 2$ m and $H_L = 7$ m were specified based on the liquefaction potential assessment in Section 4.1.

As for the model in Figure 4(b), flow pressure was assigned using Equations (3) and (4), in which $H_{NL} = 2$ m and $H_L = 7$ m were specified. It is noted that, although the flow pressure is dependent on the distance to the waterfront via the coefficient c_s, its values for Pile S-7 and Pile N-7 were the same because the distance were both smaller than 50 m. As the thickness of the nonliquefied crust and liquefied layers was also the same, the obtained pressure profile on both piles was identical.

It is noted that the displacement-control procedure in SAP2000 was adopted when the lateral spreading was modelled as both flow displacement and flow pressure, not only because it has generally better convergence for nonlinear analysis but also because it enables the analysis on structures with a negative stiffness, which is possible herein when the plastic hinge on piles has reached its ultimate moment.

4.3. Analysis Results: Lateral Spreading as Flow Displacement

4.3.1. No Axial Load from Superstructure. Firstly, only the actions of the lateral spreading were considered in terms of

flow displacement, and the axial load from the superstructure was neglected. Figure 7 shows the obtained pile deformation, the development of plastic hinges, and the moment distribution along the piles at different structural limit states, of which the yielding state means that the first plastic hinge reached its yielding moment (M_y) so that a significant stiffness reduction of the pile was caused, ultimate state means that the first plastic hinge reached its ultimate moment (M_u) so that the ultimate bending resistance of the pile was attained, and the final state means that the first plastic hinge reached its residual moment (M_{res}) so that a complete flexural failure of the pile was considered having occurred. These mentioned moments are defined in Figure 6.

As 7.0% of the prescribed flow displacement was applied, the yielding state was reached though the pile cap displacement was merely slightly above 0.07 m. Plastic hinges beyond cracking on Pile S-7 showed at the depth of 4-6 m (refer to Table 2, near the border between soil springs with $D_E = 0$ and $D_E > 0$) as well as near the interface of liquefied and lower nonliquefied layers, where the first yielding hinge appeared (at a depth of 9 m), while those on Pile N-7 were mainly near the pile head. When 66.1% of the prescribed flow displacement was applied, the pile cap displacement was about 0.7 m, and the ultimate state was reached because the first hinge attained its M_u on Pile S-7 at a depth of 9 m, and the majority of the plastic hinges in the liquefied layer on both piles had yielded. As all the prescribed flow displacement was eventually imposed to the piles, the displacement at the pile cap was 1.08 m, conforming to the field observations, and the moment resistance in the plastic hinge on Pile S-7 at a depth of 9 m had descended to M_{res}, indicating that the final state had been reached; meanwhile, the hinge on Pile N-7 at the depth of 9 m had attained its M_u.

Naturally, the locations of plastic hinges can be related to the extrema of the moment distribution curves shown in Figure 7; moreover, a double-curvature behavior of both piles is noticed by the sign change of the bending moment except for Pile N-7 at the final state because the hinge reaching M_{res} served as a fuse to prevent the downward transmission of the moment. This double curvature is probably due to the restraints from the pile cap and the grade beam at the upper ends of the piles as well as from the soil reaction of the lower nonliquefied layer.

Excluding the plastic hinges at the interface of liquefied and lower nonliquefied layers, the distribution of hinges, though mainly in the liquefied layer, was somewhat different on Pile S-7 and Pile N-7. For the former, plastic hinges with a worse damage state concentrated in the middle of the pile sector in the liquefied layer, while those for the latter were closer to the upper and lower ends. This difference can be attributed to the discrepancy in moment distribution. Anyhow, development of plastic hinges roughly meets the real situation in which piles were more severely damage near the pile head as well as near the border between reclaimed fill and sand (namely, between liquefied and lower nonliquefied layers), as shown in Figure 3(a). However, it is also noted the breakage of Pile S-7 at a depth of 4.5 m was not reproduced in the analysis, even though a considerable pile sector around
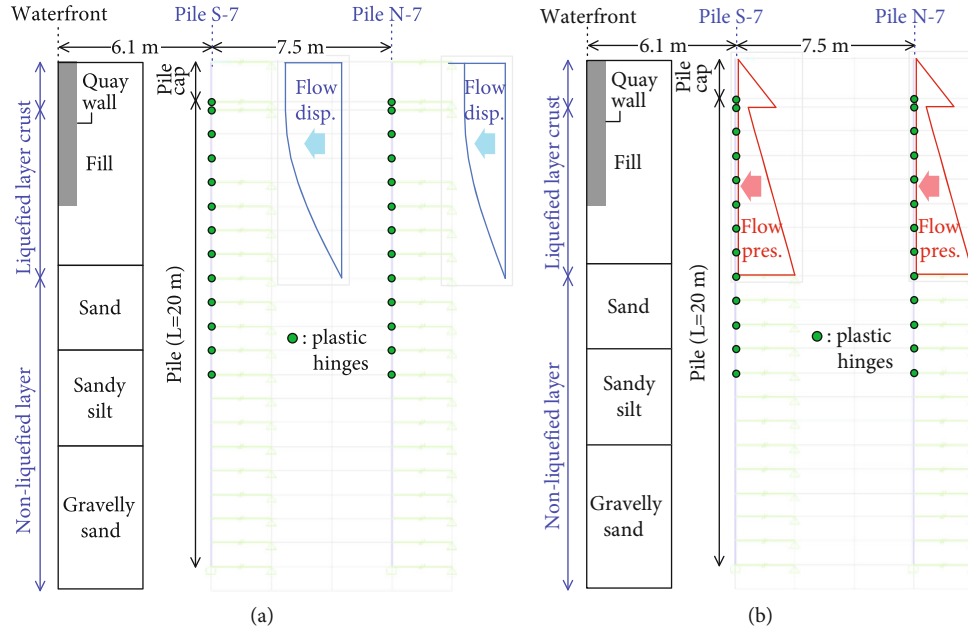
FIGURE 4: SAP2000 model for case study. (a) Lateral spreading as flow displacement. (b) Lateral spreading as flow pressure.
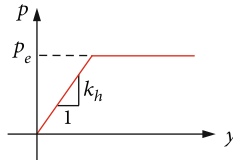

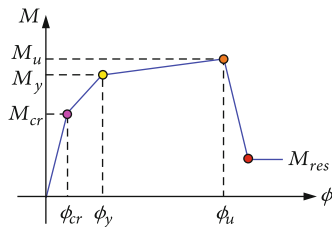FIGURE 5: Bilinear elastic-plastic p-y curve.

FIGURE 6: Moment-curvature curve to define plastic hinges on piles (not to scale).

this depth had reached yielding. This will be further discussed in the next section.

4.3.2. With Axial Load from Superstructure. As mentioned in Section 4.2.3, the design compressive axial load of the pile in this case was 40 tons. Therefore, in this case, the 40-ton axial load was further applied as concentrated load before the action of lateral spreading and remained constant during the analysis to investigate its influence on the pile performance. The axial load on each pile would vary in reality as the structure was subjected to different levels of lateral actions due to the restraint of grade beams and pile caps. However, including axial load variation would make the analysis rather complicated because it could be necessary to model the superstructure, and in addition, the P-delta effect

could not be conspicuously exhibited. Therefore, a constant compressive axial load was adopted for both simplification and better demonstration. Figure 8 depicts the pile deformation, the development of plastic hinges, and the moment distribution along the piles.

The yielding state was reached as 6.6% of the prescribed flow displacement was applied, and the pile cap displacement as well as the distribution of plastic hinges were similar to the no-axial-load case. The ultimate state was reached when 65.2% of the prescribed flow displacement was applied, and the first hinge attained its M_u on Pile S-7 also at a depth of 9 m, yet meanwhile, the pile cap displacement was nearly 0.8 m, larger than the no-axial-load case. It is also noticed that more plastic hinges on Pile S-7 in the liquefied layer had yielded but less on Pile N-7. The final state had been reached when all the prescribed flow displacement was imposed to the piles because the plastic hinge on Pile S-7 at a depth of 9 m had attained its M_{res}, same as the no-axial-load case, and meantime, the hinge on Pile N-7 at the depth of 9 m had also attained its M_u. However, the displacement at the pile cap was up to 1.22 m, larger than the no-axial-load case.

The discrepancy between the analyses with and without the axial load is probably due to the additional moment from the axial load as the pile head was laterally displaced, or the P-delta effect. This additional moment is responsible for greater displacement of the pile cap, the slightly earlier reaching of the yielding and ultimate states, and the larger yielding zone of Pile S-7 in the liquefied layer. Although the breakage of Pile S-7 at a depth of 4.5 m was still not reproduced, the P-delta effect did cause the more extensive damage of Pile S-7. Further considering the total loss of soil resistance ($D_E = 0$) near this depth due to severe liquefaction that can be regarded as the absence of lateral confinement of the pile,

TABLE 3: Main analysis parameters for piles.

Cross-section properties				
Length	Outer diameter	Thickness	Young's modulus, E	Moment of inertia, I
20 m	400 mm	65 mm	34.3 GPa	0.001025 m^4
Plastic hinge properties				
Cracking moment, M_{cr}	Yielding moment, M_y	Ultimate moment, M_u	Residual moment, M_{res}	Curvature ductility ratio, μ_ϕ
83.3 kN-m	123.1 kN-m	136.8 kN-m	27.4 kN-m	20

the buckling instability of Pile S-7 might be induced. Unfortunately, it could not be represented by the displacement-based approach despite the P-delta effect had been included in the analysis.

It should be mentioned that the two piles were possibly subjected to different axial loads in reality, which might influence their damage patterns. Although the analysis model can account for this possibility, yet for this case, the design axial load was adopted because the purpose was to exhibit the effect of the axial load. Consequently, discrepancy between the damage patterns from the analysis and of the reality could be thus caused.

4.4. Analysis Results: Lateral Spreading as Flow Pressure

4.4.1. No Axial Load from Superstructure. Similarly, the axial load from the superstructure was firstly neglected, and only the actions of the lateral spreading were considered in terms of flow pressure. The pile deformation, the development of plastic hinges, and the moment distribution along the piles at different structural limit states are given in Figure 9.

The yielding state was reached with the appearance of yielding hinges on both Pile S-7 and Pile N-7 at a depth of 9 m, the interface of liquefied and lower nonliquefied layers, until 61% of the prescribed flow pressure was applied, yet meantime, the pile cap displacement was merely 0.087 m. In addition, development of plastic hinges on both piles were the same, beyond cracking near the pile head as well as near the depth of 9 m, which can be related the almost identical moment distribution on both piles which showed a double curvature with the moment extrema at the pile head and at a depth of 9 m. The identical moment distribution was due to the same pressure profile acting on both piles as well as the symmetric structure. As 73% of the prescribed flow pressure was imposed, the pile cap displacement was about 1.17 m, and on both piles, the hinges at a depth of 9 m firstly attained their M_u, showing that the ultimate state was reached; meanwhile, both piles yielded near the pile head. After this, no additional flow pressure could be applied, probably because the moment-curvature relationship of the hinges having reached their M_u showed a negative slope, as shown in Figure 6; that is, the moment resistance was descending. Further examining the base shear of the model versus the pile cap displacement, as shown in Figure 10, a negative slope of the curve that represented the negative stiffness of the foundation system exhibited after its ultimate state, indicating that the system was unstable. Thus, the final

state defined as one of the hinges reached its M_{res} was not available.

In this case, damage near the pile head and the interface between reclaimed fill and sand can be approximated, but the breakage of Pile S-7 at a depth of 4.5 m was still not reproduced. In addition, as mentioned, the damage pattern of Pile S-7 and Pile N-7 were identical in the analysis, yet this is not conformable to the real situation that some difference existed.

4.4.2. With Axial Load from Superstructure. When the design compressive axial load of 40 tons was included, the yielding state was reached as 52% of the prescribed flow pressure was applied, and the yielding hinges also appeared on both Pile S-7 and Pile N-7 at a depth of 9 m, as shown in Figure 11. Although at this moment the pile cap displacement was only 0.125 m, no additional flow pressure could be applied afterwards. The base shear of the model versus the pile cap displacement of this case, as shown in Figure 10, exhibited greater discrepancy from the no-axial-load case as the pile cap displacement increased, and consequently, a negative stiffness of the foundation system was shown after its yielding state; that is, the foundation system was unstable, and thus, the ultimate and final states were both not available. Since the moment-curvature relationship of the plastic hinges in Figure 6 exhibits a hardening tendency after yielding, this negative stiffness can be attributed to the P-delta effect shown with the inclusion of the compressive axial load, which is often considered equivalent to reduction of flexural rigidity of a structural member, and can be regarded as the occurrence of buckling. P-delta effect was also responsible for the less applied flow pressure and larger pile cap displacement at yielding than in the no-axial-load case.

The damage pattern of the piles shown in Figure 11 is similar to in Figure 9(a), the no-axial-load case. Despite the breakage of Pile S-7 at a depth of 4.5 m was also not directly reproduced in the analysis, the negative stiffness of the foundation system owing to the P-delta effect occurred before its ultimate state implied that the buckling instability might control the failure of the piles, which was considered possible for slender piles, especially for those embedded in liquefied ground. That is, the complete damage of Pile S-7 at a depth of 4.5 m was probably related to the buckling of the pile sector in the liquefied layer.

4.5. Comparison and Discussions. Some differences are noticed in the results of the displacement-based and force-
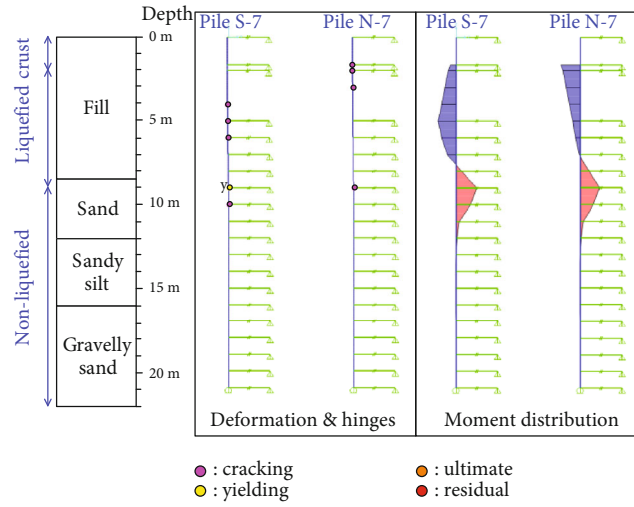
(a)
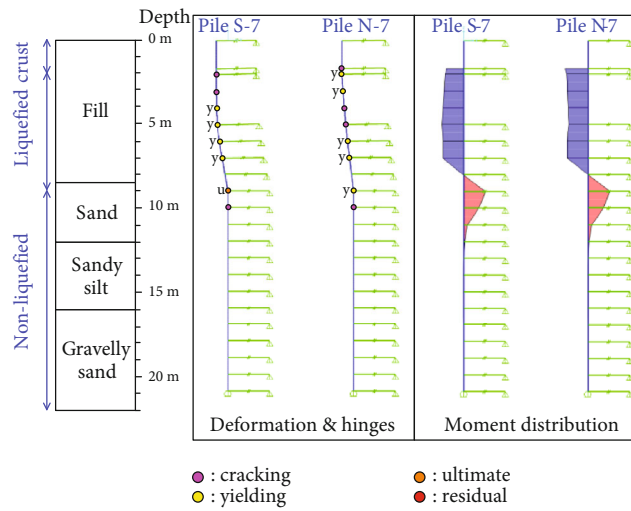
(b)
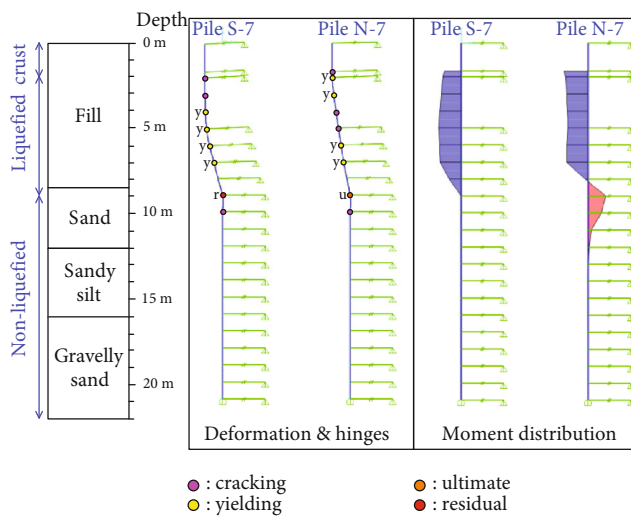
(c)

FIGURE 7: Deformation, plastic hinges, and moment distribution along the piles (lateral spreading as flow displacement, no axial load). (a) Yielding state. (b) Ultimate state. (c) Final state.

(a)

(b)

(c)

FIGURE 8: Deformation, plastic hinges, and moment distribution along the piles (lateral spreading as flow displacement, with axial load). (a) Yielding state. (b) Ultimate state. (c) Final state.

(a)

(b)

FIGURE 9: Deformation, plastic hinges, and moment distribution along the piles (lateral spreading as flow pressure, no axial load). (a) Yielding state. (b) Ultimate state. (Final state not available).

based approaches. The most obvious one is that the prescribed actions of lateral spreading could not be entirely applied in the latter, because the foundation system had a negative stiffness and was thus unstable after a certain damage state, while using the former enabled the complete imposition of the action. Additionally, the pile cap displacement obtained using the force-based approach was more conservative (larger) either in the yielding state or in the ultimate state, while that obtained using displacement-based approach when all the prescribed flow displacement had been applied was close to field observations.

The flow pressure profile proposed in [4] is basically corresponding to a limit state in which the passive earth pressure is developed in the nonliquefied crust layer. However, based on the comparison of the simplified analysis [2] and the centrifuge test results [5], modelling lateral spreading as flow pressure could be overpredicted the bending moments in the pile if the ground movements were not large enough to mobilize the presumed limit pressures. In other words, the assigned flow pressure, especially that in the nonliquefied crust layer, could be overestimated and thus more conservative compared to the real situation.

Another discrepancy is the moment distribution of the piles, which was very similar in both piles when the force-based approach was used, thus leading to identical damage pattern. On the other hand, using the displacement-based

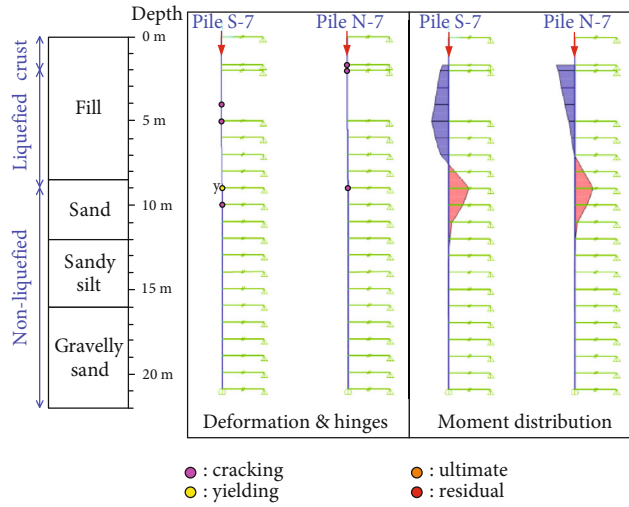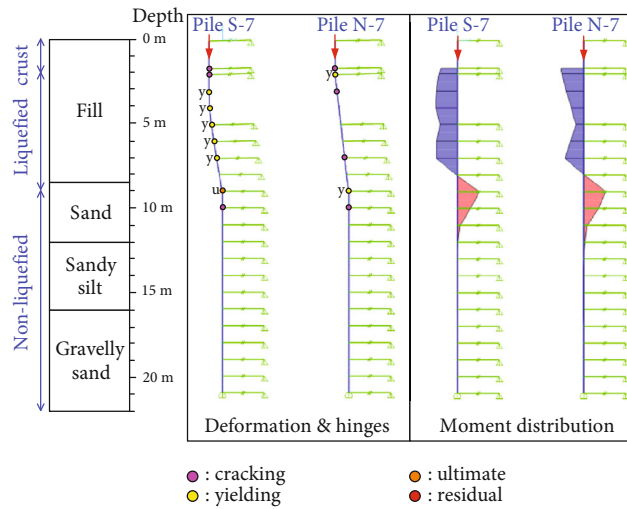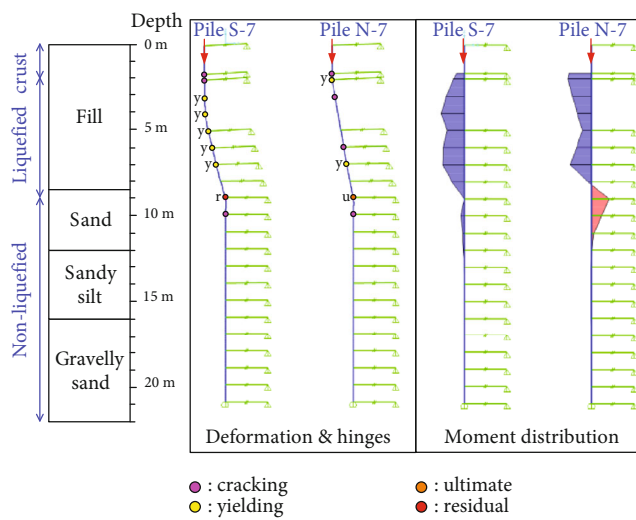Figure 10: Base shear versus pile cap displacement (lateral spreading as flow pressure).
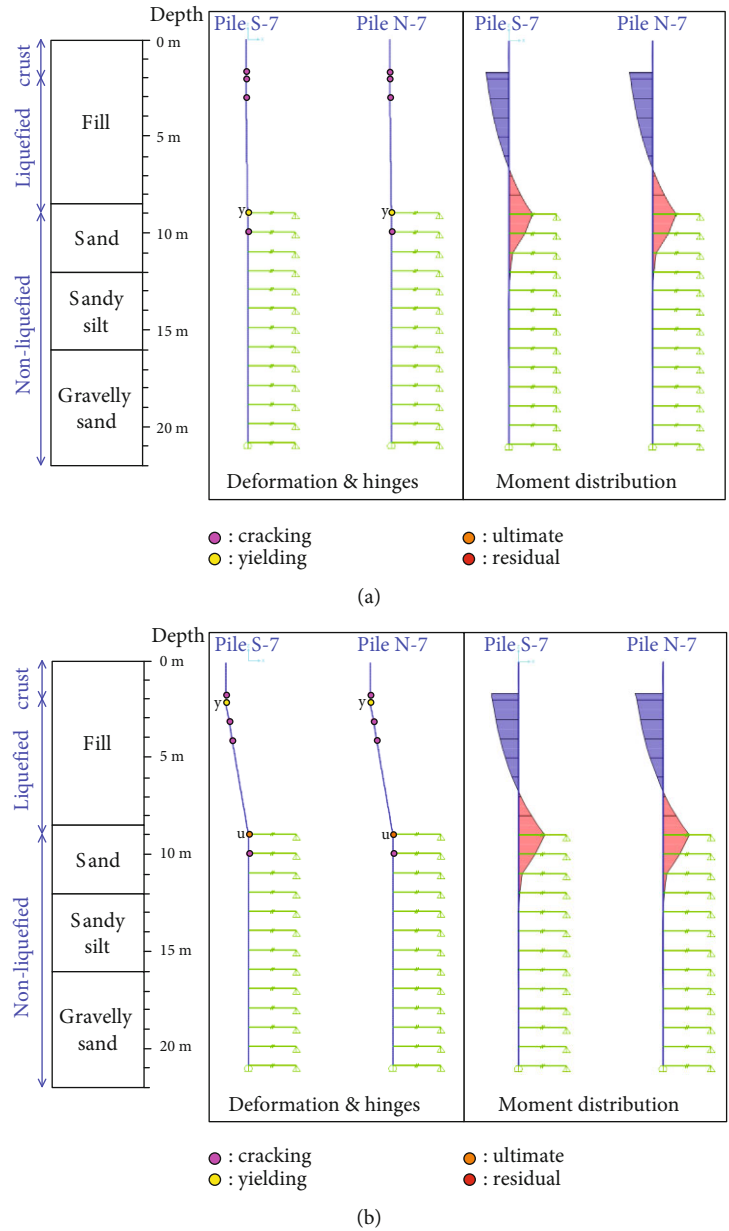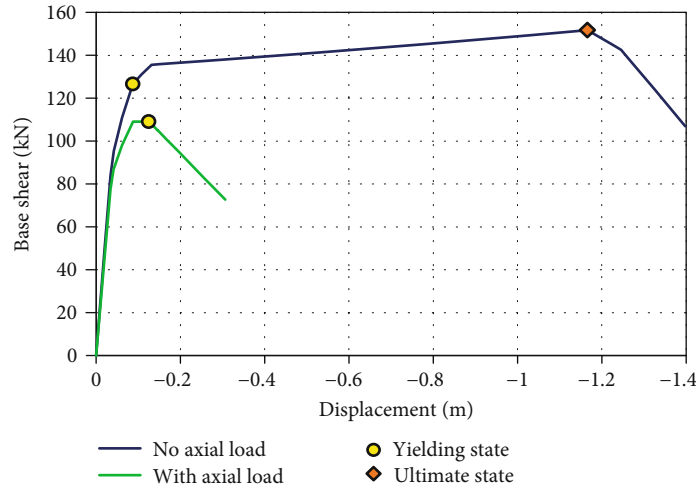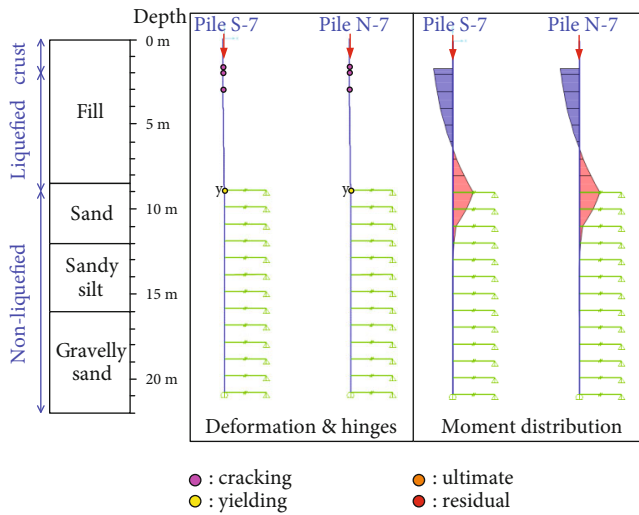

Figure 11: Deformation, plastic hinges, and moment distribution along the piles (lateral spreading as flow pressure, with axial load) at yielding state (ultimate and final states not available).

approach gave different moment distribution in the piles, and consequently, Pile S-7 was more severely damaged, which was conformable to the real situation. The reason could be that the adopted method to estimate flow pressure [4] in the force-based approach only roughly takes the distance from the waterfront into consideration via the factor c_s, and in this case, the same c_s was specified for both piles so that identical flow pressure was assigned; while in the displacement-based approach, different flow displacement profile was estimated according to [18] for each pile, because different ground surface displacement was specified considering its distance from the waterfront.

To further clarify the action of lateral spreading in both approaches, though the displacement-based one is basically forced displacement analysis and thus the lateral spreading pressure cannot be directly obtained, the lateral reaction of each soil spring as all the prescribed displacement profile had been imposed was used to calculate the apparent-pressure diagram along both piles, which was from the idea from the braced cut analysis. It was then compared to the flow pressure profile used in the force-based approach, as shown in Figure 12, where positive values denote pressure from the north (landside) whereas negative values denote pressure from the south (seaside) (refer to Figure 3(a)). Large discrepancy was noticed, because the apparent pressure varied intensely with respect to the depth and did not drop to zero below the liquefied layers. However, it should be emphasized that this apparent pressure distribution were in fact the consequence of the pile-soil interaction and could be significantly influenced by the structural characteristics of the piles, such as the rigid body constraint specified to both pile caps which made this interaction more complicated. On the other hand, the flow pressure profile was based on limit state of soil [4] and was irrelevant to the structure. It could be roughly regarded as the lateral spreading pressure acting on a rigid structure if the ground movements were large enough for limit pressure mobilization, yet this also means the pile-soil interaction was excluded.

To conclude, the flow displacement seems to better approximate the actions of liquefaction-induced lateral spreading in this case. Nevertheless, the displacement-based method, which basically performs the analysis by imposing given displacement profile as boundary conditions without actually applying lateral spreading pressure, cannot explicitly exhibit the instability due to either the strength descending of structure members or the geometric nonlinearity, because no base shear can be directly output by the SAP2000 software during the analysis. By contrast, the instability can be represented by the force-based method in terms of the negative stiffness of the foundation system, namely, the negative slope of the curve showing base shear versus pile cap displacement. If the flow pressure can be adjusted to consider the level of limit pressure mobilization and the distance from the waterfront more specifically, as well as to include the influences of the
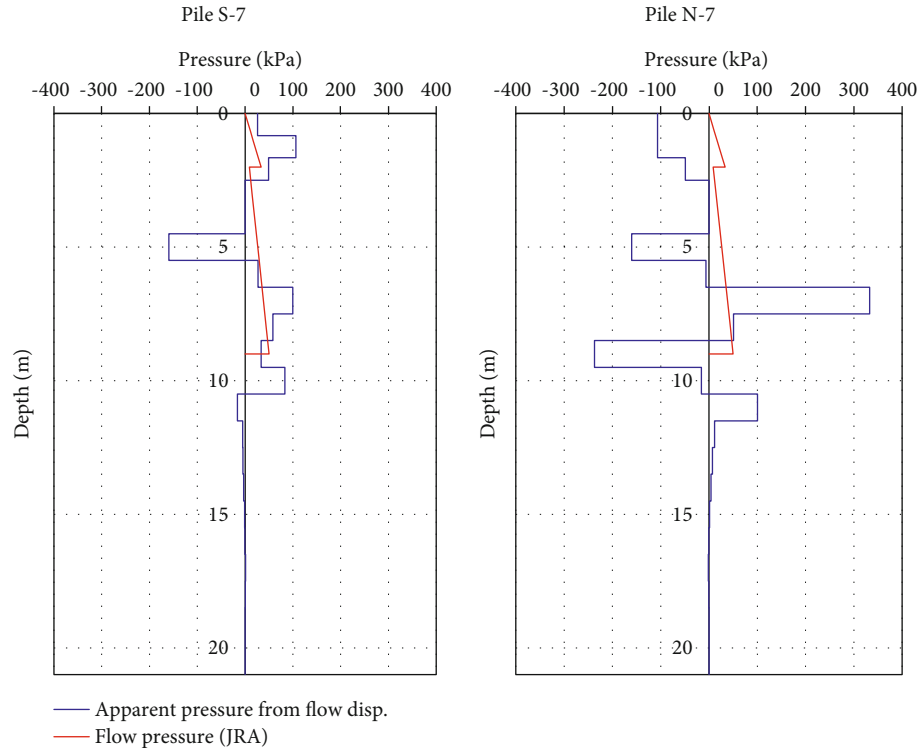
Figure 12: Comparison of apparent-pressure diagram from the displacement-based approach and the flow pressure used in the force-based approach.

soil-structure interaction on the actions of lateral spreading, the force-based method can be expected to capture main damage patterns of piles subjected to lateral spreading and can thus reasonably assess their performance.

5. Applicability and Limitations

The proposed analysis model basically utilizing the concept of the Winkler foundation, which only needs beam-column (frame) and spring elements. The soil nonlinearity is represented by nonlinear p-y curves, and the possible flexural failure (or even shear failure) of piles is simulated by plastic hinges. Therefore, the model can be established by any of the recognized structural analysis codes as long as it allows of defining nonlinear force-displacement relationship of the spring elements and provides plastic hinges, which makes this model quite applicable in engineering practice.

However, an apparent limitation of the model noticed in the analysis results is that it failed to specifically reproduce the buckling-induced damage of the pile. Although the model was able to account for P-delta effect when axial load on the pile was included, it could only simulate the consequently caused additional moment when the laterally spreading ground was modelled as flow displacement but the instability due to the nature of displacement-based approach. To be more specific, the approach comprised forced displacement analysis which was made with given displacement boundary conditions, and thus, an equilibrium solution could always be obtained at a prescribed flow displacement

profile as long as the strength of the pile-soil system was still enough to resist the action of the axial load. Therefore, it cannot highlight the possible structural instability under the combination of lateral spreading and axial load. On the other hand, the force-based approach could exhibit the instability in terms of negative stiffness of the pile-soil system after its yielding but before ultimate states when axial load was considered. However, it also means no additional flow pressure could be applied at this moment, because the analysis scheme needed to achieve an equilibrium, and thus, the sequential structural failure was not reproduced. To this end, an explicit scheme allowing for the simulation of failure or even collapse process of structures may be necessary.

Nevertheless, revealing the possibility of geometrical instability, which the proposed model is capable of, is still beneficial in engineering practice. Thus, this model can be considered competent for the need of performance assessment. For instance, if negative stiffness of the pile-soil system, either caused by the strength degradation of the pile-soil system or by geometric nonlinearity, is exhibited using the force-based model, the performance of the piles can be regarded as nearly collapse.

Another limitation for the force-based approach, though it is preferable considering the buckling of piles, is the modelling of flow pressure. According to the results of case study, it gave larger displacement and failed to approximate the damage pattern, and the reason could be that the flow pressure profile proposed by JRA [4] was not sufficiently adequate. This is an important issue to be investigated in the future.

6. Conclusions

In this study, the response of piles subjected to lateral spreading of liquefied ground was evaluated using nonlinear pseudo-static analysis, and a pile damage case during the 1995 Kobe Earthquake was adopted for case study. The actions of laterally spreading ground were modelled as both flow displacement and flow pressure, and the results were compared and discussed. Several conclusions can be drawn as follows:

(1) By the usage of the Winkler foundation with soil springs represented by elastic-plastic p-y curves to account for the pile-soil interaction, and the distributed plastic hinges on the pile to simulate its flexural failure, as well as the inclusion of P-delta effect, the nonlinear behavior, and the damage pattern of laterally loaded piles can be reasonably approximated at an acceptable cost for engineering practice purpose. Thus, the performance of piles can be assessed according to the status of the plastic hinges and the stability of the analysis model

(2) The displacement-based approach with the flow displacement estimated following Tokimatsu and Asaka [18] gave a damage pattern in which considerable damages were caused to both piles near the pile head and the interface between the liquefied and lower nonliquefied layers, and the latter was the most severe, while Pile S-7 was also severely damaged in the middle of its sector in the liquefied layers. This is roughly conformable to the reality except the pile breakage at a depth of 4.5 m was not successfully reproduced. In addition, the obtained pile cap displacement was also close to the field observations. By contrast, the force-based approach with the flow pressure profile proposed by JRA [4] gave somewhat different damage pattern and more conservative pile cap displacement compared to the displace-based approach

(3) Including the compressive axial load of piles caused the same damage state to be reached at a lower magnitude of applied actions and larger corresponding pile cap displacement, that is, it intensified the flexural damage of laterally loaded pile. This can be owing to the additional moment from the P-delta effect. Hence, the axial load should be considered in evaluating the lateral resistance of piles

(4) Despite of the somewhat different results compared to the real case, the force-based method can account for the structural instability of the pile due to either strength descending of plastic hinges or the geometric nonlinearity in terms of the negative stiffness of the foundation system, which helps to capture the dominant failure mode of the pile in assessing its performance. Accordingly, buckling failure was possible for the pile in the investigated case when the compressive axial load was included, because the global

instability occurred before the ultimate moment of any of the plastic hinges was reached. By contrast, the displacement-based method cannot highlight this instability, because an equilibrium solution can always be obtained at the prescribed flow displacement as long as the structure is still adequate to resist the axial load

Data Availability

The data used to support the findings of this study are included within this article.

Conflicts of Interest

The authors declare that they have no conflict of interest regarding the publication of this article.

Acknowledgments

References

[1] S. Bhattacharya and K. Tokimatsu, "Collapse of Showa Bridge revisited," *International Journal of Geoengineering Case Histories*, vol. 3, no. 1, pp. 24–35, 2013.

[2] S. J. Brandenberg, R. W. Boulanger, B. L. Kutter, and D. Chang, "Static pushover analyses of pile groups in liquefied and laterally spreading ground in centrifuge tests," *Journal of Geotechnical and Geoenvironmental Engineering*, vol. 133, no. 9, pp. 1055–1066, 2007.

[3] S. A. Ashford, R. W. Boulanger, and S. J. Brandenberg, *Recommended Design Practice for Pile Foundations in Laterally Spreading Ground*, PEER, Berkeley, CA, 2011.

[4] Japan Road Association (JRA), *Specifications for Highway Bridges*, Part V – Seismic Design, Japan Road Association, Tokyo, Japan, 2012, (in Japanese).

[5] A. F. Rauch, *EPOLLS: An Empirical Method for Predicting Surface Displacements Due to Liquefaction– Induced Lateral Spreading in Earthquakes, Ph.D. dissertation*, Virginia Polytechnic Institute and State University, VA, 1997.

[6] T. L. Youd, "Liquefaction-induced lateral ground displacement," in *Proceedings of 3rd International Conference on Recent Advances in Geotechnical Earthquake Engineering and Soil Dynamics*, vol. 2, pp. 911–925, St. Louis, MS, USA, April 1995.

[7] K. Tokimatsu, H. Mizuno, and M. Kakurai, "Building damage associated with geotechnical problems," *Soils and Foundations*, vol. 36, pp. 219–234, 1996.

[8] M. Cubrinovski and K. Ishihara, "Simplified method for analysis of piles undergoing lateral spreading in liquefied soils," *Soils and Foundations*, vol. 44, no. 5, pp. 119–133, 2004.

[9] S. J. Brandenberg, R. W. Boulanger, B. L. Kutter, and D. Chang, "Behavior of pile foundations in laterally spreading ground during centrifuge tests," *Journal of Geotechnical and Geoenviromental Engineering*, vol. 131, no. 11, pp. 1378–1391, 2005.

[10] S. M. Haeri, A. Kavand, I. Rahmani, and H. Torabi, "Response of a group of piles to liquefaction–induced lateral spreading by large scale shake table testing," *Soil Dynamics and Earthquake Engineering*, vol. 38, pp. 25–45, 2012.

[11] R. Motamed, I. Towhata, T. Honda, K. Tabata, and A. Abe, "Pile group response to liquefaction–induced lateral spreading: E–Defense large shake table test," *Soil Dynamics and Earthquake Engineering*, vol. 51, pp. 36–46, 2013.

[12] R. Dobry, T. Abdoun, T. D. O'Rourke, and S. H. Goh, "Single piles in lateral spreads: field bending moment evaluation," *Journal of Geotechnical and Geoenvironmental Engineering*, vol. 129, no. 10, pp. 879–889, 2003.

[13] National Institute of Standards and Technology (NIST), *The January 17, 1995 Hyogoken–Nanbu (Kobe) Earthquake – Performance of Structures, Lifelines, and Fire Protection Systems, NIST Special Publication 901, Building and Fire Research Laboratory*, National Institute of Standards and Technology, Gaithersburg, MD, 1996.

[14] PIANC (World Association for Waterborne Transport Infrastructure), *Seismic Design Guidelines for Port Structures*, A.A. Balkema Publishers, Lisse, Netherlands, 2001.

[15] K. Ishihara and M. Cubrinovski, "Case studies of pile foundations undergoing lateral spreading in liquefied deposits," in *5th International Conference on Case Histories in Geotechnical Engineering*, New York, NY, USA, April 2004.

[16] K. Tokimatsu, H. Oh-oka, K. Satake, Y. Shamoto, and Y. Asaka, "Failure and deformation modes of piles due to liquefaction-induced lateral spreading in 1995 Hyogoken–Nambu earthquake," *Journal of Structural and Construction Engineering, AIJ*, vol. 62, no. 495, pp. 95–100, 1997, (in Japanese).

[17] M. Cubrinovski, J. D. Bray, C. de la Torre et al., "Liquefaction effects and associated damages observed at the Wellington Centreport from the 2016 Kaikoura earthquake," *Bulletin of the New Zealand Society for Earthquake Engineering*, vol. 50, no. 2, pp. 152–173, 2017.

[18] K. Tokimatsu and Y. Asaka, "Effects of liquefaction–induced ground displacements on pile performance in the 1995 Hyogo-ken–Nambu earthquake," *Soil and Foundations*, vol. 38, pp. 163–177, 1998.

[19] T. Iwasaki, T. Arakawa, K. Tokida, and S. Yasuda, "A practical method for assessing soil liquefaction potential based on case studies at various sites in Japan," in *Proceedings of 2nd International Conference on Microzonation for Safer Construction - Research and Application*, vol. 2, pp. 885–896, San Francisco, CA, USA, November-December 1978.

[20] AIJ (Architectural Institute of Japan), *Recommendations for Design of Building Foundations*, Architectural Institute of Japan, Tokyo, Japan, 2001, (in Japanese).

[21] J. H. Huang and C. H. Chen, "Evolution of design guidelines on soil liquefaction assessment," *Sino-Geotechnics*, vol. 70, pp. 23–44, 1998, (in Chinese).

[22] CSI (Computers & Structures, Inc), *CSI Analysis Reference Manual for SAP2000 Ver. 20*, Walnut Creek, CA, 2017.

[23] R. Uzuoka, N. Sento, A. Yashima, and F. Zhang, "3–dimensional effective stress analysis of a damaged group–pile foundation adjacent to a quay wall," *Journal of JAEE*, vol. 2, no. 2, pp. 1–14, 2002, (in Japanese).

[24] J. S. Chiou, H. H. Yang, and C. H. Chen, "Use of plastic hinge model in nonlinear pushover analysis of a pile," *Journal of Geotechnical and Geoenvironmental Engineering*, vol. 135, no. 9, pp. 1341–1346, 2009.

[25] RTRI (Railway Technical Research Institute), *Design Standards for Railway Structures and Commentary (Substructures)*, Railway Technical Research Institute, Tokyo, Japan, 2012, (in Japanese).

[26] Japanese Standards Association (JSA), *Japanese Industrial Standard JIS A 5373: 2004 – Precast Prestressed Concrete Products*, Japanese Standards Association, Tokyo, Japan, 2004.

[27] H. G. Kwak and S. P. Kim, "Nonlinear analysis of RC beams based on moment–curvature relation," *Computers and Structures*, vol. 80, no. 7–8, pp. 615–628, 2002.

[28] K. Watanabe, Y. Umemura, M. Teshigawara, M. Iiba, and M. Tamura, "A study on seismic response evaluation by monolithic analysis of building and its foundation," in *13th World Conference on Earthquake Engineering (13WCEE)*, Vancouver, B.C., Canada, August 2004.

[29] Z. Guo, *Strength and Constitutive Relationship for Concrete – Mechanism and Application*, China Industrial and Building Press, Beijing, China, 2004, (in Chinese).

[30] T. Paulay and M. J. N. Priestley, *Seismic Design of Reinforced Concrete and Masonry Buildings*, John Wiley & Sons, New York, 1992.

[31] American Society of Civil Engineers (ASCE), *Prestandard and commentary for the seismic rehabilitation of buildings*, Report FEMA 356 Federal Emergency Management Agency, Washington, D.C., USA, 2000.

WILEY | Hindawi

Research Article

Ground Subsidence Triggered by the Overexploitation of Aquifers Affecting Urban Sites: The Case of Athens Coastal Zone along Faliro Bay (Greece)

Agavni Kaitantzian,[1] Constantinos Loupasakis [ID],[1] Ploutarchos Tzampoglou,[2] and Isaak Parcharidis[3]

[1]*Laboratory of Engineering Geology and Hydrogeology, School of Mining and Metallurgical Engineering, National Technical University of Athens, 9, Heroon Polytechniou Str., 157 80 Athens, Greece*
[2]*Department of Civil and Environmental Engineering, School of Engineering, University of Cyprus, 75 Kallipoleos Street, P.O. Box 20537, 1678 Nicosia, Cyprus*
[3]*Department of Geography, Harokopio University of Athens, 70, El. Venizelou Str., 17671 Athens, Greece*

Correspondence should be addressed to Constantinos Loupasakis; cloupasakis@metal.ntua.gr

Land subsidence in the coastal zone of the Neo Faliro, Moschato, and Kallithea municipalities, along the Faliro bay, has been recorded since the mid 1960's. This phenomenon has caused damage to buildings, pavements, and roads. Aiming to identify the main causes of the observed ground deformations, data referring to the geological, geotechnical, and hydrogeological settings of the study area has been evaluated. Subsidence has been quantified by the use of space-born Synthetic Aperture Radar interferometry (InSAR) techniques. SVD (Singular Value Decomposition) and IPTA (Interferometric Point Target Analysis) techniques have been applied for the production of deformation maps, referring to the time period between 2002 and 2010. Furthermore, aiming to extend the study of the phenomenon further to the past, Persistent Scatterer Interferometry (PSI) data for the time period from 1992 to 2001 were also evaluated. Finally, the results of the InSAR analysis have been crosschecked with measurements acquired by a vertical geodetic control network as well as by ground truth data, referring to damage inventory of the site. The current research presents an interesting case study of an urban site affected for a long-lasting period by the activities of a neighboring industrial zone. The development of an extensive depression cone, mainly due to the overexploitation of the aquifers for industrial use, is the main cause of the land subsidence phenomenon, without excluding a component of motion due to the natural compaction of the compressible soil in the area of interest. The complexity of the geological, hydrogeological, and geotechnical conditions and the interaction of the numerous land use activities make this study far more interesting.

1. Introduction

Land subsidence is considered as one of the most frequent geological hazard that usually occurs as a consequence of a number of causes, namely, groundwater overexploitation [1–5], organic soils oxidation [6, 7], and collapse of underground cavities [8–10].

The effects of this geohazard include significant damage to buildings as well as loss of functionality of linear and point infrastructures (pipeline and road network deformations, well-casing failures, and protrusion, etc.) [11, 12].

Detecting, measuring, and monitoring land subsidence is important for urban and infrastructure planning as well as for risk management. Repeat-pass Synthetic Aperture Radar interferometry (InSAR) is a unique tool for large-scale monitoring of surface deformation, at a low cost and great precision [13, 14], and particularly for land subsidence regardless of its cause [15–30].

Numerous studies using InSAR techniques have been conducted in Greece concerning areas affected by land subsidence. Characteristic examples of such areas are Thessaly plain in central Greece [31–34], the wider area close to Kalochori and Sindos villages west of the Thessaloniki plain [35–38], the Anthemountas basin at the east of Thessaloniki [39–42].

The current study focuses on the land subsidence phenomenon occurring at the coastal zone of the N. Faliro, Moschato, and Kallithea municipalities, along the Faliro bay. In this urban area, subsidence has been observed since the mid-60s. Although numerous studies have been conducted by using ground-based techniques, like geodetic surveys [43–47]; up until now, there is not any publication referring to any InSAR analysis results as well as no any publication investigating their causal factors.

The study area is a highly populated urban environment, where the human factor is exposed through this geohazard. The socioeconomic importance of the region is excessive. Several major infrastructure projects have taken place in the study area during the last few decades. Furthermore, the plans for the future development of the region are huge, as the entire sea frond along Faliro bay is considered to be the Greek Riviera. Major residential and commercial constructions combined with marinas are planned to be constructed. The urban expansion and the remaining industrial activities affect the natural evolution of the landscape and the physical processes.

The application of the state of the art technology of Synthetic Aperture Radar (SAR) Interferometry successfully verified the subsidence phenomenon adding new information on its spatial distribution and deformation rates. Land motion mapping data, produced by Singular Value Decomposition (SVD) and Interferometric Point Target Analysis (IPTA), combined with geotechnical characteristics and hydrogeological data are the stepping stone for the development of an efficient management and mitigation of this geohazard.

The objective of the present study is to identify the main causes of the observed ground deformations and to upgrade the existing knowledge for their spatial and temporal patterns by means of advanced DinSAR techniques. To achieve this objective, all parameters affecting the evolution of the land subsidence phenomenon have been evaluated, including geological, geotechnical, hydrogeological, and remote sensing data.

2. The Study Area

The site under investigation is located along the Faliro bay coastal front at the southern part of Athens. In particular, it includes the coastal zone of the Neo Faliro, Moschato, and Kallithea municipalities. As indicated in Figure 1, the area is crossed by two major rivers Kiffisos and Ilissos flowing into the bay.

The study area has experienced both an increasing urbanization trend and significant population growth in the past century. Besides the high-value residential buildings, numerous high impact infrastructures, such as hospitals, stadiums, as well as the National Library and the National Opera House of Greece, are located there. Also, several urban rail lines, sensitive to displacements, are crossing the site. As already mentioned, the future foresees an even more intensive development, supported by the location of the site along the coastline.

Since the 50's, an extensive industrial zone has been established north of Moschato municipality, the Tavros Industrial zone. It was a mixed industrial park including companies dealing with food processing, leather and fabric processing, footwear and cloth production, and construction materials production; most of them highly water consuming. The industrial activity was severely affected by the financial crisis period, 2009-2018, when the use of the park gradually changed from industrial to commercial, as most of the remaining companies are dealing with logistic activities.

2.1. Geological Setting. Regarding the geological setting of the study area (Figure 2), the top layers are occupied by loose Quaternary deposits; including slightly unconsolidated fine-grained fluvial sediments of Kiffisos and Ilissos rivers and coastal deposits. The deeper strata consist of Pleistocene fine-grained deposits, while the underlay Neogene formations are considered to be the bedrock formation [48, 49].

The loose Quaternary coastal deposits mainly consist of soft clay horizons intercalated with sandy silt to silty sand and silt. These deposits cover a wide zone along the coastline extending to the north for more than 1.5-2.0 Km, reaching down to a maximum depth of approximately 20 m (Figure 2).

The Quaternary fine-grained fluvial deposits consist mainly of sandy clay of low to medium plasticity; intercalate with clayey-silts, clayey-sands, silty sands, and clayey-silty gravels. According to data coming from geotechnical boreholes, their maximum thickness is approximately 30 m, and their lower strata are occupied by the coarser sandy and gravel horizons.

The Pleistocene fine-grained deposits consist of a red-brownish sandy clay (sandy loam) horizon with fine gravels and pisolites, intercalated with loose conglomerates. The Neogene basement is represented by alternate beds of marls, marlstones, marly limestones, dolomitic limestones, and locally intercalations of sandstones, conglomerates, and occasionally lignite. The thickness of the Neogene sediments is approximately 180 m, outcropping at the southwest of the Athens basin (Figure 2).

A number of probable inactive faults of NNW- SSE and NE-SW direction have been identified intersecting the Pleistocene and the Neogene formations of the wider study area [50] (Figure 2).

2.2. Geotechnical Setting. Considering the geotechnical properties of the Quaternary soil formations, it is clear that, according to the oedometer tests, the silty horizons of the coastal deposits are highly compressible presenting compression index (Cc) values ranging from 0.06 to 0.23 (Table 1). Besides that, the Standard Penetration Tests (SPT) reveled that they are loose, as the Nspt values are low, varying from 2 to 14. These horizons certainly contribute to the high compressibility potential of the coastal deposits.
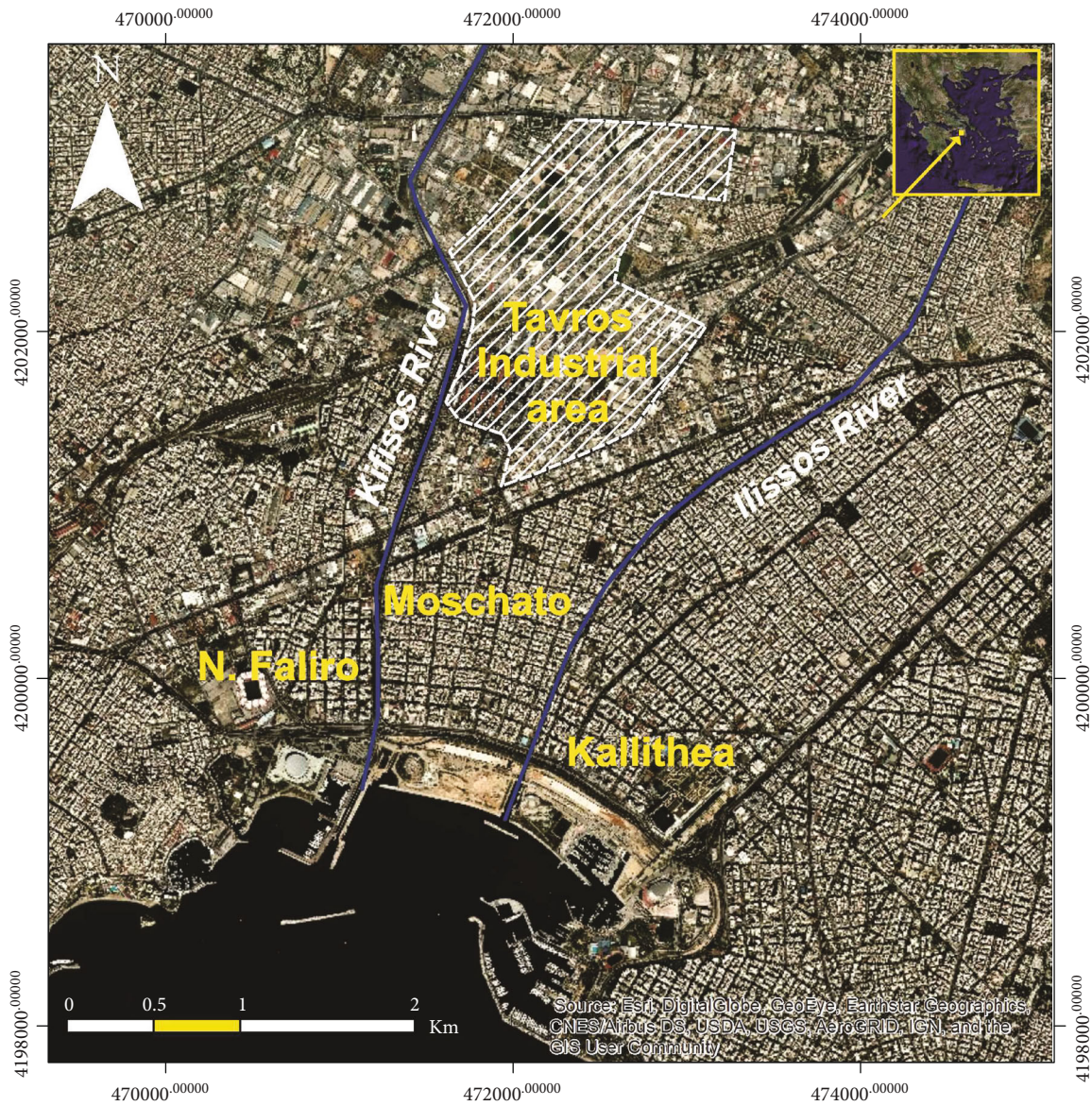
FIGURE 1: Location map of the study area.

Furthermore, evaluating the overall properties of the coastal deposits, the oedometer tests reviled that the preconsolidation pressure values of several samples have been systematically recorded slightly below the effective geostatic stresses, proving that the loose coastal deposits occur slightly underconsolidated, and as a result susceptible for the manifestation of deformations due to natural compaction. So, a wide zone extending from the coastline up to the southeast boundaries of the industrial zone is susceptible for the manifestation of land subsidence also due to the natural compaction of the relatively unconsolidated formations.

Regarding the Quaternary fluvial deposits, the sandy clay horizons, constituting 70% of the formation, appear to be stiff with low to medium plasticity, normally consolidated and with low to medium compression index (Cc) values, ranging from 0.09 to 0.32 (Table 2). Respectively, the silty sands and clayey-silty gravels are stiff, with even higher compression

index (Cc) values. So, the fluvial deposits are less susceptible to the manifestation of subsidence phenomena than the coastal deposits.

The Pleistocene fine-grained deposits include mainly fine-grained horizons up to a percentage of 80%. As indicated by the high NSPT values, they are stiff (Table 3), and as a result, they are not expected to have any particular contribution on the land subsidence mechanism.

2.3. *Hydrogeological Setting.* Two interacting aquifer systems can be identified, a shallow—unconfined and a deeper semiconfined. The shallow aquifer occupies the top coarse-grain horizons of the Quaternary deposits, while the semiconfined the deeper horizons extending deep down to the Pleistocene deposits.

Furthermore, a confined aquifer system is formed at the semipermeable sandstone and conglomerate horizons of the
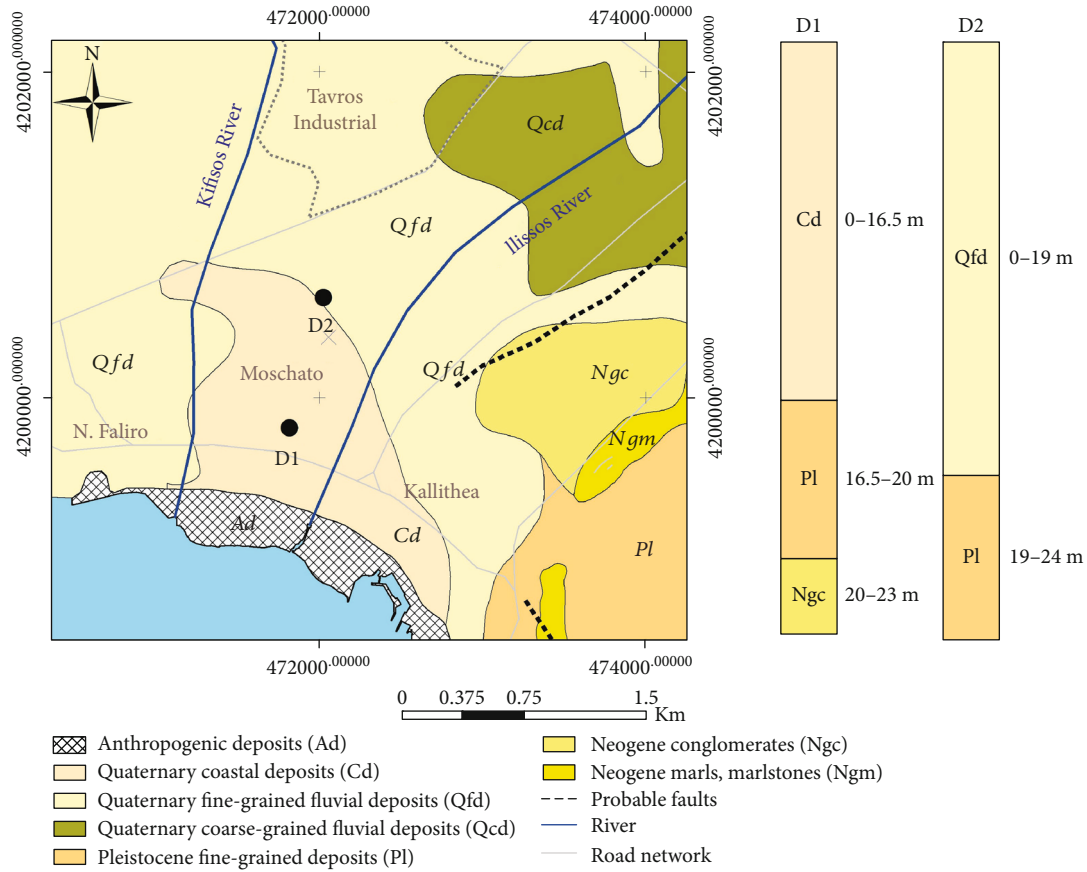
FIGURE 2: Geological map of the study area (modified by [51, 52]).

TABLE 1: Physical and mechanical properties of loose Quaternary coastal deposits [53–58].

	Silty clay			Silt			Silty sand		
	Unified Soil Classification System (USCS) classification								
	CL, CH			ML, CL-ML			SM		
	Min	Max	Av.	Min	Max	Av.	Min	Max	Av.
Physical parameters									
Liquid limit, LL (%)	25	48.5	37.3	-	-	-	-	-	-
Plasticity index, PI (%)	9	29.5	18.9	-	-	-	-	-	-
Mechanical parameters									
UC strength, q_u (KN/m^2)	28	150	77.7	20	44	33	21	36	28.5
Initial void ratio, e_o	0.55	1.7	0.91	0.62	0.86	0.74	0.54	0.8	0.69
Compression index, C_c	0.2	0.8	0.42	0.06	0.23	0.14	-	-	-
Standard penetration test (SPT)									
N_{SPT}	2	14	6.5	3	42	17	10	46	23
Triaxial test (UU)									
Cohesion, C (KN/m^2)	6	82	23	5	56	22.5	1	30	14
Friction angle, φ (°)	1	23	7	19	40	31	30	42	36

Neogene formations. Although these aquifers appear to be protected from the seawater intrusion by the impermeable marl horizons, they are not exploited due to their poor recharge rates.

Previous hydrochemical studies [59, 60] have identified the intrusion of seawater along the coastline, during the late 90s. The overpumping of the groundwater, at the industrial area of Tavros, had been cutting off the underground feed of the aquifers located along to the coastline causing their depression and as a result the intrusion of the seawater. The depression cone extending from the Tavros industrial zone down to

TABLE 2: Physical and mechanical properties of the Quaternary fine-grained fluvial deposits [53–58].

	Sandy clay			Silty sand		
	Unified Soil Classification System (USCS) classification					
	CL			SM		
	Min	Max	Av.	Min	Max	Av.
Physical parameters						
Dry unit weight, γd (KN/m³)	10.7	18.8	15.69	14.8	22.4	18.28
Specific gravity, G_s	2.49	2.67	2.55	2.58	2.58	2.58
Liquid limit, LL (%)	21.2	57.5	36.53	N.P.	39.7	23.41
Plastic limit, PL (%)	12.9	27.8	19.73	N.P.	19.4	14.47
Plasticity index, PI (%)	2.1	33	16.87	N.P.	23.3	9.49
Mechanical parameters						
UC strength, q_u (KN/m²)	35	399	172	36	353	213,33
Compression index, C_c	0.09	0.32	0.2		0,11	
Shear box test (CD)						
Cohesion, c (KN/m²)	1	49	10.28	8.5	31	19.75
Friction angle, φ (°)	3	31	23.14	26	28	27
Triaxial test (CUPP)						
Cohesion, c (KN/m²)	26	30	27.67	-	-	-
Cohesion, c' (KN/m²)	23	34	27.33	25		-
Friction angle, φ (°)	14	29	19.67	-	-	-
Friction angle, φ' (°)	17	31	23.67	31		-

TABLE 3: Physical and mechanical properties of the Pleistocene fine-grained deposits [53–58].

	Clayey sand			Sandy clay		
	Unified Soil Classification System (USCS) classification					
	SM			CL, CH		
	Min	Max	Av.	Min	Max	Av.
Physical parameters						
Liquid limit, LL (%)	20.1	34.2	27.5	23	43.2	30.6
Plasticity index, PI (%)	7.5	20	12.2	7.5	27.9	15
Mechanical parameters						
UC strength, q_u (KN/m²)	88	196	140	110	398	198
Initial void ratio, e_o	0.33	0.45	0.40	0.39	0.71	0.49
Compression index, C_c	0.10	0.14	0.12	-	-	-
Standard Penetration Test (SPT)						
N_{SPT}	16	>50	-	25	>50	-
Triaxial test (UU)						
Cohesion, c (KN/m²)	30	40	37	-	-	-
Friction angle, φ (°)	7	24	17	-	-	-

the coastline can be clearly identified at the piezometric map of July 1997 [59] (Figure 3(a)).

The annual water demand in the Tavros industrial area was continuously increasing until the mid-2000s. In the last years, the water demand was reduced and according to piezometric measurements conducted during 2015, the groundwater level gradually recovered. So, by comparing the July 1997 piezometric lines [59] with those based on the data collected during the May 2015 campaign, it is clear that the aquifers have recovered throughout the entire study area (Figures 3(a) and 3(b)). As presented in Figure 3(b), the zero level contour line moved back close to the coastline. The aforementioned recovery is related to the reduction of the water consumption for industrial purposes, triggered by the economic crises of the late 2000s and the resulting changes on the industrial activities.

A clear view of the changes taking place in the last two decades at the groundwater piezometry can be seen in Figure 4, presenting the equal drawdown contour lines produced by comparing the July 1997 and May 2015 piezometric surfaces. As clearly presented, at the vicinity of the Tavros industrial area, the groundwater level has risen up 3 to 7 m since 1997. Along the coastline, the recovery uplifted the groundwater level for 1 to 2 m, moving the zero level piezometry contours back along the coastline, regenerating the barrier protecting the inland from the seawater intrusion.

3. Land Subsidence Historical Background and Ground Truth Data

Since the mid 60's, the coastal zone of the N. Faliro, Moschato, and Kallithea municipalities has experienced land subsidence phenomena associated mainly with groundwater exploitation [43, 59]. A leveling network has been established since 1989 and geodetic surveys have been carried out in the study area [44]. These measurements indicate significant
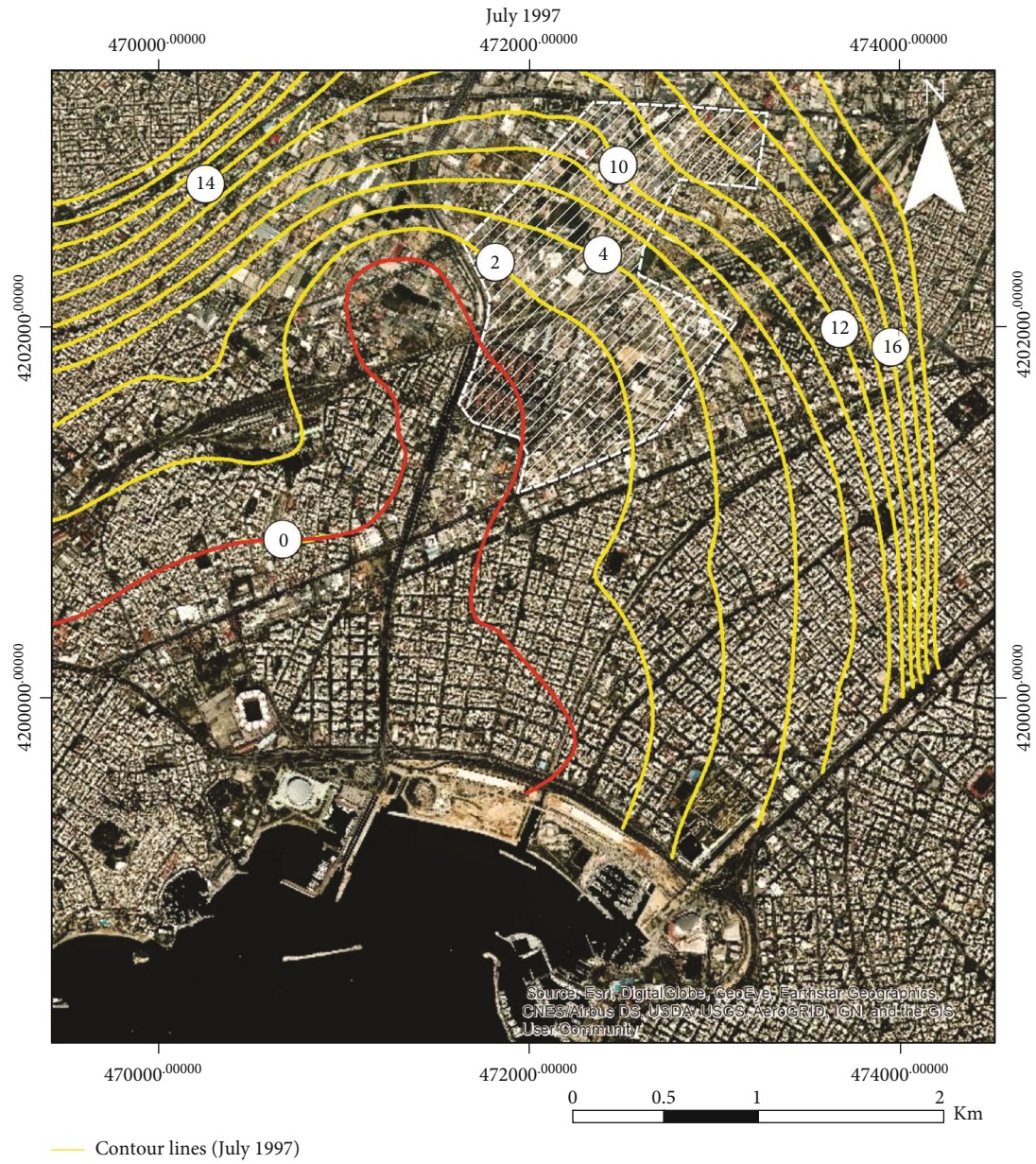
Contour lines (July 1997)

(a)

Figure 3: Continued.

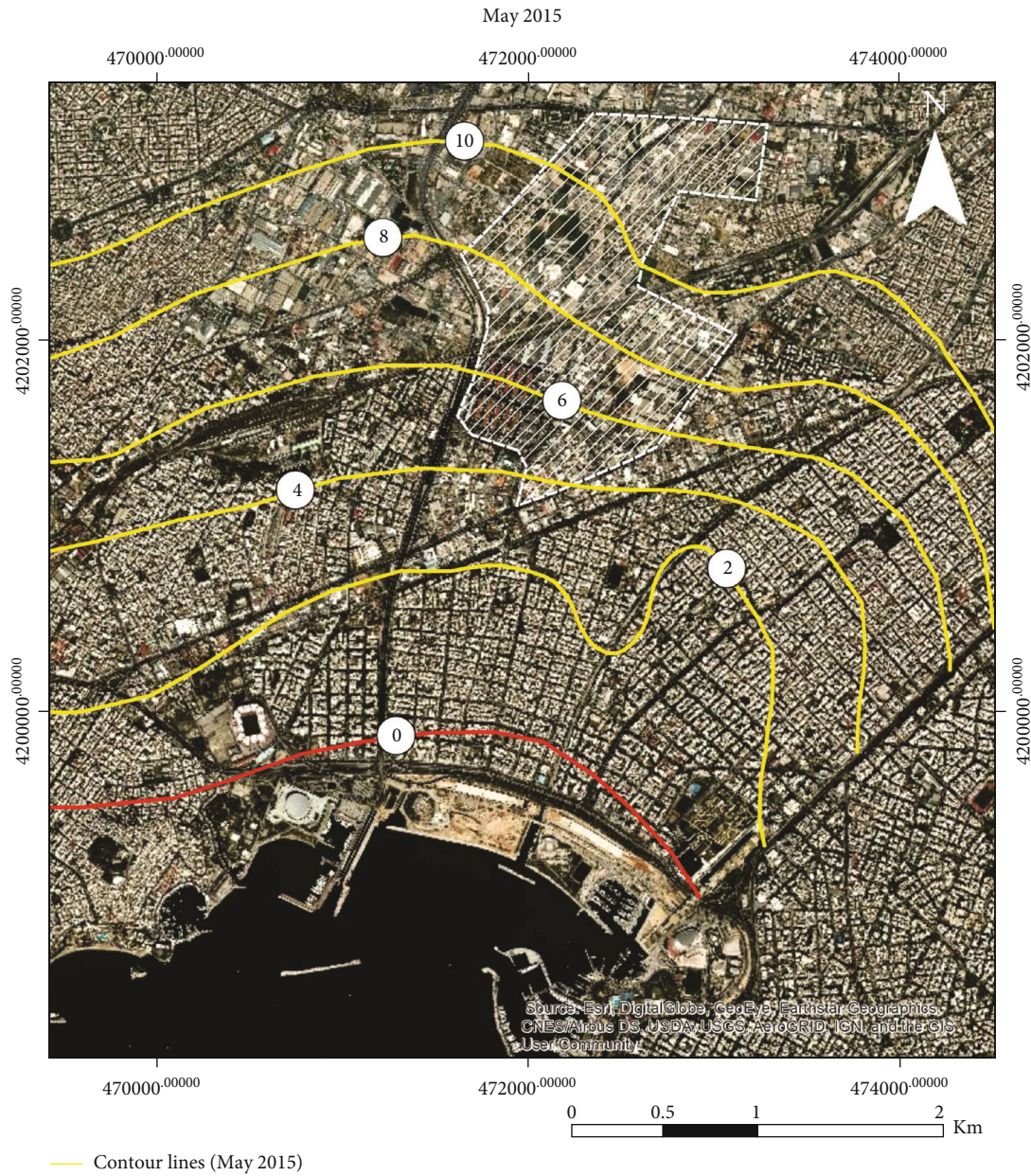May 2015

Contour lines (May 2015)

(b)

FIGURE 3: (a) Piezometric contour lines of July 1997, (b) Piezometric contour lines of May 2015.

vertical displacements at the area extending between the outlets of the Kiffisos and Ilissos rivers (Figure 5).

The maximum displacement rates identified by the vertical geodetic control network can be distinguished into three periods [44]. The first period extends from 1989 to 1995 (Figure 5(a)). At the time, the deformations were affecting a zone extending approximately 500 m north of the Avenue running along the coastline. The maximum total subsidence values were reaching up to -16 mm (approx. -3 mm/yr) [43]. The second period extending from 1995 to 2001 (Figures 5(b) and 5(c)) was a quiet period with maximum total subsidence displacements less than -4 mm [45, 46]. During the period from 2001 to 2008, the accumulated deformation reached a maximum value of -23 mm (approx. -3.5 to

-4 mm/yr) [47]. The deformation affected the entire area between the two riverbeds, up to the Tavros industrial zone. Curves with positive deformation values, indicating uplift, are probably related with control points attached to rigid constructions presenting tilting or rotational movements, uplifting them.

At this point, it should be noted that at the early 2000's, due to the pre-Olympic game financial growth of the country, the activities at the Tavros industrial area were expanding. The construction activities, resulting to extensive draining works, were also growing at the entire coastal zone. Furthermore, Kiffisos River was fully channelized cutting off the outflows to the aquifers. So, although no groundwater level measurements exist for that time period, it is fully acceptable

Difference between July 1997 and May 2015

Possitive difference (recharge) between July 1997 and May 2015
Zero difference between July 1997 and May 2015
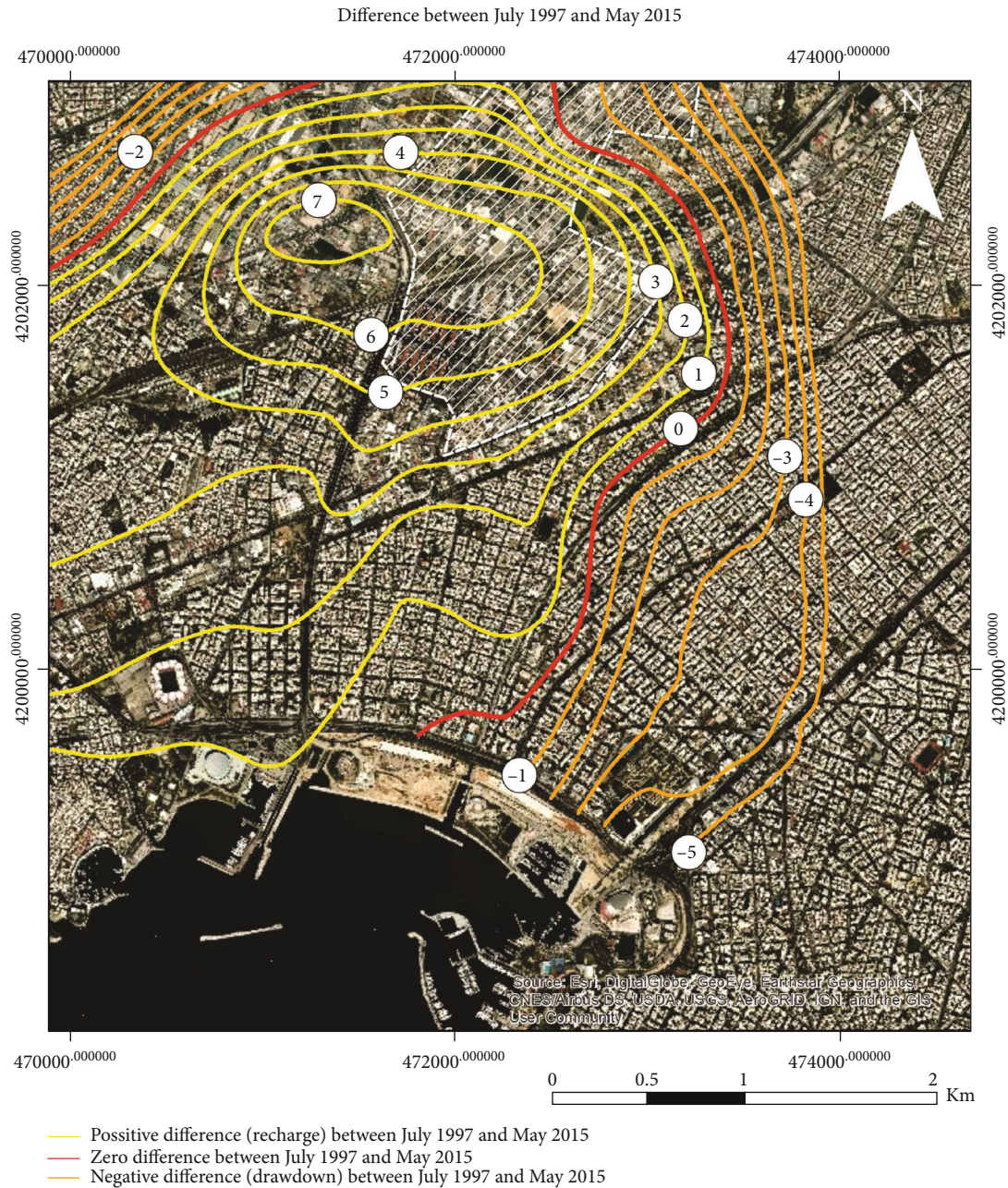Negative difference (drawdown) between July 1997 and May 2015

FIGURE 4: Contours indicating the difference of the groundwater level between May 2015 and July 1997.

that the groundwater table was susceptible to drawdown, justifying the amplified subsiding deformations observed between 2001 and 2008.

Following the spatial distribution of the deformations, numerous surface ruptures and structural failures can be identified at the area between the riverbeds of Kiffisos and Ilissos (Figure 6).
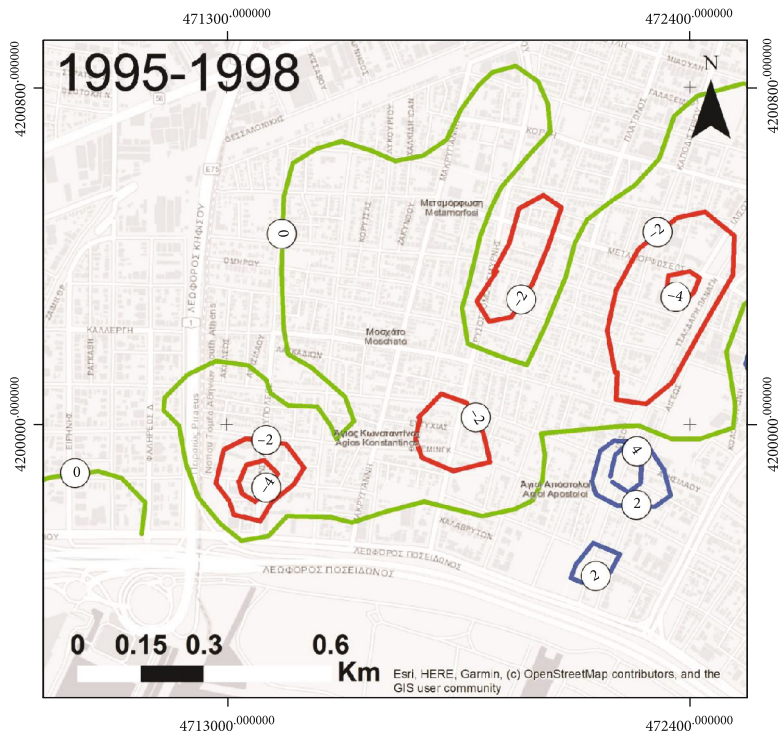
4. Multitemporal InSAR Methods and Processed Data

In the present study, twenty Single Look Complex (SLC) Advanced Synthetic Aperture Radar (ASAR) C-band images

of ESA (European Space Agency) Envisat satellite have been processed. The images refer to the time period between 2002 and 2010, and they are acquired along the descending orbit. Due to the poor dataset of available scenes covering a period of 8 years, two multitemporal InSAR techniques have been applied namely (a) SBAS-type processing and (b) the Persistent Scatterer Interferometry using the IPTA (Interferometric Point Target Analysis) algorithm for the production of time series deformation maps. The first and common step after the introduction of the images in the system is a Digital Elevation Model- (DEM-) assisted coregistration procedure, implemented at the SLC images. The SBAS-type method is characterized by a first multireference interferometric
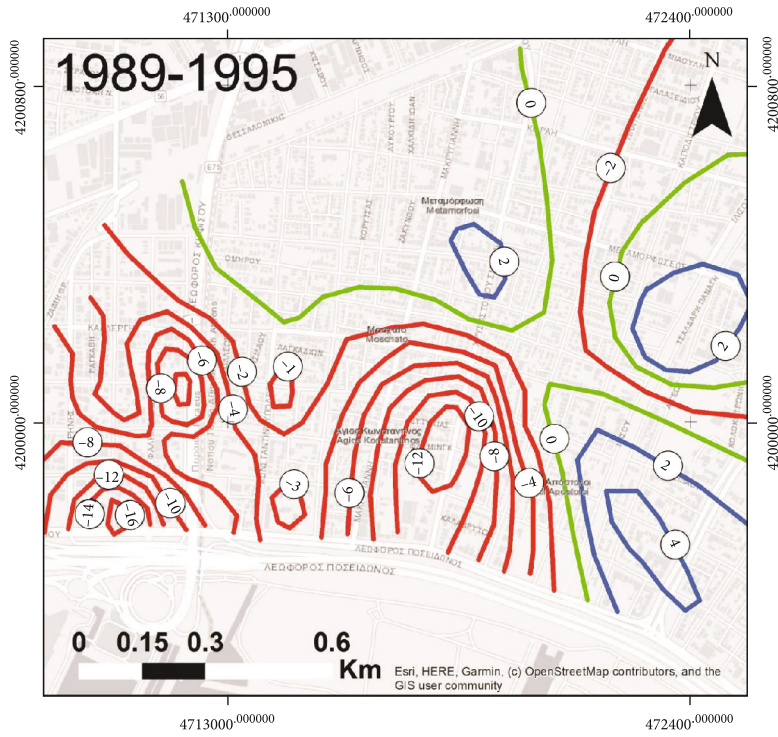
(a)

(b)

Figure 5: Continued.

(c)
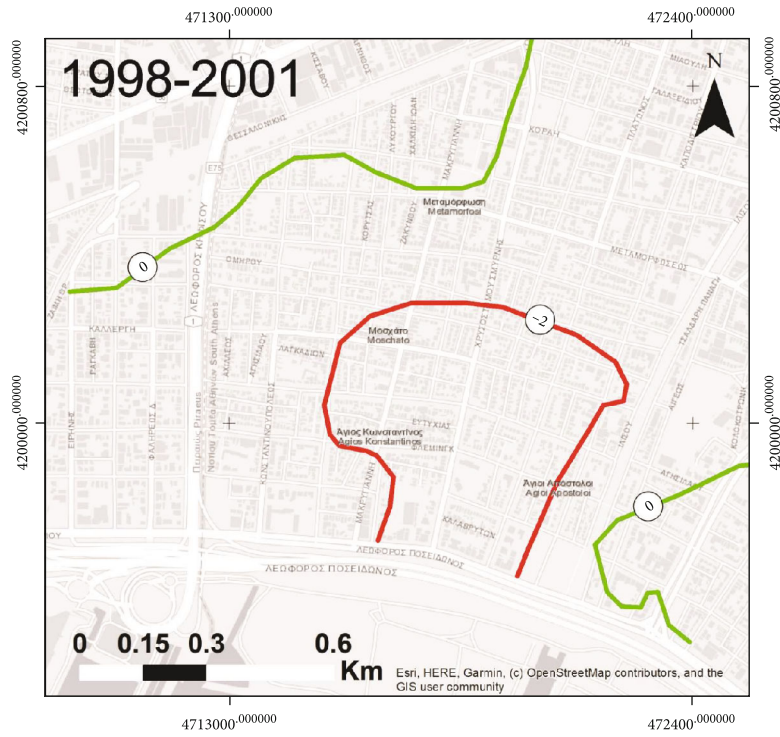
(d)

Figure 5: Vertical displacements contour lines referring to four periods. (a) 1985-1995, (b) 1995-1998, (c) 1998-2001, and (d) 2001-2008.
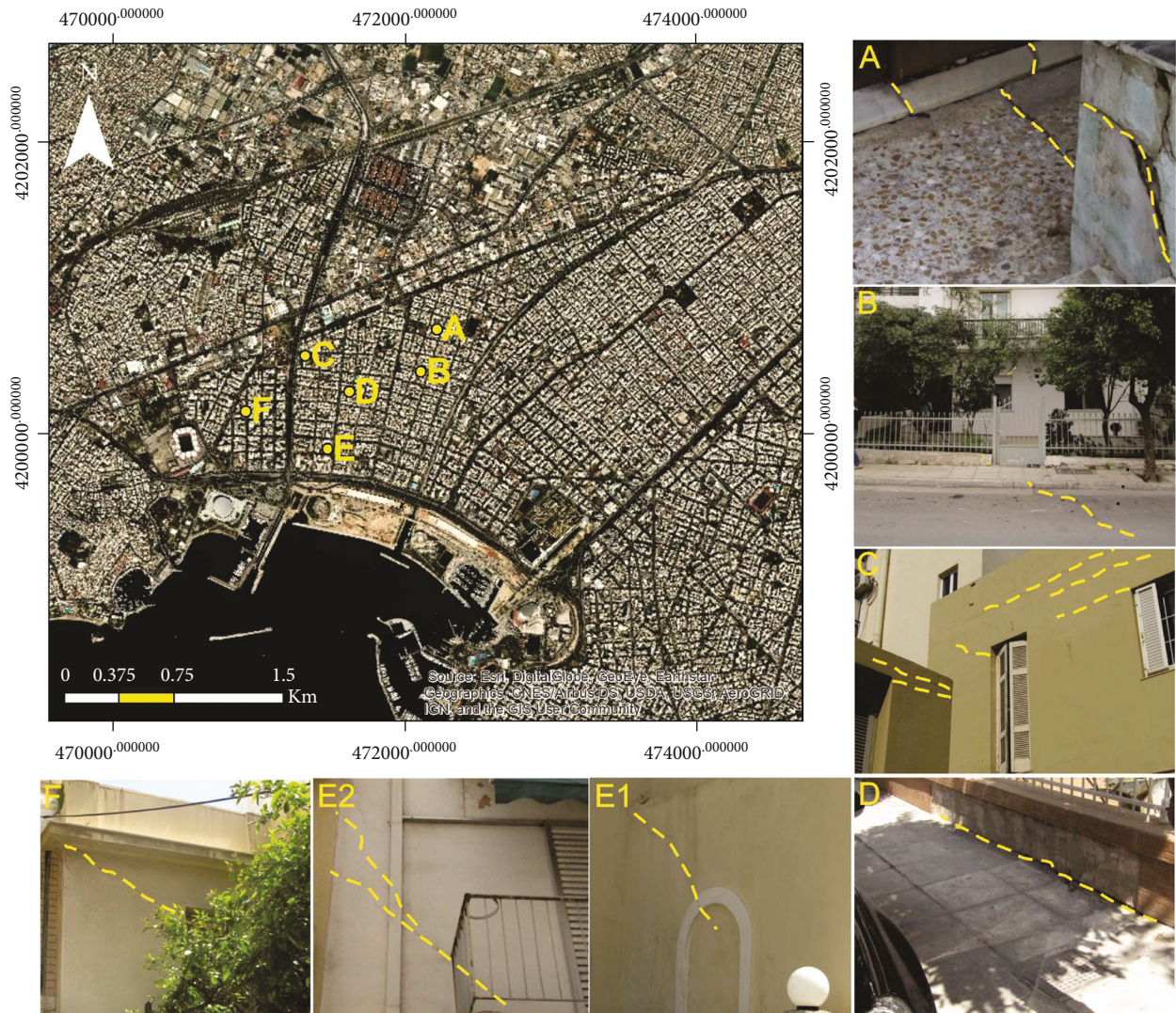
FIGURE 6: Field evidence of surface ruptures and building failures along the study area.

processing to a single reference image by applying the SVD algorithm [61], obtaining the time series surface deformation. The second one is the classical time series interferometric processing. Both techniques at the last step of processing transform the deformation phase into line-of-sight (LOS) displacement and geocoded maps (Figure 7).

Aiming to extend the study of the phenomenon further to the past, already processed Persistent Scatterer Interferometry (PSI) data covering the time period from 1992 to 2001 were also evaluated. The PSI analysis was conducted within the framework of the ESA GMES Terrafirma project (GMES—Global Monitoring for Environment and Security) funded by the European Space Agency (ESA) [40]. During this project, 9 satellite image frames were processed using a special semiautomated processor to produce a PSI ground motion map covering a $65,000\,Km^2$ area of Greece. This Wide Area Product (WAP) over Greece is based on strip map ERS 1/2 images, obtained from the ESA.

The SBAS-type processing using the SVD algorithm method allows connecting disjoint subsets of interferometric pairs separated by large baselines [61, 62]. SVD relies on the minimum-norm criterion of the deformation rate to acquire time series [63, 64]. The benefit of this technique is that the nonlinear deformation can be estimated without the need of a priori assumption of a deformation model or past knowledge and as any other multi-temporal approach, the mitigation of decorrelation phenomena and topographic inaccuracies are limited [62]. More precisely, this approach is characterized by a first multireference interferometric processing. So, a large number of interferometric pairs are produced to a single reference image interferometric processing, obtaining the time series surface deformation by applying the SVD algorithm [59]. In this way, any potential deformation values that may occur between two dates are added to the subsequent one, for each image acquisition until the last one. Therefore, creating a cumulative deformation history for each pixel that exists in the available time interval and thus enabling the creation of time-series graphs.

At the IPTA technique, based on the coregistered SLC scenes, two lists of candidate point scatterers were initially
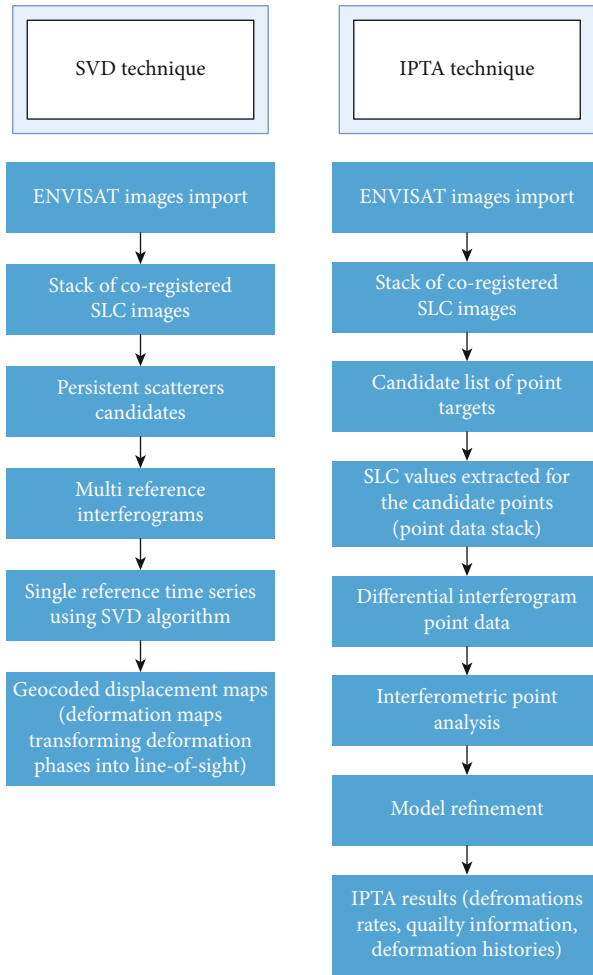
FIGURE 7: Flowcharts of the SVD and IPTA techniques.

generated using different selection approaches. Next, two point lists were generated and combined into a single one, which was used in additional processing after removing duplicate records. The single reference method has been used in order to form multiple pairs of interferograms. The criteria by which the reference scene was selected are the following: (i) forming interferometric pairs with the minimum baseline backprojection (Bp), (ii) acquisition date near the central date of the time period for which there are available SAR acquisitions, and (iii) reference scene to present low atmospheric distortions.

Consequently, the initial point differential interferograms were generated using the coregistered SLCs, the DEM heights, and the predefined Persistent Scatterers (PS) list. The topographic component was subtracted using the DEM. The generated point differential interferograms were further analyzed in the temporal and spatial domains in order to obtain information on the atmospheric phase term, deformation phase, and baseline errors.

The following steps involved least-square regression using the differential phases in an iteration process to estimate scattering heights and the deformation rate relative to the selected reference area.

Based on the regression analysis, the quality of the PS candidates was further evaluated through the estimated standard deviation of the phase difference.

Furthermore, since residual phases contain the atmosphere, nonlinear deformation components, and other error terms, they were further processed in order to compensate for these effects. Thus, residual phases were filtered assuming that atmospheric contribution is high-pass in time and low-pass in space. Further iteration was done in order to consider these corrections in the final regression model. It is worth mentioning that phase unwrapping is performed exclusively in the temporal domain, avoiding issues that could arise from error propagation when the spatial unwrapping of individual layers is considered. The generated results consist of height corrections, linear deformation rates, atmospheric phase, temporal coherence levels, and nonlinear deformation histories for each PS. Finally, the deformation phases were transformed into displacements and geocoded to a selected map.

5. Results and Discussion

5.1. Available PSI Land Motion Mapping Data (1992-2001). The available land motion mapping data, produced by PSI analysis, revealed vertical displacements at the wider study area during the time period from 1992 to 2001 (Figure 8(a)).

As presented in Figure 8(a), the Persistent Scatterers (PS) indicating subsiding movements (yellow to red dots) are concentrated along the coastal zone, with a higher density between the riverbeds of Kiffisos and Ilissos. Also, a stack of PSs can be identified at the northern part of the Tavros Industrial zone. The maximum displacement rates at the coastal zone reach up to values of -1.5 to -4 mm/yr, while even larger displacement values, up to -6.9 mm/yr, can be identified at the industrial zone. Also, the analysis of the time series clearly shows a steady downward trend in the time intervals covered by ERS 1/2 dataset (Figure 8(b)).

The spatial distribution of the deformations fits with those identified by the geodetic control network, although the maximum displacement values appear to be larger at the InSAR dataset.

5.2. IPTA and SVD Land Motion Mapping Data (2002-2010). Both DinSAR techniques applied at the Envisat data reveal an identical pattern of deformations for the time period extending from 2002 to 2010. As presented in Figures 9(a) and 10., both datasets indicate that the maximum displacements can be identified at the area included between the riverbeds of Kiffisos and Ilissos, at the south of the Tavros industrial zone. Nevertheless, slight differences can be identified at the maximum displacement rates. The Interferometric Point Target Analysis (IPTA) indicated deformation rates of -3 to -5 mm/yr, along the satellite's LoS (Figure 9(a)), whereas the Singular Value Decomposition (SVD) interferometric technique indicates lower LoS deformation rates, ranging between -1.5 and -3 mm/yr (Figure 10).

Displacement time series are also available for each PS target, ideally suited for monitoring the temporal evolution of displacement for the investigated period of time.

(a)
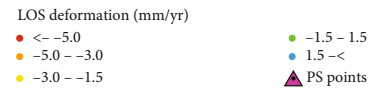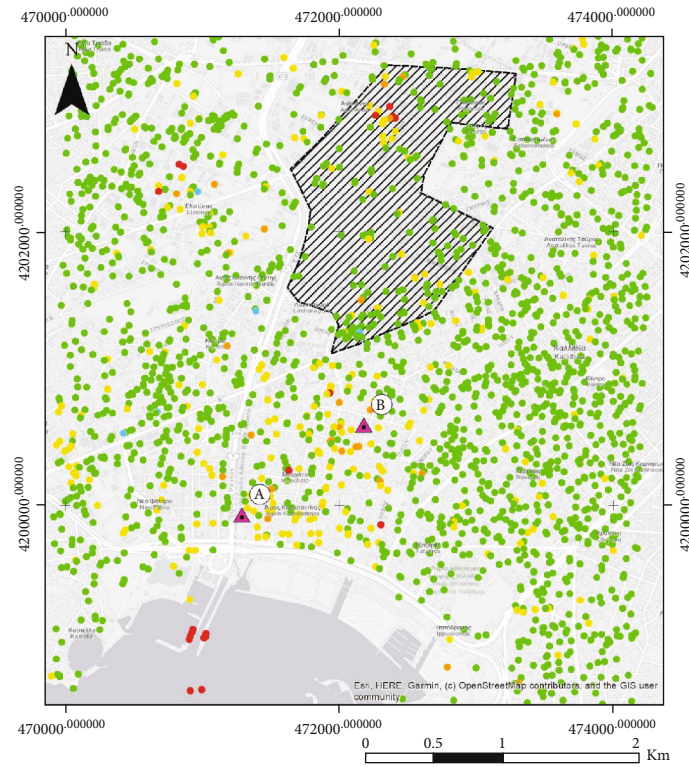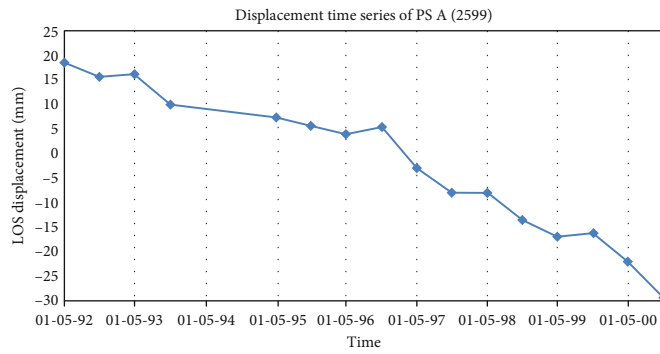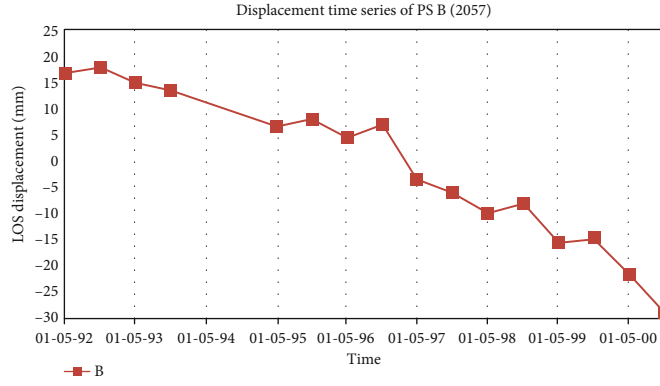
(b)

FIGURE 8: (a) Velocities from 1992 to 2001 as derived by the PSI analysis of ERS 1/2 acquisitions. (b) LoS displacement time series of PS A and B.

(a)

(b)

Figure 9: (a) Displacement rates from 2002 to 2010 as derived by the IPTA analysis of Envisat acquisitions. (b) LoS displacement time series of PS A and B.

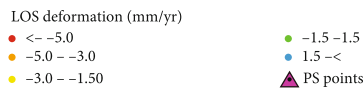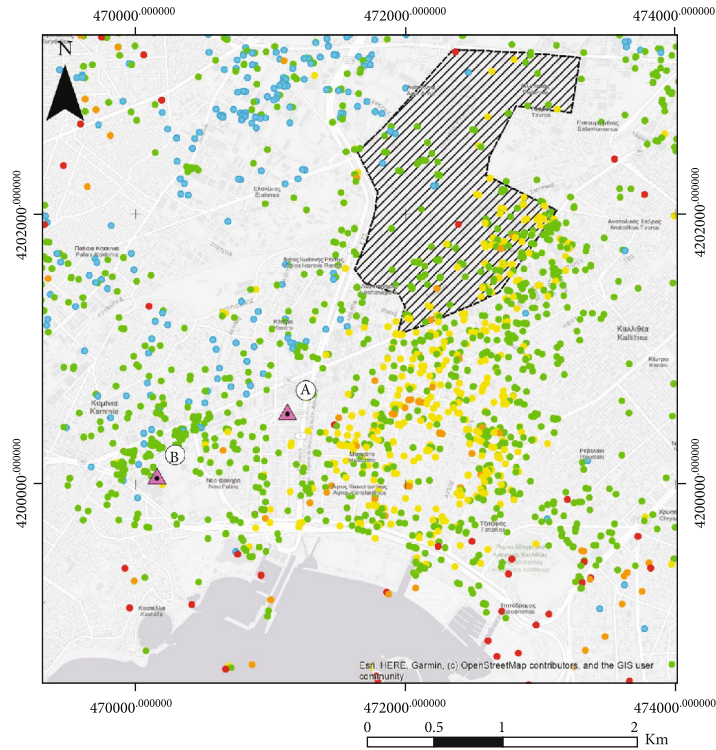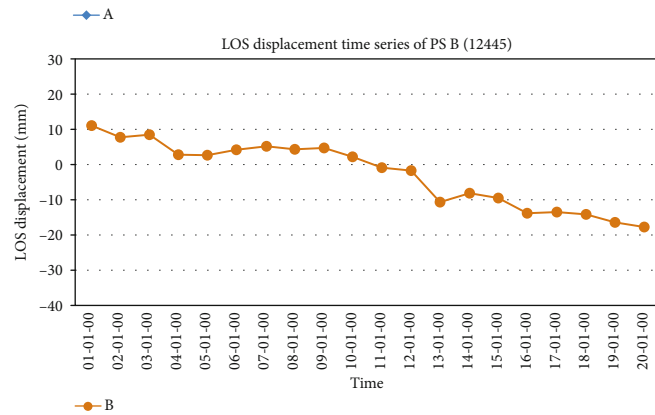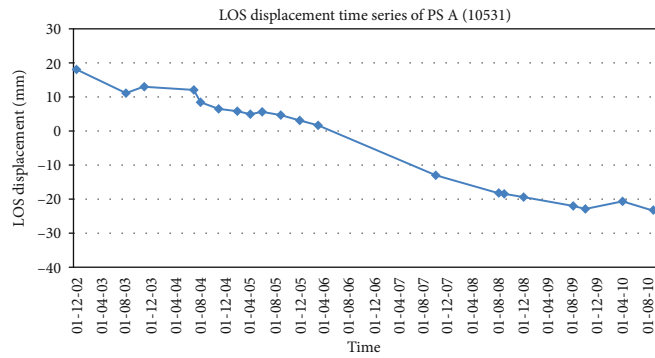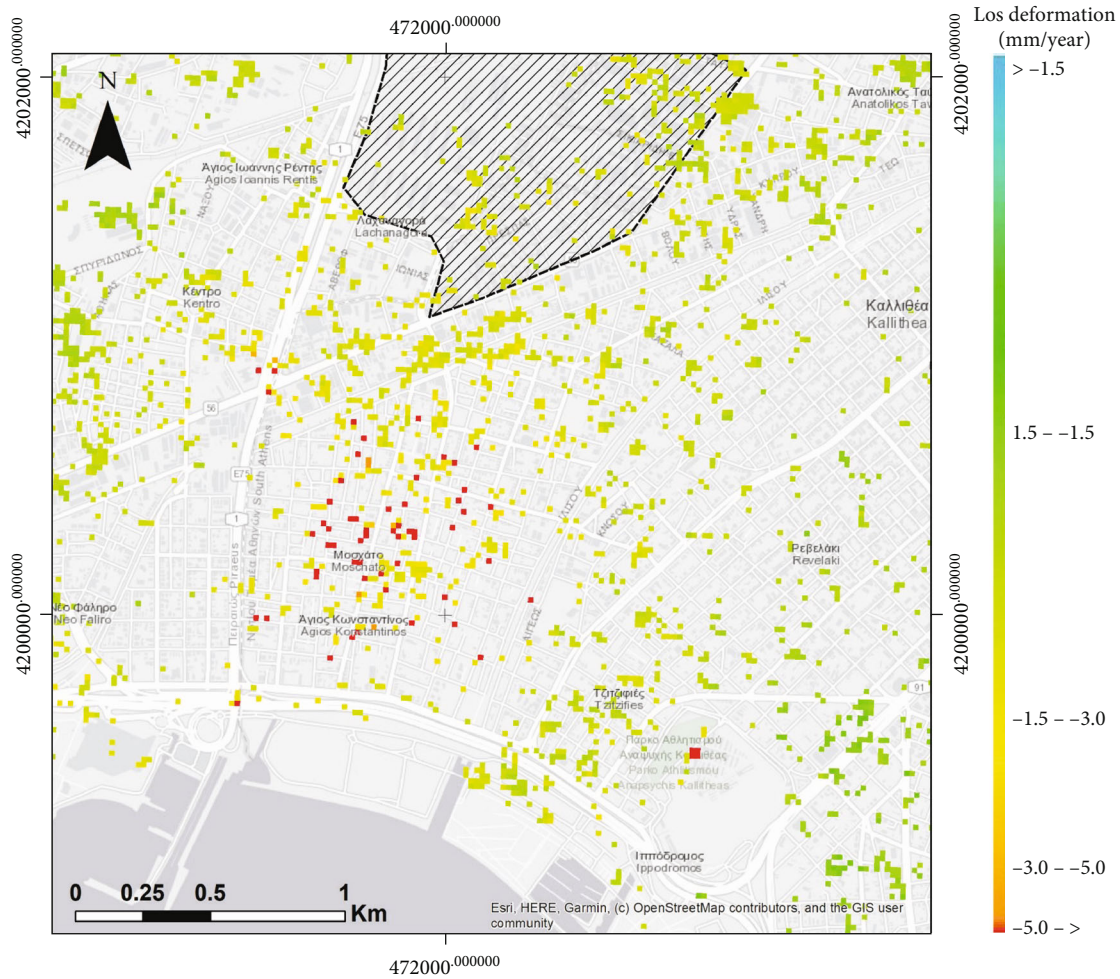FIGURE 10: Displacement rates from 2002 to 2010 as derived by the SVD analysis of Envisat acquisitions.

Characteristic graphs referring to two PSs affected by the ground motion are reported in Figure 9(b).

5.3. Correlation of Space Borne, Geodetic, Hydrogeological, and Geotechnical Data. The space-born interferometric data indicate clearly that the area affected the most by the land subsidence is the one extending between the riverbeds of Kiffisos and Ilissos. This conclusion fits perfectly with the results coming from the vertical geodetic control network. Evaluating the displacement rate values, the PSI dataset coming from the processing of the ERS 1/2 acquisitions indicate slower displacement rates during 1992 to 2001 than those identified by the Envisat data for the period 2002-2010. So, as in the case of the geodetic measurements, the deformations were accelerated during the second decade. Nevertheless, the displacement rate values of the first decade (1992-2001) do not fit perfectly with the geodetic data. Particularly, the geodetic measurements indicate displacements with velocities lower than -1 mm/yr while the PSI dataset velocities from -1.5 up to -4 mm/yr. On the contrary, the IPTA dataset of the second decade (2002-2010) fit perfectly with the geodetic data as both indicate displacement rates from -3.5 to -5 mm/yr.

Comparing the July 1997 groundwater contour lines (Figure 3(a)) with the distribution of the displacements acquired by both space-born and geodetic data, it is clear that the maximum displacements are located at the area affected by the depression cone, extending from the industrial zone down to the coastline. Unluckily, there are not any groundwater level measurements referring to the period between 2002 and 2010, in order to correlate them with the acceleration of the displacements. Nevertheless, as already mentioned, the pre-Olympic games financial growth of the country, during the early 2000's, expanded the activities of the Tavros industrial zone, as well as the construction activities along the coastal front, tensioning the depression of the aquifers. The full channelization of the Kiffisos River outlet, completed before the Olympic games of 2004, supported the evolution of the depression cone by cutting off the outflows of the river's water to the aquifers. The effect of the rebound of the aquifer on the deceleration of the displacements cannot be witnessed as space-born or geodetic data are not available for this time period. As mentioned, the rebound of the aquifer, identified at the contour lines of 2015 (Figure 3(b)), can be attributed to the financial crises pausing all financial activities (industrial and construction) at the site.

Regarding the geotechnical properties of the geological formations, the loose silty horizons of the Quaternary coastal deposits present low compression index (Cc) values making them highly susceptible to the manifestation of land subsidence due to consolidation. The deformations attributed to the remaining natural compaction of those formations combined with the occasional consolidation events caused by the newly build constructions triggers additional deformations at the areas occupied by the coastal deposits.

6. Conclusions

The study area is a high-interest urban site along the Faliro bay coastal zone of the city of Athens, including districts of the Neo Faliro, Moschato, and Kallithea municipalities. The site, planed to be the Greek Riviera, is subjected to continuous deformations due to the land subsidence phenomena, occurring since the mid 60's.

The present study provides a methodological approach for the identification of the subsidence mechanism by combining the geotechnical characteristics with the hydrogeological data and by verifying the displacements with the use of space-born SAR interferometry (InSAR) techniques and ground truth geodetic measurements.

As proved by the groundwater leveling data, the industrial zone extending at the north of the study area, due to the overexploitation of the aquifers, causes the development of an extensive depression cone, extending down to the coastline. Furthermore, the costal deposits covering a big part of the study area are proved to be compressible due to the low compression index (Cc) values identified in some of their silty horizons. So, the development of the depression cone is expected to be the main cause of the land subsidence affecting the entire area extending between the riverbeds of Kiffisos and Ilissos. Also, an additional deformation component is expected at the areas occupied by the coastal deposits as they have been proved to be slightly unconsolidated.

The manifestation of the expected deformations has been verified with excellent accuracy by the use of space-born SAR interferometry (InSAR) techniques. Furthermore, the results of the InSAR techniques have been crosschecked with measurements acquired by a vertical geodetic control network as well as by ground truth data, referring to damage traced on building and rigid constructions.

The current research demonstrates an interesting case study of an urban site affected for a long-lasting time period by the activities of a neighboring industrial zone. The complexity of the geological, hydrogeological, and geotechnical conditions and the interaction of the numerous land use activities make this study far more interesting.

Furthermore, this study demonstrates the potential of space-borne InSAR techniques as a suitable tool for the validation of the subsidence movements; a cost-efficiency method, complimentary to ground-based measurements.

Eventually, the current study indicates that by applying the proper techniques and methodology the early detection of surface deformations can be established, allowing taking measures before severe subsidence occurs and therefore allows for timely protection of the affected areas.

Conflicts of Interest

The authors declare no conflict of interest regarding this publication.

References

[1] C. Loupasakis and D. Rozos, "Finite-element simulation of land subsidence induced by water pumping in Kalochori village, Greece," *Quarterly Journal of Engineering Geology and Hydrogeology*, vol. 42, no. 3, pp. 369–382, 2009.

[2] D. L. Galloway and T. J. Burbey, "Review: regional land subsidence accompanying groundwater extraction," *Hydrogeology Journal*, vol. 19, no. 8, pp. 1459–1486, 2011.

[3] J. Pacheo-Martínez, M. Hernandez-Marín, T. J. Burbey et al., "Land subsidence and ground failure associated to groundwater exploitation in the Aguascalientes Valley, México," *Engineering Geology*, vol. 164, pp. 172–186, 2013.

[4] P. Ezquerro, C. Guardiola-Albert, G. Herrera, J. F. Fernández-Merodo, M. Béjar-Pizarro, and R. Bonì, "Groundwater and subsidence modeling combining geological and multi-satellite SAR data over the alto guadalentín aquifer (SE Spain)," *Geofluids*, vol. 2017, Article ID 1359325, 17 pages, 2017.

[5] P. Tzampoglou and C. Loupasakis, "Numerical simulation of the factors causing land subsidence due to overexploitation of the aquifer in the Amyntaio open coal mine, Greece," *HydroResearch*, vol. 1, pp. 8–24, 2019.

[6] G. Gambolati, M. Putti, P. Teatini, and G. Gasparetto Stori, "Subsidence due to peat oxidation and impact on drainage infrastructures in a farmland catchment south of the Venice lagoon," *Environmental Geology*, vol. 49, no. 6, pp. 814–820, 2006.

[7] T. Hoogland, J. J. H. Akker, and D. J. Brus, "Modeling the subsidence of peat soils in the Dutch coastal area," *Geoderma*, vol. 171-172, pp. 92–97, 2012.

[8] G. Caramanna, G. Ciotoli, and S. Nisio, "A review of natural sinkhole phenomena in Italian plain areas," *Natural Hazards*, vol. 45, no. 2, pp. 145–172, 2008.

[9] J. Galve, F. Gutiérrez, P. Lucha et al., "Probabilistic sinkhole modelling for hazard assessment," *Earth Surface Processes and Landforms*, vol. 34, no. 3, pp. 437–452, 2009.

[10] H. Ding, S. Chen, S. Chang, G. Li, and L. Zhou, "Prediction of surface subsidence extension due to underground caving: a case study of Hemushan Iron Mine in China," *Mathematical Problems in Engineering*, vol. 2020, Article ID 5086049, 10 pages, 2020.

[11] B. Osmanoglu, T. H. Dixon, S. Wdowinski, E. Cabral-Cano, and Y. Jiang, "Mexico City subsidence observed with persistent scatterer InSAR," *International Journal of Applied Earth Observation and Geoinformation*, vol. 13, no. 1, pp. 1–12, 2011.

[12] F. Cigna, B. Osmanoğlu, E. Cabral-Cano et al., "Monitoring land subsidence and its induced geological hazard with synthetic aperture radar interferometry: a case study in Morelia, Mexico," *Remote Sensing of Environment*, vol. 117, pp. 146–161, 2012.

[13] D. Massonnet and K. L. Feigl, "Radar interferometry and its application to changes in the Earth's surface," *Reviews of Geophysics*, vol. 36, no. 4, pp. 441–500, 1998.

[14] H. A. Zebker, P. A. Rosen, R. M. Goldstein, A. Gabriel, and C. L. Werner, "On the derivation of coseismic displacement fields using differential radar interferometry: the Landers earthquake," *Journal of Geophysical Research*, vol. 99, no. B10, pp. 19617–19634, 1994.

[15] M. P. Sanabria, C. Guardiola-Albert, R. Tomas et al., "Subsidence activity maps derived from DInSAR data: Orihuela case study," *Natural Hazards and Earth System Sciences*, vol. 14, pp. 1341–1360, 2014.

[16] L. Bateson, F. Cigna, D. Boon, and A. Sowter, "The application of the intermittent SBAS (ISBAS) InSAR method to the South Wales Coalfield, UK," *International Journal of Applied Earth Observation and Geoinformation*, vol. 34, pp. 249–257, 2015.

[17] A. Rosi, V. Tofani, A. Agostini et al., "Subsidence mapping at regional scale using persistent scatters interferometry (PSI): the case of Tuscany region (Italy)," *International Journal of Applied Earth Observation and Geoinformation*, vol. 52, pp. 328–337, 2016.

[18] L. Solari, A. Ciampalini, F. Raspini, S. Bianchini, and S. Moretti, "PSInSAR analysis in the Pisa urban area (Italy): a case study of subsidence related to stratigraphical factors and urbanization," *Remote Sensing*, vol. 8, no. 2, 2016.

[19] C. Da Lio and L. Tosi, "Land subsidence in the Friuli Venezia Giulia coastal plain, Italy: 1992–2010 results from SAR-based interferometry," *Science of the Total Environment*, vol. 633, pp. 752–764, 2018.

[20] M. Del Soldato, C. Del Ventisette, F. Raspini, G. Righini, V. Pancioli, and S. Moretti, "Ground deformation and associated hazards in NW peloponnese (Greece)," *European Journal of Remote Sensing*, vol. 51, no. 1, pp. 710–722, 2018.

[21] Z. Chen, J. Wang, and X. Huang, "Land subsidence monitoring in greater Vancouver through synergy of InSAR and polarimetric analysis," *Canadian Journal of Remote Sensing*, vol. 44, no. 3, pp. 201–214, 2018.

[22] A. Ciampalini, L. Solari, R. Giannecchini, Y. Galanti, and S. Moretti, "Evaluation of subsidence induced by long-lasting buildings load using InSAR technique and geotechnical data: the case study of a Freight Terminal (Tuscany, Italy)," *International Journal of Applied Earth Observation and Geoinformation*, vol. 82, article 101925, 2019.

[23] B. Hu, B. Yan, X. Zhang, X. Chen, and Y. Wu, "Time-series displacement of land subsidence in Fuzhou downtown, monitored by SBAS-InSAR technique," *Journal of Sensors*, vol. 2019, Article ID 3162652, 12 pages, 2019.

[24] E. Bekesi, P. A. Fokker, J. E. Martins, J. Limberger, D. Bonté, and J. D. Dan Wees, "Production-induced subsidence at the los Humeros geothermal field inferred from PS-InSAR," *Geomechanics*, vol. 2019, article 2306092, 12 pages, 2019.

[25] P. E. Yastika, N. Shimizu, and H. Z. Abidin, "Monitoring of long-term land subsidence from 2003 to 2017 in coastal area of Semarang, Indonesia by SBAS DInSAR analyses using Envisat-ASAR, ALOS-PALSAR, and Sentinel-1A SAR data," *Advances in Space Research*, vol. 63, no. 5, pp. 1719–1736, 2019.

[26] Y. Shi, Y. Tang, Z. Lu, J. W. Kim, and J. Peng, "Subsidence of sinkholes in Wink, Texas from 2007 to 2011 detected by time-series InSAR analysis," *Geomatics, Natural Hazards and Risk*, vol. 10, no. 1, pp. 1125–1138, 2019.

[27] A. Goorabi, M. Karimi, M. Yamani, and D. Perissin, "Land subsidence in Isfahan metropolitan and its relationship with geological and geomorphological settings revealed by Sentinel-1A InSAR observations," *Journal of Arid Environments*, vol. 181, article 104238, 2020.

[28] B. Chen, H. Gong, Y. Chen et al., "Land subsidence and its relation with groundwater aquifers in Beijing Plain of China," *Science of the Total Environment*, vol. 735, article 139111, 2020.

[29] L. Liu, J. Yu, B. Chen, and Y. Wang, "Urban subsidence monitoring by SBAS-InSAR technique with multi-platform SAR images: a case study of Beijing Plain, China," *European Journal of Remote Sensing*, vol. 2020, pp. 1–13, 2020.

[30] P. Ezquerro, M. Del Soldato, L. Solari et al., "Vulnerability assessment of buildings due to land subsidence using InSAR data in the ancient historical city of Pistoia (Italy)," *Sensors*, vol. 20, no. 10, 2020.

[31] S. Vassilopoulou, V. Sakkas, U. Wegmuller, and R. Capes, "Long term and seasonal ground deformation monitoring of Larissa plain (Central Greece) by persistent scattering interferometry," *Open Geosciences*, vol. 5, no. 1, pp. 61–76, 2013.

[32] F. Fakhri and R. Kalliola, "Monitoring ground deformation in the settlement of Larissa in Central Greece by implementing SAR interferometry," *Natural Hazards*, vol. 78, no. 2, pp. 1429–1445, 2015.

[33] M. Foumelis, E. Papageorgiou, and C. Stamatopoulos, "Episodic ground deformation signals in Thessaly Plain (Greece) revealed by data mining of SAR interferometry time series," *International Journal of Remote Sensing*, vol. 37, no. 16, pp. 3696–3711, 2016.

[34] I. Ilia, C. Loupasakis, and P. Tsangaratos, "Land subsidence phenomena investigated by spatiotemporal analysis of groundwater resources, remote sensing techniques, and random forest method: the case of Western Thessaly, Greece," *Environmental Monitoring and Assessment*, vol. 190, no. 11, pp. 623–642, 2018.

[35] D. Raucoules, I. Parcharidis, D. Feurer et al., "Ground deformation detection of the greater area of Thessaloniki (northern Greece) using radar interferometry techniques," *Natural Hazards Earth System Science*, vol. 8, no. 4, pp. 779–788, 2008.

[36] F. Raspini, C. Loupasakis, D. Rozos, N. Adam, and S. Moretti, "Ground subsidence phenomena in the Delta municipality region (northern Greece): geotechnical modeling and validation with persistent scatterer interferometry," *International Journal of Applied Earth Observation and Geoinformation*, vol. 28, pp. 78–89, 2014.

[37] N. Svigkas, I. Papoutsis, C. Loupasakis, P. Tsangaratos, A. Kiratzi, and C. Kontoes, "Land subsidence rebound

detected via multi-temporal InSAR and ground truth data in Kalochori and Sindos regions, northern Greece," *Engineering Geology*, vol. 209, pp. 175–186, 2016.

[38] N. Svigkas, I. Papoutsis, C. Loupasakis, P. Tsangaratos, A. Kiratzi, and C. Kontoes, "InSAR time-series monitoring of ground displacement trends in an industrial area (Oreokastro-Thessaloniki, Greece): detection of natural surface rebound and new tectonic insights," *Environmental Earth Sciences*, vol. 76, no. 5, article 195, 2017.

[39] F. Raspini, C. Loupasakis, D. Rozos, and S. Moretti, "Advanced interpretation of land subsidence by validating multi-interferometric SAR data: the case study of the Anthemountas basin (northern Greece)," *Natural Hazards and Earth System Sciences*, vol. 13, no. 10, pp. 2425–2440, 2013.

[40] F. Raspini, S. Bianchini, S. Moretti et al., "Advanced interpretation of interferometric SAR data to detect, monitor and model ground subsidence: outcomes from the ESA-GMES Terrafirma project," *Natural Hazards*, vol. 83, no. S1, pp. 155–181, 2016.

[41] N. Svigkas, I. Papoutsis, C. Loupasakis, P. Tsangaratos, A. Kiratzi, and C. H. Kontoes, "Radar space measurements of the deforming trends at northern Greece resulting from underground water activity," in *Advances in Remote Sensing and Geo Informatics Applications*, pp. 309–313, 2019.

[42] N. Svigkas, C. Loupasakis, P. Tsangaratos, I. Papoutsis, A. Kiratzi, and C. H. Kontoes, "A deformation study of Anthemountas graben (northern Greece) based on in situ data and new InSAR results," *Arabian Journal of Geosciences*, vol. 13, no. 13, 2020.

[43] G. D. Georgopoulos, *The evolution of the settlements in Moschato area*, KEDE Technical Report, 1990.

[44] G. D. Georgopoulos and E. X. Teleioni, "The development of the detected settlements on the coast of N. Faliro, Moshato, Kalithea," in *6th Greek Geotechnical and Geo-environmental Engineering Conference*, vol. 8, Technical Chamber of Greece, Volos, 29/09-01/2010.

[45] T. Kakatsos, N. Maimaris, and G. Priftis, *Monitoring of deformations of the load bearing elements of the Peace and Friendship Stadium and the subsidence of the nearby area. Detection of subsidence in the areas of N. Faliro-Moschato-Kallithea*, School of Rural and Surveying Engineering, N.T.U.A., Athens, B.Sc. Thesis, 1996.

[46] E. Gkadolou, *Establishment of GPS Network for Monitoring Settlements in the Moschato Region*, School of Rural and Surveying Engineering, N.T.U.A., Athens, B.Sc. Thesis, 2002.

[47] E. Karamolegkou, *The evolution of the vertical displacements in the areas of N. Faliro, Moschato and Kallithea*, School of Rural and Surveying Engineering, N.T.U.A., Athens, B.Sc. Thesis, 2009.

[48] S. Haralambakis, "Contribution to the knowledge of Neogene of Attica," *Annales Géologiques des Pays Helléniques*, vol. 4, 1952.

[49] P. Gaitanakis, *Geological Map of Greece, 1:50000, Sheet Athinai - Piraieus*, I.G.M.E Publications, 1982.

[50] D. Papanikolaou, E. Lekkas, C. Sideris et al., "Geology and tectonics of Western Attica in relation to the 7-9-99 earthquake," Tech. Rep. 3, Newsletter of E.C.P.F.E., Council of Europe, 1999.

[51] M. Kynigalaki, N. Nikolaou, J. Karfakis et al., "Engineering geological map of the Athens prefecture area," in *Scale 1:50.000, Institute of Geological and Mineralogical Research of Greece & Department of Geology*, University of Patras, 2010.

[52] M. Kynigalaki, N. Nikolaou, J. Karfakis et al., "Digital engineering geological map of the Athens prefecture area and related database management system," *Bulletin of the Geological Society of Greece*, vol. 43, no. 3, pp. 1619–1626, 2010.

[53] I. Sellountos, *Geotechnical Investigation of School Buildings in Moschato*, KEDE Technical report, 1980.

[54] B. Thymis, *Geotechnical Investigation in the Plot at 4 Kefallinia Street in Moschato*, KEDE Technical report, 1982.

[55] I. Christodoulias, "Geotechnical investigation on Thessalonikis Street of the Moschato municipality," KEDE Technical report, 1983.

[56] N. Sabatakakis, "Geological-Geotechnical survey in the basin of Athens [Ph.D. thesis]," Department of Geology, University of Patras, 1991.

[57] D. Mpara and C. Giannaros, *Geotechnical Investigation at 13-15 Chrysostomou Smyrnis Street of the Moschato Municipality*, Ministry for the Environment, Physical Planning and Public Works of Greece, 1994.

[58] G. Koukis and N. Sabatakakis, "Engineering geological environment of Athens, Greece," *Bulletin of Engineering Geology and the Environment*, vol. 59, no. 2, pp. 127–135, 2000.

[59] I. Koumantakis, "Research of hydrogeological conditions and of the operating procedures of the ground water in the basin of Attica, Main Issue, (A' and B' Phase)," Research program in the years 1996 and 1997 performed by the research team of the Section of Geological Sciences in cooperation with the Organization of Planning and Environmental Protection Of Athens, 1997.

[60] I. Koumantakis, K. Stavropoulos, and D. Dimitrakopoulos, "Hydrogeological status and operating condition of ground water in the basin of Attica," Minutes of the 4th Hydrogeological Conference of the Greek Hydrogeological Committee, Thessaloniki, 1997.

[61] S. Usai, "A least squares database approach for SAR interferometric data," *IEEE Transactions on Geoscience and Remote Sensing*, vol. 41, no. 4, pp. 753–760, 2003.

[62] P. Berardino, G. Fornaro, R. Lanari, and E. Sansosti, "A new algorithm for surface deformation monitoring based on small baseline differential SAR interferograms," *IEEE Transactions on Geoscience and Remote Sensing*, vol. 40, no. 11, pp. 2375–2383, 2002.

[63] E. Papageorgiou, M. Foumelis, and I. Parcharidis, "Long-and short-term deformation monitoring of Santorini volcano: unrest evidence by DInSAR analysis," *IEEE Journal of Applied Earth Observations and Remote Sensing*, vol. 5, no. 5, pp. 1531–1537, 2012.

[64] K. Goel, N. Adam, and C. Minet, "Long term analysis of strong non-linear deformations induced by coal mining using the SBAS technique," *ESA Fringe Symp*, vol. 19-23, 2011.